MOLECULAR-SCALE UNDERSTANDING OF ELECTRONIC POLARIZATION IN ORGANIC MOLECULAR CRYSTALS

A THESIS
PRESENTED TO
THE ACADEMIC FACULTY

BY

SEAN M. RYNO

IN PARTIAL FULFILLMENT
OF THE REQUIREMENTS FOR THE DEGREE
DOCTOR OF PHILOSOPHY IN THE
SCHOOL OF CHEMISTRY AND BIOCHEMISTRY

GEORGIA INSTITUTE OF TECHNOLOGY
AUGUST 2015

MOLECULAR-SCALE UNDERSTANDING OF ELECTRONIC POLARIZATION IN ORGANIC MOLECULAR CRYSTALS

Approved by:

Professor C. David Sherrill, Advisor
School of Chemistry and Biochemistry
Georgia Institute of Technology

Professor Jean-Luc Brédas, Thesis Advisor
School of Chemistry and Biochemistry
Physical Sciences and Engineering Division
Georgia Institute of Technology
King Abdullah University of Science and Technology

Professor Kenneth R. Brown
School of Chemistry and Biochemistry
Georgia Institute of Technology

Professor Seth R. Marder
School of Chemistry and Biochemistry
Georgia Institute of Technology

Professor Seung Soon Jang
School of Materials Science and Engineering
Georgia Institute of Technology

Date Approved: 6/24/2015

This thesis is dedicated to my wife and daughter,

Brittany Fay Ryno and Brittain Leah Ryno,

without whose love and support

none of this would have been possible, and

in remembrance of my childhood friend, Zak McConnell,

and my Grandfathers,

William "Bill" Kelley and Robert "Bob" Ryno.

ACKNOWLEDGEMENTS

I would like to thank Professor Brédas for his constant support, guidance, and mentorship over the last 5 years. I appreciate the encouragement he has provided and the enthusiasm that he has had in my work. When I arrived at Georgia Tech I had little experience in computational chemistry, with my primary background in synthetic chemistry. He took a chance by taking me as the fourth new graduate student to join the group that year for which I am eternally grateful.

While I am indebted to a number of people whom have made my experience as a graduate student both enjoyable and enlightening, I would like to specifically thank those within the Brédas group for sharing their knowledge and experience when I needed it and for offering insight to problem solving and scientific thinking. I would like to specifically thank Professor Chad Risko, for providing guidance, support, and the willingness to allow me to bounce ideas and results off of him, assist in collecting my thoughts, and help direct my research. Chad has also helped me to vastly improve my – still lacking – writing skills through countless revisions to drafts and reports. I would also like to thank: Dr. Veaceslav Coropceanu for his willingness to ask the tough questions and then helping to guide me through, then, abstract concepts; Dr. Paul Winget for sharing his knowledge and willingness to discuss computers when I needed something to distract me; and, Dr. John Sears for helping me to think critically about the works of others. I would like to thank the members of the Sherrill group including Professor Sherrill, Dr. Rob Parrish, Dr. Shawn Marshall, and Trent Parker for numerous discussions and assistance with a number of technical issues using the PSI series of programs.

In addition, I would like to thank our sister group, the Laboratory for Chemistry of Novel Materials at the University of Mons, for graciously hosting me during a short stay in Belgium. In particular, I would like to acknowledge Professor Roberto Lazzaroni and Agnès Leclercq for arranging my stay, and Drs. David Beljonne and Jérôme Cornil, Dr. Silvio Osella, Dr. Andrea Minoia, Dr. Claire Tonnelé, Dr. Luca Grisanti, Dr. Dorota Niedzialek, and Angelos Giannakopoulos for making my time in Mons both highly enjoyable and insightful.

I am also grateful to Professors Thompson and Tomlinson for introducing me to scientific research in general and thus opening my eyes to a field in which I had only fleeting familiarity. Professor Tomlinson introduced me to computational chemistry and arranged for a talk from Professor Brédas at UNG where I eventually decided that I wanted to enter the field of computational chemistry and pursue a position under Professor Brédas.

I would like to also acknowledge my Dissertation committee members for challenging me during my OP: Professor Brédas, Professor Sherrill, Professor Brown, Professor Marder, and Professor Jang.

Finally, I would like to express my deepest appreciation for the love and support that my family has provided throughout my graduate school experience. To my wife, Brittany, and my daughter, Brittain, I could never thank you enough for the constant love and support you have shown me, and willingness to move to Saudi Arabia. To my parents, Ron and Cathy, thank you for pushing me to forge my own path at a young age and willingness to teach me subjects well ahead of where we were in school. Finally, to my grandparents, thank you for never failing to believe in me and support my decision to continue my education.

TABLE OF CONTENTS

LIST OF TABLES

LIST OF FIGURES

LIST OF ABREVIATIONS

AMOEBA	Atomic Multipole Optimized for Biomolecular Simulation Force Field
B3LYP-D	Becke 3-Parameter, Lee-Yang-Parr Hybrid Functional with D2 Dispersion
B88	1988 Functional of Becke
B97D	1997 Functional of Becke with D2 Dispersion of Grimme
CCSD	Coupled-Cluster Single- and Double-Excitations
CCSD(T)	Coupled-Cluster Single- and Double-Excitations and Perturbative Triples
CHELPG	Charges from Electrostatic Potentials using a Grid Based Method
CSD	Cambridge Structural Database
D	Debye
DFT	Density Functional Theory
DMA	Distributed Multipole Analysis
DNA	Deoxyribonucleic Acid
EA	Electron Affinity
EH	Interacting Electron-Hole Pair
ESP	Electrostatic Potential
eV	Electron-Volts
GDMA	Generalized Distributed Multipole Analysis
GGA	Generalized Gradient Approximation
HF	Hartree-Fock
IE	Ionization Energy
INDO	Intermediate Neglect of Differential Overlap

IPES	Inverse Photoelectron Spectroscopy
Kcal/mol	Kilocalories per mole
LDA	Local Density Approximation
LYP	Correlation Functional of Lee, Yang, and Parr
MD	Molecular Dynamics
MM	Molecular Mechanics
MP2	Møller-Plesset Second-Order Perturbation Theory
NI-EH	Non-Interacting Electron-Hole Pair
OFET	Organic Field-Effect Transistor
OLED	Organic Light-Emitting Diode
OPV	Organic Photovoltaic
OSC	Organic Semiconductor
PBE	Pure 1996 Functional of Perdew, Burke, and Ernzerhof
PW	Correlation Functional of Perdew and Wang
PZ	Correlation Functional of Perdew and Zunger
QEq	Self-Consistent Charge-Equilibration Scheme of Rappé and Goddard
QM	Quantum Mechanical
QMMM	Quantum Mechanics/Molecular Mechanics
SAPT	Symmetry-Adapted Perturbation Theory
SCF	Self-Consistent Field
SCS-MP2	Spin-Component Scaled MP2
TCNQ	Tetracyanoquinodimethane
TIPS	Tri-isopropylsilylethynyl

TNAP	Tetracyanonaphthoquinodimethane
UFF	Universal Force Field
UPS	Ultraviolet Photoelectron Spectroscopy
VWN	Correlation Functional of Vosko, Wilk, and Nusair
ZINDO	Zerner’s Intermediate Neglect of Differential Overlap

SUMMARY

Organic electronic materials, possessing conjugated π-systems, are extensively used as the active layers in organic electronic devices, where they are responsible for charge transport. In this dissertation, we employ a combination of quantum-mechanical and molecular-mechanics methods to provide insight into how molecular structure, orientation, packing, and local molecular environment influence the energetic landscape experienced by an excess charge in these organic electronic materials. We begin with an overview of charge transport in organic electronic materials with a focus on electronic polarization while discussing recent models, followed by a review of the computational methods employed throughout our investigations.

We provide a bottom-up approach to the problem of describing electronic polarization by first laying the framework of our model and comparing calculated properties of bulk materials to available experimental data and previously proposed models. We then explore the effects of changing the electronic structure of our systems though perfluorination, and investigate the effects of modifying the crystalline packing through the addition of bulky functional groups while investigating how the non-bonded interactions between molecular neighbors change in different packing motifs.

As interfaces are common in organic electronics and important processes such as charge transport and charge separation occur at these interfaces, we model organic-vacuum and organic-organic interfaces to determine the effect changing the environment from bulk to interface has on the electronic polarization. We first investigate the effects of removing polarizable medium adjacent to the charge carrier and then, by modeling a realistic organic-

organic interface in a model solar cell, probe the environment of each molecular site at the interface to gain a more complete understanding of the complex energetic landscape. Finally, we conclude with a study of the non-bonded interactions in linear oligoacene dimers, model π-conjugated materials, to assess the impact of dimer configuration and acene length on the intermolecular interaction energy, and highlight the importance of dispersion and charge penetration to these systems.

CHAPTER 1

INTRODUCTION

1.1 Overview

Organic π-conjugated materials, both small molecules and polymers, have garnered considerable interest as the active layers in crystalline and thin-film organic electronic devices;[1-6] these include organic light-emitting diodes (OLED) that have recently had large commercial success in handheld devices, organic photovoltaic cells (OPV) with light to power conversion efficiencies exceeding 12%,[7,8] and organic field-effect transistors (OFET) with reported carrier mobilities larger than 50 $cm^2V^{-1}s^{-1}$.[9] While yet fully realized, the primary motivation behind the large research effort into organic semiconductor materials has been the promise of reduced manufacturing costs compared to their inorganic counterparts through high-throughput fabrication methods, such as roll-to-roll processing, and distinctive materials properties made available through the vast toolbox of organic synthetic chemistry.

Central to the operation of all organic electronic devices is the efficiency for which the active layer transports charge carriers, either positive charges, holes, or negative charges, electrons. The charge transport is quantified in terms of mobility, μ,

$$\mu = \frac{\upsilon_d}{E} \tag{1.1}$$

with units of $cm^2V^{-1}s^{-1}$ where E is the electric field applied to an organic electronic material and υ_d is the average drift velocity of the charge carrier.[10] The charge-carrier mobility is dependent on a number of properties including the chemical and molecular structure of the conjugated moiety, impurities and defects within that active layer that can act as charge trapping sites that reduce the carrier mobility, and the solid-state molecular packing. Additional factors including temperature, electric field, pressure, charge-carrier density, and molecular weight will also impact the charge carrier mobility.[9,11-19]

In general, the properties of organic semiconductors (OSC) are dictated by molecular and chemical structure, interactions at materials interfaces, and processing. Hence, a bottom-up understanding of the processes that occur at the microscopic scale and the impact of each of these factors is needed for a more complete understanding of OSCs. Computational and theoretical chemistry studies provide detail at levels not attainable, but compatible with, experimental studies, and as the rate of charge-carrier transport in organic electronic materials constitutes a limiting factor of device efficiency, a fundamental understanding of the charge transfer mechanisms in organic materials is necessary if the full potential of these materials is to be realized.

1.2 Charge Transport in Organic Semiconductors

Charge transport in organic electronic materials is typically described within one of two general models: the band model or the hopping model. The band model approach emphasizes the delocalization of the electronic wavefunction over the entire material, as in crystalline inorganic solids. Thus, the charge carrier is classified as delocalized. As organic solids are held together by relatively weak van der Waals interactions, instead of strong covalent bonds, the delocalization of the charge is expected to be restricted to a few molecules, thus limiting the accuracy of traditional band theory approaches.[20,21] The propensity of band-like transport in organic materials may be probed by measuring the mobility as a function of temperature, where one should expect to see a strong reduction in the mobility with an increase in temperature (T^{-n} dependence).[10] Two examples of this are: single crystal naphthalene where the mobility of an electron as measured via transient photoconductivity is reduced by > 50% as the temperature is increased from 54 K to 100 K,[22] and more recently, in rubrene field-effect transistors, where the mobility has been shown to rapidly decrease over the range of temperatures from 200 K to 300 K.[23]

An alternative model is based on charge-carrier hopping, wherein the carrier is strongly localized on an individual (or few) molecule(s) and the movement of charge is described as a hopping event between interacting molecules under the application of an electric field. In that case, the hopping rate between molecules *i* and *j* may be modeled using the Marcus expression for semi-classical electron transfer:[24]

$$k_{ij} = \frac{t^2}{\hbar}\left[\frac{\pi}{k_B T\lambda}\right]^{1/2} \exp\left[-\frac{\left(\lambda + \epsilon_j - \epsilon_i\right)^2}{4k_B T\lambda}\right] \tag{1.2}$$

where t is the electronic coupling (transfer integral), k_B is the Boltzmann constant, $\hbar$ is the reduced Planck constant, T is the temperature, λ is the reorganization energy associated with the charge-transfer reaction $M_i^- + M_j \rightarrow M_i + M_j^-$, and $\epsilon_{i(j)}$ are the site energies.

Hopping transport is characterized by an increased mobility with increased temperature, as it corresponds to an activated process.[25] Using the Marcus expression, the terms that determine the rate of charge transfer at a given temperature are the electronic coupling, reorganization energy, and the difference of the site energies.

Each of these terms is impacted by the environmental polarization due to the presence of a charge carrier. Described in more detail below, this polarization energy has both a nuclear and electronic component where the neighboring molecules will move in response to the change in electrostatic interactions; see Figure 1.1. The electronic coupling, t, does not have a direct dependence on the polarization energy, but it is often estimated as one-half the dimer energy splitting (*i.e.*, one-half the energy difference between the highest occupied molecular orbital (HOMO) and HOMO-1 of a dimer compared to the HOMO of the isolated molecules).[26] This approximation, though, only holds if the site energies are equal. In polarizable materials, an over estimation of the transfer integral will result if the change in intermolecular interactions, resulting from polarization by the electrostatic environment, are not included. The reorganization energy is composed of an intramolecular reorganization of the charged molecule, and an intermolecular reorganization of the surrounding bulk, $\lambda = \lambda_{\text{intra}} + \lambda_{\text{inter}}$. Both the electronic and nuclear polarizations have a cascade effect, wherein the polarization of nearest-neighbors of the charged molecule further polarize the next-nearest-neighbors and so on.[25]

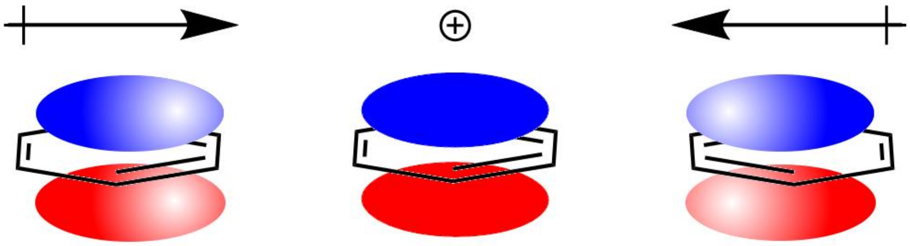

Figure 1.1. Schematic representation of electronic polarization in a benzene trimer. Charge-induced dipoles form, resulting from a shift in π-electron density on neighboring molecules, to stabilize the charge carrier.

1.3 Polarization in Organic Electronic Materials

1.3.1 Lyons Model

The polarization energy in organic materials is the stabilization of a charge carrier due to its environment. A phenomenological model of the polarization energy was first proposed by Lyons in 1957[27,28] who drew attention to the fact that the ionization energy, IE, of a crystal was dramatically different than that of the gas phase IE; for example the ionization energy of crystalline pentacene is some 1.6 eV lower than that of the isolated molecule.[29] Since the electronic structure of weakly interacting molecules changes only slightly between the isolated molecule and molecular crystal, it was assumed that the change in IE was due to the stabilization of the hole by the electrostatic environment. As such the polarization energy due to a positive charge carrier, P_+, is defined as:

$$P_+ = IE_{ss} - IE_g \tag{1.3a}$$

where IE_g and IE_{ss} are the gas-phase and solid-state ionization energies, respectively. Likewise, the polarization due to an electron, P_-, is defined as:

$$P_{-} = EA_{ss} - EA_{g} \tag{1.3b}$$

where EA_g and EA_{ss} are the gas-phase and solid-state electron affinities, respectively.

Experimentally, P_+ can be evaluated directly via ionization energies determined from ultraviolet photoelectron spectroscopies (UPS) of the isolated and solid-state systems. The experimental determination of P_- is much more difficult, as inverse photoelectron spectroscopies (IPES) have limited resolution. Thus experimental determination of P_- is typically determined through a combination of techniques as:

$$P_{-} = IE_{ss} - EA_{g} - E_{g} \tag{1.4}$$

where IE_{ss} and EA_g are measured via UPS, and E_g is the energy gap generally measured via UV-Vis spectroscopy.. Table 1.1 shows experimentally determined values for both P_+ and P_- for a number of common organic electronic materials. Note that the polarization energies due to a positive change in the planar acenes lies in the range of 1.6 eV – 1.7 eV, but substitution can result in either a strong increase or decrease of the polarization energy. For each of the linear oligoacenes, the polarization energy due to a positive charge is larger than that due to a negative charge.

Table 1.1. Experimental polarization energies due to a positive (P_+) or negative (P_-) charge and polarization asymmetry for common organic electronic materials. Data included as available. All units in eV.

(eV)	P_+	P_-	$\lvert P_+ - P_- \rvert$
Benzene[a]	1.6	--	--
Naphthalene[b]	1.72	1.10	0.62
Anthracene[b]	1.65	1.09	0.56
Tetracene[c,d]	1.63	0.92	0.71
Pentacene[b]	1.63	1.12	0.55
Fullerene (C_{60})[e]	1.1 – 1.4	1.5 – 1.9	0.4 – 0.8
Perylene[a]	1.7	--	--
Rubrene[a]	1.1	--	--
Tetracyanoquinodimethane (TCNQ)[a]	2.1	--	--
Tetracyanonaphthoquinodimethane (TNAP)[a]	2.5	--	--

[a]Ref. 30. [b]Ref. 29. [c]Ref. 31. [d]Ref. 32. [e]Ref. 33.

1.3.2 Polarization Energy Components

The polarization energy is composed of both nuclear and electronic contributions. These occur on different timescales, 10^{-16}-10^{-15} s for electronic processes and on the order of

10^{-14} s to 10^{-11} s for nuclear relaxations.[25] Because of the large difference in timescales, the polarization energy can be separated as:

$$P = E_{nuc} + E_{elect} \tag{1.5}$$

thus constituting a sum of nuclear and electronic contributions.

In practice, the polarization energy may be further separated and considered as a collection of separate energetic contributions to a collective polarization energy as:[34]

$$P = E_{nuc} + E_{dip} + E_{qQ} + E_{id} + E_{iQ} + E_{M} \tag{1.6}$$

where E_{nuc} is the nuclear relaxation, both of the molecular lattice and the charged species, E_{dip} represents the static dipole moment interactions, E_{qQ} is the interaction energy between the charged molecule and the permanent quadrupole moments of neighboring molecules, E_{id} is the energetic contributions of the induced-dipole interactions, and E_{iQ} and E_{M} are the charge delocalization and high-order multipole interactions, respectively. We may, also, partition the electronic terms of Equation 1.5 such that the electronic polarization energy is a sum of static and dynamic polarization energies:

$$E_{elect} = P_{\pm} = S_{\pm} + D_{\pm} \tag{1.7}$$

where the static polarization energy results from the charge–static-multipole interactions and the dynamic polarization energy, from the charge–induced-multipole interactions.

We note that the experimental and theoretical evaluations of intermolecular charge delocalization in oligoacene model systems is challenging and constitutes an active area of research, especially as it pertains to the proper physical description of charge-carrier transport in organic molecular crystals.[11,32,35,36] For instance, UPS studies of naphthalene clusters suggest that both positive and negative charges delocalize over at least a few molecules,[20] which brings into question charge-hopping models that fully constrain the charges on single molecules; it is also worth noting that the amount of exact (nonlocal) exchange employed in commonly used hybrid density functionals does greatly influence the theoretical description of charge delocalization.[37]

1.3.3 Models for Polarization Energy in Organic Molecular Crystals

Commonly, the effect of the electrostatic environment in quantum-chemical calculations is modeled using a continuous polarizable medium, but these models fail to capture the anisotropic nature of organic molecular crystals. As such, more detailed models must be used that include these anisotropic effects. Currently, there are three main models that have been described in the literature pertaining to the determination of electronic polarization energy in organic molecular crystals: (i) the microelectrostatic model (ii) the semiempirical model developed by Soos and co-workers,[38] and (iii) the hybrid quantum-mechanics–molecular-mechanics model.[39]

1.3.3.1 Microelectrostatic Model

Of the models considered here, the microelectrostatic model has seen the largest degree of continuous development with major contributions from Munn in a series of papers from 1979 to 1983.[40-45] These papers provide a detailed application of microelectrostatics to the problem of the polarization energy due to a localized charge by first treating each molecule in the molecular crystal as a single polarizable point, and then extending to a sub-molecular approach wherein each aromatic ring is treated by a polarizable point. Munn also highlighted the importance of the charge-quadrupole contribution to the polarization energy in linear oligoacenes, the impact of vacancies in the molecular lattice, and the effect of changing the molecular polarizability.

The microelectrostatic model employed by Verlaak *et al.*[46] to describe pentacene extended the investigations of Munn by exploring the effect of the number of polarizable points for each molecule, *e.g.*, pentacene is be composed of 5 (center of each fused ring) or 22 (each carbon center) polarizable points. Within the framework of this model the static and dynamic contributions to the electronic polarization energy are calculated independently and then summed together. The static contribution consists of quadrupole-quadrupole and charge-quadrupole interactions where an excess charge is equally distributed across all polarizable points, and the molecular quadrupole is distributed equally across points such that the new point-centered, isotropic quadrupoles reproduce the molecular quadrupole moment. Lastly, as with the molecular quadrupole moment, the molecular polarizability is also equally distributed over all polarizable points so that when treated in an additive fashion the anisotropic molecular dipole polarizability is recovered.

Table 1.2. Charge-quadrupole ($E_{q\text{-}Q}$), charge–induced-dipole ($E_{q\text{-}id}$), and electronic polarization (P_+) energies for a hole in an infinitely large anthracene or pentacene crystal. For pentacene, both molecules in the unit cell have been considered. Values in parentheses are unit-cell positions. All units in eV. Adapted from Ref. 46.

(eV)	$E_{q\text{-}Q}$	$E_{q\text{-}id}$	P_+
Anthracene	1.320	0.264	1.584
Pentacene (0,0,0)	1.157	0.258	1.415
Pentacene (1/2,1/2,0)	1.158	0.321	1.479

The microelectrostatic model has demonstrated wide versatility, having been applied to the evaluation of the bulk polarization energy in anthracene and pentacene, effects due to unit-cell asymmetry (see Table 1.2), grain boundaries in pentacene crystals, and material heterojunctions.[46-48] As the pentacene crystal unit cell is composed of two non-equivalent molecules, Verlaak has calculated the polarization energy at each site and found the polarization energy to differ by about 0.06 eV (4%) between the sites. While this value itself is small, it is interesting to note that the charge–induced-dipole contributions for each site are nearly equal (1.158 *vs*. 1.157 eV) and that the difference calculated is almost entirely a result of the charge-quadrupole interactions (0.321 *vs*. 0.258 eV). Extending this model to pentacene/C_{60} interfaces Verlaak *et al*. showed that in an ideal *edge-on* pentacene-fullerene interface there is an approximately 0.4 eV barrier to charge separation, while charge separation in the *face-on* pentacene-fullerene interface is quasi-barrierless.

By definition there is no polarization asymmetry, *i.e.*, $P_+ - P_- = 0$, within this application of the microelectrostatic model. This results from the distribution of charge within the charged species, where the charge at each sub-molecular point is equal, but opposite in sign for the hole and the electron. Thus an accurate description of the charge distribution is necessary to properly describe the polarization energy. This shortcoming has very recently been addressed by D'Avino *et al.*[49] who have shown good agreement with experiment for anthracene and pentacene.

1.3.3.2 Semiempirical Model

The model of Tsiper and Soos, for which molecular polarizabilities and charge distributions are calculated using the semiempirical INDO/S Hamiltonian, and partial charges are assigned using Löwdin charges, has been in use for more than a decade.[49-52] Within this model each molecule in a spherical cluster is described by ρ_i, the molecular charge distribution at atom *i*, $\tilde{\alpha}_i$, the linear polarizability tensor associated with atom *i*, and Π_{ij}, the atom-atom polarizability tensor describing the susceptibility of atomic charges to an applied potential that is used to calculate charge redistribution, where each of these values may be different for the neutral and charged molecules. For clusters of different size, from one molecule to hundreds, the total energy of the system is calculated as:

$$E_{tot} = \frac{1}{2}\sum_m \sum_i \left(q_{mi} V_{mi}^{(0)} - \mu_{mi} \cdot F_{mi}^{(0)} \right) \tag{1.8}$$

where $V_{mi}^{(0)}$ and $F_{mi}^{(0)}$ are the potential and field when there is no charge redistribution and no induced-dipole polarization at atom *i* of molecule *m*, and includes all interactions from permanent charges, $q_{mi}^{(0)}$, charge redistribution, ρ_{mi}, and induced dipoles, μ_{mi}.

Table 1.3. Polarization energies ($P_{+}+P_{-}$) and polarization asymmetries ($P_{+}-P_{-}$) due to a positive and negative charge using the semiempirical model. Also, the difference of the polarization energy at a given interface and the bulk are presented. All units in eV. Values for bulk polarization energy and asymmetry are approximate values from figures as exact values are not reported. Positive values represent a stabilization and negative values represent a destabilization. Adapted from Refs. 38 and 51.

(eV)	$P_{+}+P_{-}$	$P_{+}-P_{-}$	$P^{i}-P$
Perylenetetracarboxylic acid dianhydride (PTCDA)	1.82	~2.7	--
Anthracene	2.20	< 0.01	--
Pentacene	2.01	0.03	--
Pentacene (vacuum)	--	--	-0.23
Pentacene (on Au surface)	--	--	0.13

Similar to the microelectrostatic model this semiempirical model has been applied to a number of chemical systems and interfaces, partially summarized in Table 1.3. Having been applied to pentacene-vacuum interfaces and pentacene-gold interfaces this model shows large differences in the polarization at the interface compared to the bulk. Interestingly, Tsiper and Soos report a reduction in the polarization energy at a vacuum interface of 0.23 eV and a stabilization of an excess charge at a gold interface of 0.13 eV. Additionally, they estimate values of 20 – 40 meV for the difference in polarization energy due to non-equivalent molecules in the unit cells used.

Table 1.4. Polarization energies for anthracene and pentacene from the semiempirical model using Löwdin charges, ESP charges, and the DFT electron density. All values in eV.

	Anthracene			*Pentacene*		
(eV)	P_+	P_-	P_+-P_-	P_+	P_-	P_+-P_-
Löwdin Charges[a,b]	1.10	1.10	< 0.01	1.03	0.98	0.03
ESP Charges[c]	1.18	0.95	0.23	1.08	0.82	0.26
DFT Electron Density[d]	1.38	0.82	0.56	--	--	--

[a]Ref. 38. [b]Ref. 51. [c]Ref. 49. [d]Ref. 53.

In the initial implementation of the semiempirical model polarization energy asymmetries of much less than 0.1 eV were reported for anthracene and pentacene. Since these initial reports, the semiempirical model has been modified to incorporate the use of electrostatic potential (ESP) charges or to use the DFT electron density for the permanent charge distribution. Both methods represent an improvement over the initial implementation in terms of absolute values of the polarization energies and asymmetries; see Table 1.4. While the DFT results agree very well with experimental data, the computational cost limits its application to the smallest systems, whereas the ESP-derived charges represent a compromise to allow reliable calculations of polarization asymmetries at reasonable computational cost.

1.3.3.3 Hybrid QMMM Model

The hybrid QMMM model[39] of attempts to combine aspects of both the previous models to create a methodology where the charged molecule in a molecular crystal is treated via quantum mechanical methods while the effect of the environment is treated as a perturbation with its effects captured classically. Here the ONIOM methodology[54] is used, where the total energy of the system is defined as:

$$E_{ONIOM} = E_{MM,\mathrm{real}} - E_{MM,\mathrm{model}} + E_{QM,\mathrm{model}} \tag{1.9}$$

where *MM* and *QM* are the level at which each system is treated, and *real* and *model* refer to the entire system and the portion of the system treated quantum mechanically, respectively. While the QM region is treated using density functional theory, the MM region has been treated using the UFF force field[55] with the partial atomic charges of the bulk included in the QM calculations to better model the electrostatic environment. To allow the bulk material to polarize the QM region the CHELPG charges[56] of the QM region are iteratively updated into the UFF force field. The partial charges of the bulk are then allowed to fluctuate using the self-consistent charge equilibration scheme (QEq) of Rappé and Goddard,[57] and subsequently updated in the QM calculations. This process is then repeated until convergence.

By using small, two-dimensional clusters Norton and Brédas have calculated the site energy difference in tetracene and pentacene to be on the order of 0.01 eV, similar to that reported by Verlaak and Tsiper. Also, they have improved upon one of the shortcomings of the microelectrostatic model, namely that the charge distributions for the positively and negatively charged systems are not identical, and as a result, each have a different impact on the bulk; see Figure 1.2. Their calculated polarization asymmetries of 0.11 eV to 0.25 eV, for naphthalene through pentacene, are in much better agreement with experimental polarization asymmetries (Table 1.5). Although, they report a reversal of the relative ordering of the polarization energies, namely, that for all of the systems studied the polarization energy due to a hole is smaller than that of an electron, in direct contrast to what has been reported experimentally.

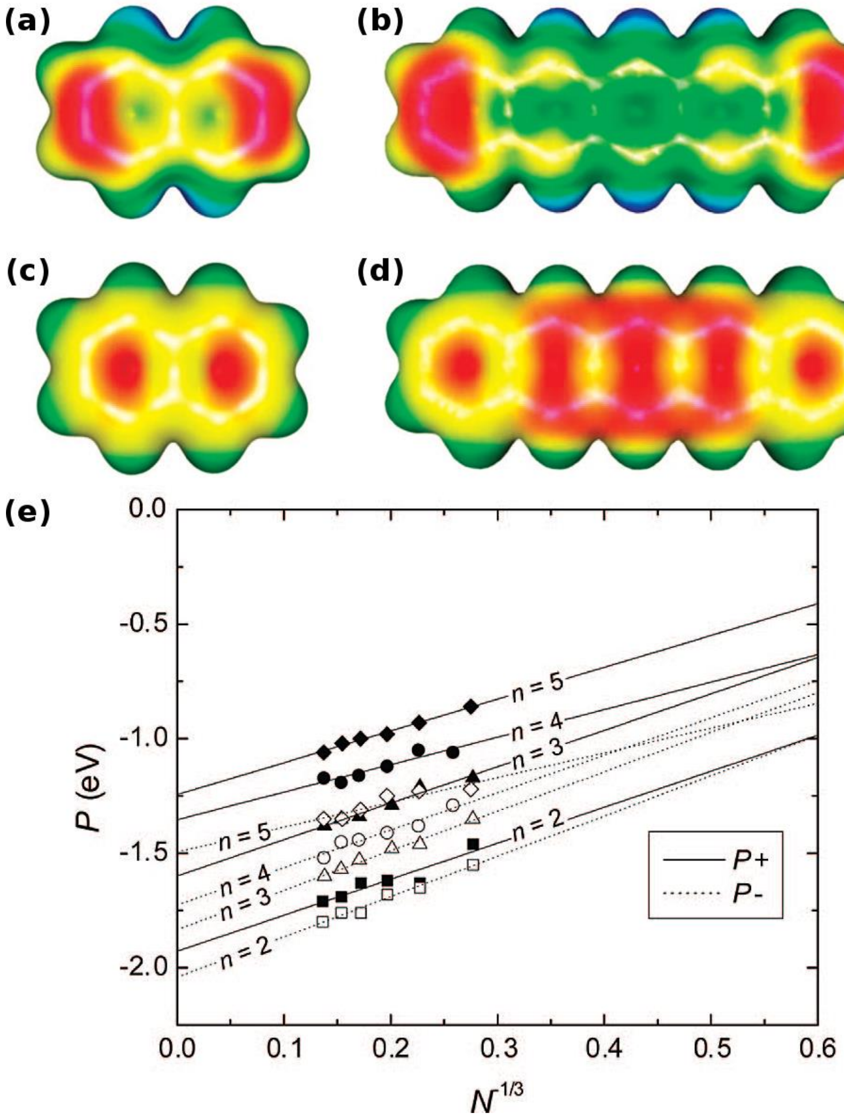

Figure 1.2. Electrostatic potential surface of naphthalene with a positive (a) or negative (c) charge and pentacene with a positive (b) or negative (d) inside of spherical clusters. Red areas represent areas of electron repulsion and blue areas show electron attraction. (e) Polarization energy of spherical clusters treated by the QMMM model at the B3LYP/6-31+G(d,p)/UFF level as a function of $N^{-1/3}$ where N is the number of molecules in the cluster. Linear fits are used to extrapolate to the bulk polarization energy. Adapted from Ref. 39.

Table 1.5. Polarization energies and polarization asymmetries due to a positive or negative charge using the hybrid QMMM model. All units in eV. Adapted from Ref. 39.

(eV)	P_+	P_-	P_+-P_-
Naphthalene	1.93	2.04	0.11
Anthracene	1.76	1.83	0.07
Tetracene	1.35	1.73	0.38
Pentacene	1.24	1.49	0.25

As underlined in section 1.3.3.1 a proper description of the charge-quadrupole and induced-dipole–quadrupole interactions is necessary to accurately model the polarization energy. In the oligoacenes, since the largest non-zero multipole moment is the quadrupole, properly accounting for the molecular quadrupole moments is crucial to describe the intermolecular interactions. Since most force fields, such as UFF, describe the electrostatic interactions using atom-centered point charges, even a qualitative description of the molecular systems is difficult without the use of auxiliary charges. Thus the improper description of the molecular quadrupoles by the UFF force field leads to the erroneous polarization orderings calculated by the hybrid QMMM model.

1.4 Thesis Objectives and Outline

The polarization energy, or the effect the electrostatic environment of a charge carrier has in response to the presence of the charge, has been in continuous study since the 1950s; it impacts the site energies within a molecular crystal and directly affects the rate of charge transport.[25,27] Thus by using computational methodologies the effects of molecular packing, molecular geometry, and bulk versus interface configurations may be understood to provide guidance for materials design. Additionally, a fundamental understanding of charge transport in organic electronic materials requires a detailed description of the intermolecular coupling between molecules, the reorganization of the nuclei associated with the change in charge of a molecule, and the polarization of the environment upon charge injection. Our goal in this Thesis is to detail the electronic polarization energy in organic semiconducting materials as a function of molecular structure and packing, and investigate the non-covalent interactions responsible for molecular packing as a function of molecular structure. Our results provide molecular-scale insight that may be used to better understand the semiconducting properties of organic electronic materials, and direct the design of organic electronic materials and crystal engineering efforts to produce materials with desired polarization energies.

In Chapter 2, we review the computational methodologies and our model used for the evaluation of electronic polarization energy as well as the methods necessary for model parameterization and to provide a description of non-covalent interactions. We begin with a description of the Schrödinger equation and the approximations needed to derive the electronic-structure methods employed in this thesis: Hartree-Fock, perturbation theory, symmetry-adapted perturbation theory, and density functional theory methods. Next, we provide a brief review of the distributed multipole analysis, the AMOEBA force field, and molecular dynamics used for the modeling of bilayer interfaces. Lastly, we describe the procedure for the parameterization of the electrostatic component of the AMOEBA force field necessary for the evaluation of the electronic polarization energy.

Chapter 3 details the limitations of previously proposed models for polarization energy, and lays the foundation for our newly proposed model using a polarizable force field. The model is validated by comparison to prior experimental investigations using the linear oligoacenes; the predictive ability of the model is demonstrated by the calculation of the polarization energy of molecular systems that have yet to have their polarization energy determined experimentally, the calculated results of which may be physically rationalized.

In Chapter 4 and Chapter 5, the impact of molecular packing on the polarization energy is demonstrated through a combination of comparison to experimentally studied materials and model system manipulations. First, we explain the observed reduction in polarization energy measured for a system that packs in a brickwork motif compared to a herringbone packing analogue though examination of the non-bonded interactions. We then use tetracene and rubrene to investigate the effect of changing molecular backbone orientation and reduced packing density within and between molecular layers. Finally, we show that while there is only a small difference in the polarization energy at an organic-vacuum interface compared to the bulk, the static and dynamic contributions are significantly different.

In Chapter 6, we use molecular dynamics to model a pentacene/C_{60} bilayer interface and show that the polarization energy at each molecular site is independent, resulting in a complex energetic landscape.

As organic molecular crystals are held together by weak van der Waals forces, Chapter 7 provides a detailed analysis of the non-bonded interactions in oligoacene dimers using symmetry-adapted perturbation theory. We find that the potential energy surfaces consists of deep, wide valleys that allow for a large variety of dimer configurations at room temperature and that the stabilizing contribution from charge penetration is nearly equivalent to the total dimer interaction energy in the most stable dimer configurations.

Lastly, Chapter 8 discusses conclusions, broad impact, and further directions to be considered. By applying our model of electronic polarization energy we provide additional insight into previous experimental investigations and give additional considerations for materials engineering efforts.

1.5 References

(1) Tang, C. W. *Appl. Phys. Lett.* **1986**, *48*, 183.

(2) Tang, C. W.; VanSlyke, S. A. *Appl. Phys. Lett.* **1987**, *51*, 913.

(3) Garnier, F.; Horowitz, G.; Peng, X.; Fichou, D. *Adv. Mater.* **1990**, *2*, 592.

(4) Burroughes, J. H.; Bradley, D. D. C.; Brown, A. R.; Marks, R. N.; Mackay, K.; Friend, R. H.; Burns, P. L.; Holmes, A. B. *Nature* **1990**, *347*, 539.

(5) O'Regan, B.; Gratzel, M. *Nature* **1991**, *353*, 737.

(6) Kippelen, B.; Bredas, J. L. *Ener. Envir. Sci.* **2009**, *2*, 251.

(7) NREL. NREL Best Research-Cell Efficiencies. Published Online: 2015. http://www.nrel.gov/ncpv/images/efficiency_chart.jpg (accessed March 23, 2015).

(8) Heliatek http://www.heliatek.com/newscenter/latest_news/neuer-weltrekord-fur-organische-solarzellen-heliatek-behauptet-sich-mit-12-zelleffizienz-als-technologiefuhrer/?lang=en#, 2013.

(9) Jurchescu, O. D.; Baas, J.; Palstra, T. T. M. *Appl. Phys. Lett.* **2004**, *84*, 3061.

(10) Coropceanu, V.; Cornil, J.; Silva, D. A. d.; Olivier, Y.; Silbey, R.; Bredas, J. L. *Chem. Rev.* **2007**, *107*, 926.

(11) Minder, N. A.; Ono, S.; Chen, Z.; Facchetti, A.; Morpurgo, A. F. *Adv. Mater.* **2012**, *24*, 503.

(12) McGarry, K. A.; Xie, W.; Sutton, C.; Risko, C.; Wu, Y.; Young, V. G.; Brédas, J.-L.; Frisbie, C. D.; Douglas, C. J. *Chem. Mater.* **2013**, *25*, 2254.

(13) Mas-Torrent, M.; Hadley, P.; Bromley, S. T.; Ribas, X.; Tarrés, J.; Mas, M.; Molins, E.; Veciana, J.; Rovira, C. *J. Am. Chem. Soc.* **2004**, *126*, 8546.

(14) Blom, P. W. M.; Jong, M. J. M. d.; Munster, M. G. v. *Phys. Rev. B* **1997**, *55*, R656.

(15) Sirringhaus, H. *Adv. Mater.* **2005**, *17*, 2411.

(16) Warta, W.; Karl, N. *Phys. Rev. B* **1985**, *32*, 1172.

(17) Mozer, A. J.; Denk, P.; Scharber, M. C.; Neugebauer, H.; Sariciftci, N. S.; Wagner, P.; Lutsen, L.; Vanderzande, D. *J. Phys. Chem. B* **2004**, *108*, 5235.

(18) Rang, Z.; Haraldsson, A.; Kim, D. M.; Ruden, P. P.; Nathan, M. I.; Chesterfield, R. J.; Frisbie, C. D. *Appl. Phys. Lett.* **2001**, *79*, 2731.

(19) Goh, C.; Kline, R. J.; McGehee, M. D.; Kadnikova, E. N.; Fréchet, J. M. J. *Appl. Phys. Lett.* **2005**, *86*, 122110.

(20) Saigusa, H.; Lim, E. C. *J. Phys. Chem.* **1994**, *98*, 13470.

(21) Mitsui, M.; Ando, N.; Nakajima, A. *J. Phys. Chem. A* **2007**, *111*, 9644.

(22) Schein, L. B.; Duke, C. B.; McGhie, A. R. *Phys. Rev. Lett.* **1978**, *40*, 197.

(23) Podzorov, V.; Menard, E.; Borissov, A.; Kiryukhin, V.; Rogers, J. A.; Gershenson, M. E. *Phys. Rev. Lett.* **2004**, *93*, 086602.

(24) Marcus, R. A. *Rev. Mod. Phys.* **1993**, *65*, 599.

(25) Silinsh, E. A. *Organic Molecular Crystals: Their Electronic States*; Springer: New York, 1980.

(26) Newton, M. D. *Chem. Rev.* **1991**, *91*, 767.

(27) Lyons, L. E. *J. Chem. Soc.* **1957**, 5001.

(28) Lyons, L. *Aust. J. Chem.* **1957**, *10*, 365.

(29) Sato, N.; Inokuchi, H.; Silinsh, E. A. *Chem. Phys.* **1987**, *115*, 269.

(30) Sato, N.; Seki, K.; Inokuchi, H. *J. Chem. Soc., Faraday Trans. 2* **1981**, *77*, 1621.

(31) Pope, M.; Burgos, J.; Giachino, J. *J. Chem. Phys.* **1965**, *43*, 3367.

(32) Ando, N.; Mitsui, M.; Nakajima, A. *J. Chem. Phys.* **2008**, *128*, 154318.

(33) Sato, N.; Saito, Y.; Shinohara, H. *Chem. Phys.* **1992**, *162*, 433.

(34) Silinsh, E. A.; Čápek, V. *Organic Molecular Crystals: Interaction, Localization, and Transport Phenomena*, 1994.

(35) Martinelli, N. G.; Ide, J.; Sanchez-Carrera, R. S.; Coropceanu, V.; Bredas, J. L.; Ducasse, L.; Castet, F.; Cornil, J.; Beljonne, D. *J. Phys. Chem. C* **2010**, *114*, 20678.

(36) Liu, T.; Cheung, D. L.; Troisi, A. *Phys. Chem. Chem. Phys.* **2011**, *13*, 21461.

(37) Sai, N.; Barbara, P. F.; Leung, K. *Phys. Rev. Lett.* **2011**, *106*, 226403.

(38) Tsiper, E. V.; Soos, Z. G. *Phys. Rev. B* **2001**, *64*, 195124.

(39) Norton, J. E.; Brédas, J.-L. *J. Am. Chem. Soc.* **2008**, *130*, 12377.

(40) Bounds, P. J.; Munn, R. W. *Chem. Phys.* **1979**, *44*, 103.

(41) Bounds, P. J.; Munn, R. W. *Chem. Phys.* **1981**, *59*, 41.

(42) Bounds, P. J.; Munn, R. W. *Chem. Phys.* **1981**, *59*, 47.

(43) Eisenstein, I.; Munn, R. W.; Bounds, P. J. *Chem. Phys.* **1983**, *74*, 307.

(44) Eisenstein, I.; Munn, R. W. *Chem. Phys.* **1983**, *77*, 47.

(45) Eisenstein, I.; Munn, R. W. *Chem. Phys.* **1983**, *79*, 189.

(46) Verlaak, S.; Heremans, P. *Phys. Rev. B* **2007**, *75*, 115127.

(47) Verlaak, S.; Beljonne, D.; Cheyns, D.; Rolin, C.; Linares, M.; Castet, F.; Cornil, J.; Heremans, P. *Adv. Funct. Mater.* **2009**, *19*, 3809.

(48) Linares, M.; Beljonne, D.; Cornil, J. r. m.; Lancaster, K.; Brédas, J.-L.; Verlaak, S.; Mityashin, A.; Heremans, P.; Fuchs, A.; Lennartz, C.; Idé, J.; Méreau, R. l.; Aurel, P.; Ducasse, L.; Castet, F. d. r. *J. Phys. Chem. C* **2010**, *114*, 3215.

(49) D'Avino, G.; Muccioli, L.; Zannoni, C.; Beljonne, D.; Soos, Z. G. *J. Chem. Theory Comput.* **2014**.

(50) Soos, Z. G.; Tsiper, E. V.; Pascal Jr, R. A. *Chem. Phys. Lett.* **2001**, *342*, 652.

(51) Tsiper, E. V.; Soos, Z. G. *Phys. Rev. B* **2003**, *68*, 085301.

(52) Topham, B. J.; Soos, Z. G. *Phys. Rev. B* **2011**, *84*, 165405.

(53) Sin, J. M.; Tsiper, E. V.; Soos, Z. G. *Europhys. Lett.* **2002**, *60*, 743.

(54) Dapprich, S.; Komáromi, I.; Byun, K. S.; Morokuma, K.; Frisch, M. J. *J. Mol. Struct. Theochem* **1999**, *461–462*, 1.

(55) Rappe, A. K.; Casewit, C. J.; Colwell, K. S.; Goddard, W. A.; Skiff, W. M. *J. Am. Chem. Soc.* **1992**, *114*, 10024.

(56) Breneman, C. M.; Wiberg, K. B. *J. Comput. Chem.* **1990**, *11*, 361.

(57) Rappé, A. K.; Goddard, W. A. *J. Phys. Chem.* **1991**, *95*, 3358.

CHAPTER 2

COMPUTATIONAL METHODS FOR THE DETERMINATION OF POLARIZATION ENERGY IN ORGANIC MOLECULAR CRYSTALS

In this Chapter, the methods necessary for the determination of the polarization energy in organic molecular crystals and methods of description of the non-bonded interactions in dimer structures are reviewed. As the problems this thesis is interested in scale from single molecules to thousands of molecules, a multiscale approach is necessary that utilizes both quantum and classical methodologies. We begin with the Schrödinger equation and then move onto approximate methods (*i.e.*, Hartree-Fock theory, Møller-Plesset Perturbation Theory, Symmetry-Adapted Perturbation Theory, and Density Functional Theory) used for electronic-structure calculations. This is followed by the description of the Distributed Multipole Analysis used for the calculation of electrostatic interactions between dimers. Lastly, the polarizable force field and molecular dynamics methods used for the determination of the polarization energy are described.

2.1 Electronic-Structure Theories

In this section, we present a brief discussion of the electronic-structure methods used for the parameterization of the AMOEBA (Atomic Multipole Optimized Energetics for Biomolecular Applications) force field and the energy decomposition analysis of non-bonding interactions. The notation used throughout this section has been adopted from Szabo and Ostlund.[1]

2.1.1 Schrödinger Equation

The primary tool to describe the quantum nature of a given system is the time-independent, non-relativistic Schrödinger equation:

$$\hat{\mathcal{H}}\left|\Psi_i\right\rangle = E_i\left|\Psi_i\right\rangle \tag{2.1}$$

where $\hat{\mathcal{H}}$ (given our interest in organic systems) is the non-relativistic Hamiltonian operator for a system of M nuclei and N electrons, $\left|\Psi_i\right\rangle$ is the wave function, and E_i is the energy. The Hamiltonian, in atomic units, is defined as:

$$\hat{\mathcal{H}} = \underbrace{-\sum_{i=1}^{N}\frac{1}{2}\nabla_i^2}_{1} \underbrace{-\sum_{A=1}^{M}\frac{1}{2M_A}\nabla_A^2}_{2} \underbrace{-\sum_{i=1}^{N}\sum_{A=1}^{M}\frac{Z_A}{r_{iA}}}_{3} \underbrace{+\sum_{i=1}^{N}\sum_{j>i}^{N}\frac{1}{r_{ij}}}_{4} \underbrace{+\sum_{A=1}^{M}\sum_{B>A}^{M}\frac{Z_A Z_B}{R_{AB}}}_{5} \tag{2.2}$$

where ∇_i^2 and ∇_A^2 are Laplacian operators that involve differentiation with respect to the coordinates of the *i*th electron and *A*th nucleus, M_A is the mass of the *A*th nucleus, Z_A is the atomic number of nucleus *A*, $r_{ij} = \left|r_i - r_j\right|$ is the distance between the *i*th and *j*th electrons, $r_{iA} = |r_i - R_A|$ is the distance between the *i*th electron and the *A*th nucleus, and $R_{AB} = |R_A - R_B|$ is the distance between the *A*th and *B*th nuclei. The first two terms of the Hamiltonian represent the kinetic energy of the electrons and nuclei, respectively, the third term represents the electron-nuclear attraction, the fourth term represents electron-electron repulsion, and the fifth term represents nuclear-nuclear repulsion.

The Schrödinger equation is intractable except for very simple (hydrogenoid) systems, therefore, a series of approximations are applied. We note that a first approximation, already applied above, is a neglect of relativistic effects, as their contributions do not become large until the investigation of 4th row elements. Second, because of the large difference (1836:1) between the masses of protons (1.672622 x 10^{-27} kg) and electrons (9.109382 x 10^{-31} kg) one can approximate the electrons to be moving in a field of fixed nuclei; this is referred to as the Born-Oppenheimer approximation. Within this approximation the second term, the kinetic energy of the nuclei, of Equation 2.2 may be neglected and the fifth term, the nuclear-nuclear repulsion, may be treated as a constant. The remaining terms define the electronic Hamiltonian describing the motion of a system of N electrons in a field of fixed nuclei:

$$\hat{\mathcal{H}}_{elec} = -\sum_{A=1}^{M} \frac{1}{2M_A} \nabla_A^2 - \sum_{i=1}^{N} \sum_{A=1}^{M} \frac{Z_A}{r_{iA}} + \sum_{i=1}^{N} \sum_{j>i}^{N} \frac{1}{r_{ij}} \tag{2.3}$$

Equation 2.3 then leads to the electronic Schrödinger equation:

$$\hat{\mathcal{H}}_{elec} \Psi_{elec} = E_{elec} \Psi_{elec} \tag{2.4}$$

where the electronic wave function depends only on the coordinates of the electrons for a given nuclear configuration. The total energy is then defined as:

$$E_{tot} = E_{elec} + E_{nuc} \tag{2.5}$$

where E_{nuc} is the nuclear repulsion energy.

The electronic Hamiltonian depends upon the spatial and spin coordinates of the electrons, with the many-electron wave function antisymmetric with respect to the interchange of any two electrons to obey the Pauli exclusion principle:

$$\Psi\left(\mathrm{x}_1, \mathrm{x}_i, \mathrm{x}_j, \ldots, \mathrm{x}_N\right) = -\Psi\left(\mathrm{x}_1, \mathrm{x}_j, \mathrm{x}_i, \ldots, \mathrm{x}_N\right) \tag{2.6}$$

While Equation 2.3 appears simpler than Equation 2.2 it is still intractable for systems consisting of more than one electron. To increase the tractability, the independent-particle approximation is used, where the electronic Schrödinger equation is transformed from a solution for a N-electron Hamiltonian to that of N one-electron Hamiltonians. The wave function then becomes a simple product of spin-orbital wave functions for each electron, known as the Hartree product:

$$\Psi^{HP}\left(\mathrm{x}_1, \mathrm{x}_2, \ldots, \mathrm{x}_N\right) = \chi_i\left(\mathrm{x}_1\right)\chi_j\left(\mathrm{x}_2\right)\cdots\chi_k\left(\mathrm{x}_N\right) \tag{2.7}$$

where spin orbitals are defined as:

$$\chi(\mathrm{x}) = \begin{cases} \psi(r)\alpha(\omega) \\ \quad or \\ \psi(r)\beta(\omega) \end{cases} \tag{2.8}$$

To ensure the anti-symmetry of the wave function, which the Hartree product does not, the many-electron wave function may be represented as a single Slater determinant:

$$\Psi\left(\mathrm{x}_1,\mathrm{x}_2,\ldots,\mathrm{x}_N\right)=\frac{1}{\sqrt{N!}}\begin{vmatrix}\chi_i\left(\mathrm{x}_1\right) & \chi_j\left(\mathrm{x}_1\right) & \cdots & \chi_k\left(\mathrm{x}_1\right)\\ \chi_i\left(\mathrm{x}_2\right) & \chi_j\left(\mathrm{x}_2\right) & \cdots & \chi_k\left(\mathrm{x}_2\right)\\ \vdots & \vdots & \ddots & \vdots\\ \chi_i\left(\mathrm{x}_N\right) & \chi_j\left(\mathrm{x}_N\right) & \cdots & \chi_k\left(\mathrm{x}_N\right)\end{vmatrix} \tag{2.9}$$

where $\frac{1}{\sqrt{N!}}$ is a normalization factor and $\chi\left(\mathrm{x}\right)$ are the one-electron spin orbitals. By use of a Slater determinant the interchange of any two electrons, corresponding to interchange of two rows, changes the sign of the determinant and if two electrons occupy the same spin orbital, corresponding to two columns being equal, the determinant is zero.

Throughout this Thesis, a number of electronic-structure theories are employed to model molecular systems and go beyond the very crude independent-particle approximation. The following sections will describe aspects of these theories, including Hartree-Fock theory, perturbation theories, and Density Functional Theory, which have been necessary for the work in the following Chapters.

2.1.2 Hartree–Fock Theory

Except for the simplest cases, such as H_2^+, solutions to the electronic Schrödinger equation involve many-electron problems resulting from the last term of Equation 2.3, the electron-electron repulsion. Thus the central approximation to electronic-structure theory and to solving these problems, is the Hartree–Fock approximation, through the Fock operator:

$$f\left(i\right)=-\frac{1}{2}\nabla_i^2-\sum_{A=1}^{M}\frac{Z_A}{r_{iA}}+\upsilon^{HF}\left(i\right) \tag{2.10}$$

Here, electron-electron interactions are introduced in an average way with $\upsilon^{HF}\left(i\right)$ the potential of the *i*th electron due to the *mean* field of the other electrons. This reduces the electron-electron repulsion term from a two-electron operator to a one-electron operator. The Hartree-Fock energy may then be defined using one- and two-electron integrals:

$$E_{HF}=\sum_{i}^{N}\langle i|h|i\rangle+\frac{1}{2}\sum_{ij}^{N}[ii\,|\,jj]-[ij\,|\,ji] \tag{2.11}$$

where the first term:

$$\langle i|h|i\rangle=\int d\mathrm{x}_1\chi_1^*\left(\mathrm{x}_1\right)\left\{-\frac{1}{2}\nabla_i^2-\sum_{A}^{M}\frac{Z_A}{r_{iA}}\right\}\chi_1\left(\mathrm{x}_1\right) \tag{2.12}$$

corresponds to the one-electron contribution to kinetic energy and the electron-nuclear attraction, and:

$$[ii\,|\,jj]=\int d\mathrm{x}_1 d\mathrm{x}_2\chi_i^*\left(\mathrm{x}_1\right)\chi_i\left(\mathrm{x}_1\right)\frac{1}{r_{12}}\chi_j^*\left(\mathrm{x}_2\right)\chi_j\left(\mathrm{x}_2\right) \tag{2.13}$$

And:

$$[ij\,|\,ji]=\int d\mathrm{x}_1 d\mathrm{x}_2\chi_i^*\left(\mathrm{x}_1\right)\chi_j\left(\mathrm{x}_1\right)\frac{1}{r_{12}}\chi_j^*\left(\mathrm{x}_2\right)\chi_i\left(\mathrm{x}_2\right) \tag{2.14}$$

are the two-electron Coulomb and exchange integrals, respectively. Since Equations 2.13 and 2.14 for the *i*th electron depend on the spin-orbitals of the other electrons the energy must be solved iteratively, through the so-called self-consistent-field (SCF) method. The spin-orbitals are typically defined as a linear combination of atomic orbitals to form molecular orbitals:

$$\chi_i = \sum_{\mu} C_{\mu}^{i} \phi_{\mu} \tag{2.15}$$

where C_{μ}^{i} are the expansion coefficients, and ϕ_{μ} are the atomic orbitals constructed from Gaussian-type orbitals (GTO):

$$\phi_{\mu}^{GTO}\left(r\right) = N x^{l} y^{m} z^{n} e^{-\zeta r^{2}} \tag{2.16}$$

where *N* is a normalization constant, *l*, *m*, and *n* are the integers used to describe the angular momentum of the orbitals, and ζ controls the diffusiveness of the orbital.

2.1.3 Møller-Plesset Perturbation Theory

Hartree-Fock is a mean-field theory that makes the assumption that each electron moves in the static field created by all of the other electrons. As such, instantaneous electron-electron interactions, also referred to as electron correlation, are not explicitly taken into account and are treated in an average way. To improve upon Hartree-Fock, dynamic electron correlation may be included. One such method is Møller-Plesset perturbation theory[2] wherein a small perturbation, defined as a sum of one-electron Fock operators, to the Hamiltonian is introduced:

$$\hat{\mathcal{H}}\Psi = \left(\hat{\mathcal{H}}_0 + \hat{\mathcal{H}}'\right)\Psi = E\Psi \tag{2.17}$$

To be able to systematically improve the eigenvalues of the Hamiltonian operator, it is necessary to switch between the unperturbed and perturbed states. This is accomplished through the introduction of an ordering parameter λ:

$$\hat{\mathcal{H}} = \left(\hat{\mathcal{H}}_0 + \lambda\mathcal{V}\right) \tag{2.18}$$

Expanding the exact eigenfunctions and eigenvalues in a Taylor series gives:

$$E_i = E_i^{(0)} + \lambda E_i^{(1)} + \lambda^2 E_i^{(2)} + \cdots \tag{2.19}$$

$$\left|\Psi_i\right\rangle = \left|\Psi_i^{(0)}\right\rangle + \lambda\left|\Psi_i^{(1)}\right\rangle + \lambda^2\left|\Psi_i^{(2)}\right\rangle + \cdots \tag{2.20}$$

where $E_i^{(n)}$ and $\Psi_i^{(n)}$ are the *n*th-order energy and wave function, respectively. Substituting Equations 2.19 and 2.20 into Equation 2.18 gives:

$$\begin{gathered}\left(\hat{\mathcal{H}}_0 + \lambda\mathcal{V}\right)\left(\left|\Psi_i^{(0)}\right\rangle + \lambda\left|\Psi_i^{(1)}\right\rangle + \lambda^2\left|\Psi_i^{(2)}\right\rangle + \ldots\right) = \\ \left(E_i^{(0)} + \lambda E_i^{(1)} + \lambda^2 E_i^{(2)} + \ldots\right)\left(\left|\Psi_i^{(0)}\right\rangle + \lambda\left|\Psi_i^{(1)}\right\rangle + \lambda^2\left|\Psi_i^{(2)}\right\rangle + \ldots\right)\end{gathered} \tag{2.21}$$

Expanding Equation 2.21 and collecting equal coefficients of λ^n gives a set of equations known as the *n*th-order Schrödinger equations:

$$\hat{\mathcal{H}}_0\left|\Psi_i^{(0)}\right\rangle = E_i^{(0)}\left|\Psi_i^{(0)}\right\rangle \tag{2.22}$$

$$\hat{\mathcal{H}}_0\left|\Psi_i^{(1)}\right\rangle + \mathcal{V}\left|\Psi_i^{(0)}\right\rangle = E_i^{(0)}\left|\Psi_i^{(1)}\right\rangle + E_i^{(1)}\left|\Psi_i^{(0)}\right\rangle \tag{2.23}$$

$$\hat{\mathcal{H}}_0\left|\Psi_i^{(2)}\right\rangle + \mathcal{V}\left|\Psi_i^{(1)}\right\rangle = E_i^{(0)}\left|\Psi_i^{(2)}\right\rangle + E_i^{(1)}\left|\Psi_i^{(1)}\right\rangle + E_i^{(2)}\left|\Psi_i^{(0)}\right\rangle \tag{2.24}$$

$$\hat{\mathcal{H}}_0 \left| \Psi_i^{(n)} \right\rangle + \mathcal{V} \left| \Psi_i^{(n-1)} \right\rangle = \sum_{n=0}^{k} E_i^{(n)} \left| \Psi_n^{(k-n)} \right\rangle \tag{2.25}$$

Multiplying each of Equations 2.22 through 2.25 by $\left\langle \Psi_i^{(0)} \right|$ gives the set of *n*th-order energies:

$$E_i^{(0)} = \left\langle \Psi_i^{(0)} \middle| \hat{\mathcal{H}}_0 \middle| \Psi_i^{(0)} \right\rangle \tag{2.26}$$

$$E_i^{(1)} = \left\langle \Psi_i^{(0)} \middle| \mathcal{V} \middle| \Psi_i^{(0)} \right\rangle \tag{2.27}$$

$$E_i^{(2)} = \left\langle \Psi_i^{(0)} \middle| \mathcal{V} \middle| \Psi_i^{(1)} \right\rangle \tag{2.28}$$

$$E_i^{(n)} = \left\langle \Psi_i^{(0)} \middle| \mathcal{V} \middle| \Psi_i^{(n-1)} \right\rangle \tag{2.29}$$

where the sum of the zeroth-order energy, $E_i^{(0)}$, and first-order energy correction, $E_i^{(1)}$, corresponds to the Hartree-Fock energy. Thus to improve upon Hartree-Fock theory, at least, a second-order correction must be made. Additional, higher-order corrections may be as computationally demanding as more accurate correlated methods, such as configuration interaction and coupled-cluster theories, and are often not considered. The second-order energy correction to Hartree-Fock is Equation 2.28 with the first-order perturbed wave function having the form:

$$\left| \Psi_i^{(1)} \right\rangle = \sum_{\mu \neq i} \frac{\left\langle \Psi_\mu^{(0)} \middle| \mathcal{V} \middle| \Psi_i^{(0)} \right\rangle}{E_i^{(0)} - E_\mu^{(0)}} \left| \Psi_\mu^{(0)} \right\rangle \tag{2.30}$$

Thus the second-order correction to the energy becomes:

$$E_o^{(2)} = \frac{1}{4}\sum_{ijab} \frac{\left[[ai\,|\,bj] - [aj\,|\,bi]\right]^2}{\epsilon_a + \epsilon_b - \epsilon_i - \epsilon_j} \tag{2.31}$$

where i and j are occupied spin orbitals, a and b are unoccupied spin orbitals, and ϵ_i, ϵ_j, ϵ_a, and ϵ_b are the orbital energies of the respective spin orbitals. The total MP2 energy is the sum of the zeroth-order, first-order, and second-order energy corrections.

2.1.4 Symmetry-Adapted Perturbation Theory

Non-covalent interactions are responsible for organic molecular crystal structures, provide a significant contribution to the secondary and tertiary structures of biological macromolecules such as proteins, and dictate the interactions between DNA base pairs.[3-5] These non-covalent interactions may be evaluated using a supramolecular approach where the binding energy:

$$E_{binding} = E_{monomerA}^{isolated} + E_{monomerB}^{isolated} - E_{dimer}^{complex} \tag{2.32}$$

or the interaction energy:

$$E_{interaction} = E_{dimer}^{complex} - E_{monomerA}^{complex} - E_{monomerB}^{complex} \tag{2.33}$$

may be calculated, or a perturbational approach may be used where interaction energy is treated as a perturbation and solved for directly. While a number of energy decomposition analysis methods have been proposed, perhaps the most well-defined method is Symmetry-Adapted Perturbation Theory (SAPT).[6] Within SAPT, the interaction energy may be directly calculated without the need to calculate the total energy of the system. This is done as a sum of several physically motivated terms:

$$E_{SAPT} = E_{elst}^{(1)} + E_{exch}^{(1)} + E_{ind}^{(2)} + E_{exch-ind}^{(2)} + E_{disp}^{(2)} + E_{exch-disp}^{(2)} \tag{2.34}$$

where $E_{elst}^{(1)}$, $E_{exch}^{(1)}$, $E_{ind}^{(2)}$, $E_{exch-ind}^{(2)}$, $E_{disp}^{(2)}$, $E_{exch-disp}^{(2)}$ represent the first-order electrostatic, first-order exchange, second-order induction, second-order exchange-induction, second-order dispersion, and second-order exchange-dispersion contributions, respectively. Often the contribution from $E_{exch-ind}^{(2)}$ and $E_{exch-disp}^{(2)}$ are grouped into the induction and dispersion terms, respectively, to give the total interaction energy as:

$$E_{SAPT} = E_{elst}^{(1)} + E_{exch}^{(1)} + E_{ind}^{(2)} + E_{disp}^{(2)} \tag{2.35}$$

Additional terms may be included to improve accuracy and completeness. SAPT has been the topic of a number of recent reviews.[7-9] Hence, only a cursory introduction to the energetic contributions will be provided.

2.1.4.1 Electrostatics

The electrostatic interactions between molecules may be described via a multipole expansion where the permanent or static multipole moments of the molecules interact. While valid at long-range, this approximation breaks down at short range as molecular orbital overlap increases. Although the multipole expansion may be constructed as to always converge, an error in the interaction energy, known as the penetration energy, increases as the molecular orbital overlap increases. Thus a proper description of the electrostatic energy requires the integration over the electron density of each monomer. The resulting attractive interaction due to charge interpenetration increases exponentially as the orbital overlap increases.

2.1.4.2 Exchange–Repulsion

The exchange is the most important repulsive component of the interaction energy at short-range, and is a result of the Pauli exclusion principle. The attractive component to exchange may be physically understood as an electron on one monomer tunneling to an orbital on the other in a dimer complex. On the other hand, the dominating repulsive term may be thought of in terms of two monomers beginning at infinite separation and being brought close together such that their electron densities overlap. At infinite separation, the electrons may distribute freely around their respective monomers, but as the two monomers are brought close together their densities overlap. The electrons within this overlap area are repelled from this area so that electrons of equivalent spin may not occupy the same space. This repulsion increases exponentially as the overlap increases. This term is often approximated with a $\frac{1}{r^{12}}$ term in many force fields, although other approximations may be used such as exponential terms to more accurately model the behavior of the exchange–repulsion.

2.1.4.3 Induction

The stabilizing induction term results from the relaxation of the electron density of one monomer in the static electric field of the other. This interaction may be considered as the interaction of the static multipoles of one monomer with the induced multipoles of the other. Since the electron density of one molecule changes in response to the field of the other the static field of the first molecule will change, thus necessitating the need to treat the induction self-consistently to accurately capture the induction contribution. Induction is rarely captured by force field methods. The polarizable force fields that attempt to capture the polarization of one molecule by another often do so through atom-centered induced dipoles. One example of such a force field will be discussed later.

2.1.4.4 Dispersion

Dispersion results from the interaction of instantaneous charge fluctuations, with the largest contribution a result of dipole-dipole fluctuations. For interacting nonpolar molecules the dispersion energy is the dominant attractive component, and is purely due to electron correlation. As discussed earlier, electron correlation is neglected in Hartree-Fock theory and thus requires, at a minimum, treatment by MP2. Empirical dispersion included in many force fields is often approximated pairwise as $\frac{C_6}{r^6}$, where C_6 comes from the atomic polarizabilities and r^{-6} is the distance between the two atomic centers.

2.1.5 Density Functional Theory

Density functional theory (DFT) attempts to solve the electronic Schrödinger equation using the electronic density instead of the wave function. The basis of DFT results from the seminal work of Hohenberg and Kohn[10] who have related the ground-state electronic energy to the electron density.

2.1.5.1 The Hohenberg-Kohn Theorems

The Hohenberg-Kohn theorems are the foundation upon which DFT is built. The first theorem states that the ground state density uniquely determines the Hamiltonian and all properties of the system. Another way of stating this is that the ground state energy is a unique functional of the electron density. The second theorem states that the ground state energy may be obtained variationally and that the electron density that minimizes the total energy is the exact ground state density. From this, the expectation value for a given observable may be defined as a functional of the electron density:

$$\langle A \rangle = A\left[\rho(r)\right] \tag{2.36}$$

and the energy may be defined as:

$$E\left[\rho(\mathrm{r})\right] = \langle \Psi | H | \Psi \rangle = T\left[\rho\right] + E_{Ne}\left[\rho\right] + E_{ee}\left[\rho\right] \tag{2.37}$$

where the Hamiltonian is composed of a kinetic energy component, T, a nuclear-electron attraction component, E_{Ne}, and an electron-electron repulsion component, E_{ee}; the electron density is defined as:

$$\rho(r) = N\int d^3r_2 \ldots \int d^3r_N \left|\Psi(r_1, r_2, \ldots, r_N)\right|^2 \tag{2.38}$$

The universal functional is introduced to encapsulate all electron-only contributions:

$$F[\rho] = \langle \Psi | T + V_{ee} | \Psi \rangle = T[\rho] + J[\rho] + E_{ncl}[\rho] \tag{2.39}$$

where the J and E_{ncl} are the Coulomb functional and non-classical correlation functional, respectively. The non-classical correlation functional incorporates the effects of self-interaction, exchange, and electron correlation.

2.1.5.2 Kohn-Sham Theory

As obtaining the exact kinetic energy term as a function of the electron density has been difficult, Kohn and Sham[11] proposed a formalism wherein the system is reduced from a system of interacting electrons in a static external potential to a system of non-interacting electrons in an effective potential. Such a system may be represented by a set of Kohn-Sham orbitals, ϕ_i, that constitute a Slater determinant representing the ground state wave function (Equation 2.9), for which the kinetic energy is exactly known:

$$T_s = -\frac{1}{2}\sum_i^N \langle \phi_i | \nabla^2 | \phi_i \rangle \tag{2.40}$$

The small energy difference that results from not using the true kinetic energy may be corrected for by other functionals, such that the universal functional becomes:

$$F[\rho] = T_s[\rho] + J[\rho] + E_{XC}[\rho] \tag{2.41}$$

where E_{XC} is the exchange-correlation energy that contains the correction of the kinetic energy and the non-classical electron correlation contribution.

$$E_{XC}[\rho] = (T[\rho] - T_s[\rho]) + (E_{ee}[\rho] - J[\rho]) = T_C[\rho] + E_{ncl}[\rho] \tag{2.42}$$

The total energy then becomes:

$$E[\rho] = T_s[\rho] + E_{Ne}[\rho] + J[\rho] + E_{XC}[\rho] \tag{2.43}$$

The corresponding Schrödinger equation is:

$$\left[-\frac{1}{2}\nabla^2 - \sum_A^M \frac{Z_A}{r_{iA}} + \int \frac{\rho(r_2)}{r_{12}} dr_2 + V_{XC}(r_1)\right]\phi_i = \varepsilon_i \phi_i \tag{2.44}$$

with the exchange-correlation potential, V_{XC}:

$$V_{XC} = \frac{\delta E_{XC}}{\delta \rho} \tag{2.45}$$

The exact form of the exchange-correlation potential is not known and must be approximated.

2.1.5.3 Approximate Functionals for Exchange and Correlation

As the exact form of the exchange-correlation energy is not known, approximations must be made. Three of the most common approximations are the local-density approximation, the generalized gradient approximation, and the use of hybrid functionals that include a portion of the exact exchange from Hartree-Fock.

2.1.5.3.1 Local density approximation

The simplest approximation for exchange-correlation is the local-density approximation upon which more sophisticated approximations are based. Within this approximation the functional is dependent only on the electron density at a given point:

$$E_{XC}^{LDA}[\rho] = \int \rho(r)\,\varepsilon_{XC}(\rho)\,dr \tag{2.46}$$

where ε_{XC} is the exchange-correlation energy per particle, and the electron density, ρ, is assumed to be slowly varying. For this approximation E_{XC}^{LDA} may be separated into exchange, E_X^{LDA}, and correlation, E_C^{LDA}, contributions such that:

$$E_{XC}^{LDA} = E_X^{LDA} + E_C^{LDA} \tag{2.47}$$

where the exchange, defined as:

$$E_X^{LDA}[\rho] = -\frac{3}{4}\left(\frac{3}{\pi}\right)^{1/3} \int \rho(r)^{4/3}\,dr \tag{2.48}$$

and the correlation contribution are not known exactly, except at the limits of high density and low density. Thus, for intermediate values of the electron density, Monte Carlo simulations of a homogenous electron gas are used for parameterization. Note that while the assumption of a slowly varying electron density holds for materials such as metals it may not necessarily for molecular materials. Popular local-density approximation correlation functionals include those developed by Perdew and Wang (PW),[12] Perdew and Zunger (PZ),[13] and Vosko, Wilk, and Nusair (VWN).[14]

2.1.5.3.2 Generalized gradient approximation

The generalized gradient approximation attempts to improve upon the local-density approximation by including information about the gradient of the electron density, $\nabla\rho$, at a given point as well as the electron density at that point, thus better accounting for the inhomogeneity of molecular systems. As such, the exchange-correlation energy may be represented by:

$$E_{XC}^{GGA}[\rho] = \int \rho(r)\,\varepsilon_{XC}^{GGA}\left(\rho_\alpha, \rho_\beta, \nabla\rho_\alpha, \nabla\rho_\beta\right)dr \tag{2.49}$$

which accounts for spin. Examples of popular generalized gradient approximation functionals for exchange and correlation include PBE from Perdew, Burke, and Ernzerhof and BLYP where the exchange is that of Becke (B88)[15] and the correlation is that of Lee, Yang, and Parr (LYP).[16]

2.1.5.3.3 Hybrid Functionals

The exchange contributions are generally much larger than the correlation contributions, thus improving the exchange expression will provide a significant improvement to the exchange-correlation functional. Additionally, it is has been shown that the exact exchange potential has a $1/r$ dependence, although the LDA and GGA display exponential decay.[17,18] One method of improvement, proposed by Becke,[15] is the inclusion of some portion of the exact Hartree-Fock exchange, which provides the correct asymptotic behavior, in the DFT exchange such that the exchange-correlation energy may be expressed as:

$$E_{XC} = a_0 E_X^{HF} + \left(1 - a_0\right) E_X^{DFT} + E_C^{DFT} \tag{2.50}$$

where a is a constant that may vary between 0 and 1. Of the many available hybrid functionals the B3LYP hybrid functional[19,20] is one of the most popular, with a functional form of:

$$E_{XC}^{B3LYP} = aE_X^{HF} + \left(1 - a\right) E_X^{LDA} + b\Delta E_X^{B88} + cE_C^{LYP} + \left(1 - c\right) E_C^{VWN} \tag{2.51}$$

where *a*, *b*, and *c* are optimized parameters with values of 0.20, 0.72, and 0.81, respectively. Additionally, parameter-free hybrid functionals such as PBE0 exist.[21,22]

2.2 Distributed Multipole Analysis

The distributed multipole analysis (DMA) of Stone[23-25] is a method by which to describe the charge distribution of a molecular system through a multipole expansion about a number of defined centers, often atomic positions. At each center there exists a multipole series consisting of charge, dipole, quadrupole, and higher-order terms derived from electronic structure calculations. This method allows the electrostatic multipole interactions between molecules to be accurately calculated, by distributing the molecule properties over a collection of points. Additionally, the distributed multipoles may be used for parameterization of the electrostatic component of force fields.

The charge density of a system may be represented as a sum of products of Gaussian functions with the form:

$$\rho(r,r') = \sum_{ab} P_{ab}\chi_a(r)\chi_b(r') \tag{2.52}$$

where P_{ab} is the coefficient corresponding to an element of the single-particle density matrix. From this, the overlap of each pair of Gaussian functions may be described by a single Gaussian, centered at a point between the centers of the two functions, which also contain regular spherical harmonics. These new Gaussians, that constitute the charge distribution, each possess multipole moments where the spherical harmonic multipole is defined as:

$$Q_{lk} = \int R_{lk}(r)\rho(r)dr \tag{2.53}$$

where R_{lk} is the associated regular solid harmonic and $\rho(r)$ is the total charge density. Based on an allocation algorithm, each new Gaussian is then moved to a new center, typically an atomic center. Note that there are various algorithms available to determine the new Gaussian center, from simply choosing the atom closest to the current Gaussian center to more complex weighted, grid-based schemes.[26,27]

The multipole moments that may be calculated at each center are limited by the angular momentum of the spherical harmonics associated with the overlap, $l+l'$. For example, two *s* orbitals of rank 0 may be entirely represented by a point charge, one *s* orbital and one *p* orbital may be represented by a point charge and dipole vector, and two *p* orbitals require a point charge, dipole vector, and quadrupole tensor to be properly described.

Additional multipole methods beyond that of Stone have been proposed by Rein,[28] Sokalski and Poirier,[29] Vigné-Maeder and Claverie,[30] and Amos and Crispin.[31]

2.3 Molecular Dynamics

In order to simulate large ensembles of molecules, necessary for the description of bulk materials and macroscopic properties, approximate methods must be used that allow for the treatment of 1000s of points in space. Molecular dynamics provides a method by which a trajectory may be obtained to describe the motion of particles within a bulk material according to Newton's second equation:

$$-\frac{dV}{dr} = m\frac{d^2r}{dt^2} \tag{2.57}$$

As the properties of the system, as a function of time, are of interest in molecular dynamics the size of the time steps taken must be smaller than the rate of the fastest process of importance. Molecular vibrations occur on a timescale of 10^{11}-10^{14} s^{-1} requiring time steps on the order of 10^{-15} s^{-1}, *i.e*., on the femtosecond scale.

The forces between the points and the potential energy are defined by molecular mechanics forces fields. These force fields are comprised of a set of parameters that define the potential energy using terms for different interactions, as described in Section 2.4. These force fields must be optimized through, often tedious, parameterization schemes that require iteratively updating initial parameters, obtained from experiment or from quantum-mechanical calculations, by comparison to known bulk properties. While molecular mechanics and molecular dynamics might appear at first sight to be quite similar, an important distinction between the two must be made. Namely, molecular mechanics focuses on static pictures, while molecular dynamics employs molecular mechanics to describe the motion of particles.

2.4 The AMOEBA Force Field

Many organic molecular crystals are composed of molecules where the largest non-zero multipole moment is the quadrupole. To be able to properly describe the electrostatic interactions in these systems, while still allowing the scale necessary (1000s of atoms), molecular mechanics force fields that include higher-order multipoles are necessary. As we are modeling the polarization energy in these systems, it is also necessary that our model be able to react to the presence of an excess charge. The AMOEBA (Atomic Multipole Optimized Electrostatics for Biological Applications) molecular mechanics force field of Ponder and co-workers[32-34] meets all of these requirements. AMOEBA is composed of a series of eight energy components:

$$U = U_{bond} + U_{angle} + U_{oop} + U_{torsion} + U_{b\theta} + U_{vdW} + U_{elec}^{static} + U_{elec}^{ind} \qquad (2.54)$$

The first five terms, *i.e.*, the stretching, bending, out-of-plane bending, torsion, and stretch-bend terms are adopted from Allinger's MM3 force field,[35] and the van der Waals term is a dampened 14-7 Lennard-Jones potential. The final two terms represent electrostatic contributions in the form of static multipole and induced-dipole interactions.

The static multipole interaction term defines the influence of the multipole moments, M_i, of atom *i* on the multipole moments, M_j, of atom *j* through the interaction operator, T_{ij} :

$$U_{elec}^{static}\left(r_{ij}\right) = M_i^T T_{ij} M_j \tag{2.55}$$

where all static interactions from charge-charge to dipole-dipole interactions through quadrupole-quadrupole interactions, including cross terms, are taken into account.

Induced-dipole interactions are calculated in a self-consistent manner through a combination of direct and mutual induction contributions:

$$\mu_{i,a}^{ind}\left(n+1\right) = \left(1-\omega\right)\mu_{i,a}^{ind}\left(n\right) + \omega\left[\mu_{i,a}^{ind}\left(0\right) + \alpha_i \sum_{\{j'\}} T_{\alpha\beta}^{ij'} \mu_{j',\beta}^{ind}\left(n\right)\right] \tag{2.56}$$

where ω controls the rate of convergence and the direct induction, $\mu_{i,\alpha}^{ind}\left(0\right)$, is the resulting induced-dipole component on atom *i* with atomic polarizability α due to all static charge, dipole, and quadrupole moments not within the same polarization group; here, a polarization group is defined as a small group of atoms with negligible charge such as a methyl group, or as an ensemble of similar atoms such as a conjugated backbone. The direct induction is a function of the static electric field and thus does not vary.

The mutual induction is a function of the induced dipoles on other atomic sites and must be solved self-consistently, where all atomic sites are allowed to interact. To prevent the induced dipoles from approaching infinity at short-range, a smearing function, ρ, is used to modify the dipole term such that one site in the pair interaction may be described as:[36,37]

$$\rho = (3a/4\pi)\exp\left(-au^3\right) \tag{2.57}$$

where a is a dimensionless width parameter that controls the amount of smearing and u is an effective distance that is a function of the distance between the two sites and their respective atomic polarizabilities.

Additional information on the AMOEBA force field including application to test sets and complete parameterization are available.[32-34,38]

2.4.1 Parameterization of AMOEBA for the Calculation of Electronic Polarization Energy

The parameterization of the electrostatic component of the AMOEBA force field for the calculation of the electronic polarization energy requires a series of 5 steps. First, the molecular structure for a single molecule is extracted from available crystal structures. The single-particle density matrix is then calculated for the isolated molecule in the neutral, radical-cation, and radical-anion states in the crystalline geometry. A distributed multipole analysis is then performed to obtain atom-centered charges, dipoles, and quadrupoles in spherical tensor form. These spherical tensor multipoles are then converted to Cartesian format.

To allow for the use of the atom-centered multipoles in the AMOEBA force field the multipole tensors must be rotated from the global coordinate frame to a local coordinate frame. This local coordinate frame is defined for each atom center such that the origin is located at the atom of interest, *i*, with the line connected to a directly bonded atom, *j*, defining the *z*-axis. An atom, *k*, adjacent to *i* is selected such that *i*-*j*-*k* forms an acute angle with the *x*-axis lying in the *i*-*j*-*k* plane and the *y*-axis defined as perpendicular to the *x*- and *z*-axes. These local coordinate multipole tensors are then inserted directly into the AMOEBA force field. Atom types are defined for each atomic center and additional, necessary force field parameters are adapted from analogous atoms within the force field, or from MM3.

2.5 Programs Used

All quantum mechanics, molecular mechanics, and molecular dynamics methods used for calculations in the subsequent Chapters have been employed as implemented in the following software suites:

Gaussian 09 (revisions A.02, B.01, C.01, and D.01),[39] PSI4 beta-5,[40] Molpro 2012,[41] GDMA 2.2,[24] Tinker (versions 5.0, 6.0, 6.1, 6.3, and 7.0),[42] and ZINDO.[43-45] All crystal structures were obtained from the Cambridge Crystallographic Database[46] or directly from research groups as indicated, with structures analyzed using Mercury 3.0.[47] Custom scripts were developed for bulk system construction and data analysis. The script of Dr. Trent Parker (Georgia Institute of Technology) was used for the analysis of intermolecular electrostatic multipole interactions based upon the equations of A. J. Stone.[25]

2.6 References

(1) Szabo, A.; Ostlund, N. S. *Modern Quantum Chemistry: Introduction to Advanced Electronic Structure Theory*; Dover: New York, 1996.

(2) Møller, C.; Plesset, M. S. *Phys. Rev.* **1934**, *46*, 618.

(3) Li, S.; Cooper, V. R.; Thonhauser, T.; Lundqvist, B. I.; Langreth, D. C. *J. Phys. Chem. B* **2009**, *113*, 11166.

(4) Jurečka, P.; Hobza, P. *J. Am. Chem. Soc.* **2003**, *125*, 15608.

(5) Hohenstein, E. G.; Parrish, R. M.; Sherrill, C. D.; Turney, J. M.; Schaefer, H. F. *J. Chem. Phys.* **2011**, *135*, 174107.

(6) Szalewicz, K. *WIREs Comput. Mol. Sci.* **2012**, *2*, 254.

(7) Jeziorski, B.; Moszynski, R.; Szalewicz, K. *Chem. Rev.* **1994**, *94*, 1887.

(8) Hesselmann, A.; Jansen, G.; Schutz, M. *J. Chem. Phys.* **2005**, *122*, 014103.

(9) Hohenstein, E. G.; Sherrill, C. D. *J. Chem. Phys.* **2010**, *132*, 184111.

(10) Hohenberg, P.; Kohn, W. *Phys. Rev.* **1964**, *136*, B864.

(11) Kohn, W.; Sham, L. J. *Phys. Rev.* **1965**, *140*, A1133.

(12) Perdew, J. P.; Wang, Y. *Phys. Rev. B* **1992**, *45*, 13244.

(13) Perdew, J. P.; Zunger, A. *Phys. Rev. B* **1981**, *23*, 5048.

(14) Vosko, S. H.; Wilk, L.; Nusair, M. *Can. J. Phys* **1980**, *58*, 1200.

(15) Becke, A. D. *Phys. Rev. A* **1988**, *38*, 3098.

(16) Lee, C.; Yang, W.; Parr, R. G. *Phys. Rev. B* **1988**, *37*, 785.

(17) van Leeuwen, R.; Baerends, E. J. *Phys. Rev. A* **1994**, *49*, 2421.

(18) March, N. H. *Phys. Rev. A* **1987**, *36*, 5077.

(19) Becke, A. D. *J. Chem. Phys.* **1993**, *98*, 5648.

(20) Stephens, P. J.; Devlin, F. J.; Chabalowski, C. F.; Frisch, M. J. *J. Phys. Chem* **1994**, *98*, 11623.

(21) Perdew, J. P.; Ernzerhof, M.; Burke, K. *J. Chem. Phys.* **1996**, *105*, 9982.

(22) Adamo, C.; Barone, V. *J. Chem. Phys.* **1999**, *110*, 6158.

(23) Stone, A. J. *Chem. Phys. Lett.* **1981**, *83*, 233.

(24) Stone, A. J. *J. Chem. Theory Comput.* **2005**, *1*, 1128.

(25) Stone, A. J. *The Theory of Intermolecular Forces*; Clarendon Press: Oxford, 1996.

(26) Murray, C. W.; Handy, N. C.; Laming, G. J. *Mol. Phys.* **1993**, *78*, 997.

(27) Stone, A. J. *J. Chem. Theory Comput.* **2005**, *1*, 1128.

(28) Rein, R. *Adv. Quantum Chem.* **1973**, *7*, 335.

(29) Sokalski, W. A.; Poirier, R. A. *Chem. Phys. Lett.* **1983**, *98*, 86.

(30) Vigne-Maeder, F.; Claverie, P. *J. Chem. Phys.* **1988**, *88*, 4934.

(31) Amos, A. T.; Crispin, R. J. *Molec. Phys.* **1976**, *31*, 159.

(32) Ponder, J. W.; Wu, C.; Ren, P.; Pande, V. S.; Chodera, J. D.; Schnieders, M. J.; Haque, I.; Mobley, D. L.; Lambrecht, D. S.; DiStasio, R. A.; Head-Gordon, M.; Clark, G. N. I.; Johnson, M. E.; Head-Gordon, T. *J. Phys. Chem. B* **2010**, *114*, 2549.

(33) Ren, P.; Ponder, J. W. *J. Comput. Chem.* **2002**, *23*, 1497.

(34) Ren, P.; Ponder, J. W. *J. Phys. Chem. B* **2003**, *107*, 5933.

(35) Lii, J. H.; Allinger, N. L. *J. Am. Chem. Soc.* **1989**, *111*, 8576.

(36) Thole, B. T. *Chem. Phys.* **1981**, *59*, 341.

(37) van Duijnen, P. T.; Swart, M. *J. Phys. Chem. A* **1998**, *102*, 2399.

(38) Wu, J. C.; Chattree, G.; Ren, P. *Theor. Chem. Acc.* **2012**, *131*, 1138.

(39) Frisch, M. J.; Trucks, G. W.; Schlegel, H. B.; Scuseria, G. E.; Robb, M. A.; Cheeseman, J. R.; Scalmani, G.; Barone, V.; Mennucci, B.; Petersson, G. A.; Nakatsuji, H.; Caricato, M.; Li, X.; Hratchian, H. P.; Izmaylov, A. F.; Bloino, J.; Zheng, G.; Sonnenberg, J. L.; Hada, M.; Ehara, M.; Toyota, K.; Fukuda, R.; Hasegawa, J.; Ishida, M.; Nakajima, T.; Honda, Y.; Kitao, O.; Nakai, H.; Vreven, T.; Montgomery Jr., J. A.; Peralta, J. E.; Ogliaro, F.; Bearpark, M. J.; Heyd, J.; Brothers, E. N.; Kudin, K. N.; Staroverov, V. N.; Kobayashi, R.; Normand, J.; Raghavachari, K.; Rendell, A. P.; Burant, J. C.; Iyengar, S. S.; Tomasi, J.; Cossi, M.; Rega, N.; Millam, N. J.; Klene, M.; Knox, J. E.; Cross, J. B.; Bakken, V.; Adamo, C.; Jaramillo, J.; Gomperts, R.; Stratmann, R. E.; Yazyev, O.; Austin, A. J.; Cammi, R.; Pomelli, C.; Ochterski, J. W.; Martin, R. L.; Morokuma, K.; Zakrzewski, V. G.; Voth, G. A.; Salvador, P.; Dannenberg, J. J.; Dapprich, S.; Daniels, A. D.; Farkas, Ö.; Foresman, J. B.; Ortiz, J. V.; Cioslowski, J.; Fox, D. J.; Gaussian, Inc.: Wallingford, CT, USA, 2009.

(40) Turney, J. M.; Simmonett, A. C.; Parrish, R. M.; Hohenstein, E. G.; Evangelista, F. A.; Fermann, J. T.; Mintz, B. J.; Burns, L. A.; Wilke, J. J.; Abrams, M. L.; Russ, N. J.; Leininger, M. L.; Janssen, C. L.; Seidl, E. T.; Allen, W. D.; Schaefer, H. F.; King, R. A.; Valeev, E. F.; Sherrill, C. D.; Crawford, T. D. *WIREs Comput. Mol. Sci.* **2012**, *2*, 556.

(41) Werner, H.-J.; Knowles, P. J.; Knizia, G.; Manby, F. R.; Schütz, M.; Celani, P.; Korona, T.; Lindh, R.; Mitrushenkov, A.; Rauhut, G.; Shamasundar, K. R.; Adler, T. B.; Amos, R. D.; Bernhardsson, A.; Berning, A.; Cooper, D. L.; Deegan, M. J. O.; Dobbyn, A. J.; Eckert, F.; Goll, E.; Hampel, C.; Hesselmann, A.; Hetzer, G.; Hrenar, T.; Jansen, G.; Köppl, C.; Liu, Y.; Lloyd, A. W.; Mata, R. A.; May, A. J.; McNicholas, S. J.; Meyer, W.; Mura, M. E.; Nicklass, A.; O'Neill, D. P.; Palmieri, P.; Peng, D.; Pflüger, K.; Pitzer, R.; Reiher, M.; Shiozaki, T.; Stoll, H.; Stone, A. J.; Tarroni, R.; Thorsteinsson, T.; Wang, M. MOLPRO, version 2012.1, a package of ab initio programs. Published Online: 2012.

(42) Ponder, J. W. *TINKER: Software Tools for Molecular Design*, 2012.

(43) Ridley, J.; Zerner, M. *Theor. Chim. Acta* **1973**, *32*, 111.

(44) Mataga, N.; Nishimoto, K. *Z. Phys. Chem. (Muenchen, Ger.)* **1957**, *13*, 140.

(45) Nishimoto, K.; Mataga, N. *Z. Phys. Chem. (Muenchen, Ger.)* **1957**, *12*, 335.

(46) Allen, F. H. *Acta Crystallogr.* **2002**, *B58*, 380.

(47) Macrae, C. F.; Bruno, I. J.; Chisholm, J. A.; Edgington, P. R.; McCabe, P.; Pidcock, E.; Rodriquez-Monge, L.; Taylor, R.; Streek, J. v. d.; Wood, P. A. *J. Appl. Cryst.* **2008**, *41*, 466.

CHAPTER 3

ELECTRONIC POLARIZATION IN OLIGOACENE MOLECULAR CRYSTALS: DESCRIPTION VIA A POLARIZABLE FORCE FIELD

3.1 Introduction

As discussed in Chapter 1, organic materials based on π-conjugated molecules and polymers have garnered considerable interest as the active layers in crystalline and thin-film electronic and electro-optic applications.[1-6] Regardless of the device architecture and function, the rates of charge-carrier transport generally constitute a determining factor in device efficiency and are intimately dependent on the strength of the electronic couplings between adjacent molecules, the extent of geometric and lattice relaxation upon ionization, and differences in the site energies (*i.e.*, the variations in the molecular ionization energies and electron affinities). Each of these parameters, and in particular the latter, are influenced by the polarization effects in the solid-state environment.[7-12]

Here, we build upon previous work[13,14] and employ an approach that makes use of a polarizable force field in order to describe the bulk polarization under vertical ionization conditions. From these calculations we extract, exclusively, the electronic polarization, *i.e.*, the polarization energy neglecting nuclear motion. To demonstrate the general applicability of this model, we study the oligoacene crystal series and two perfluorinated acenes; the latter are of technological interest as perfluoropentacene behaves as an efficient n-channel transport material with electron transport mobilities up to 0.22 cm^2 V^{-1} s^{-1}.[15] As the molecules under study do not present permanent dipole moments, multipole-quadrupole interactions become the primary electrostatic interactions in the neutral organic crystals. Hence, the AMOEBA force field of Ponder and co-workers[16-18] was chosen as the polarizable force field for the study as it includes multipole-quadrupole interactions through quantum-mechanically derived parameters and polarization is accounted for through the creation and interaction of induced dipoles with other static multipoles. This work has been published in *The Journal of Physical Chemistry C*, **2013**, 117, 13853.[19]

3.2 Computational Methodology

Our studies of the polarization in the oligoacenes were performed on the following crystal structures obtained from the Cambridge Structural Data[20] (CSD identification codes are noted within parentheses) with no further modification: naphthalene (NAPHTA06),[21] anthracene (ANTCEN09),[22] tetracene (TETCEN01),[23] pentacene (PENCEN04),[24] perfluoronaphthalene (OFNAPH01),[25] and perfluoropentacene (BEZLUO).[15]

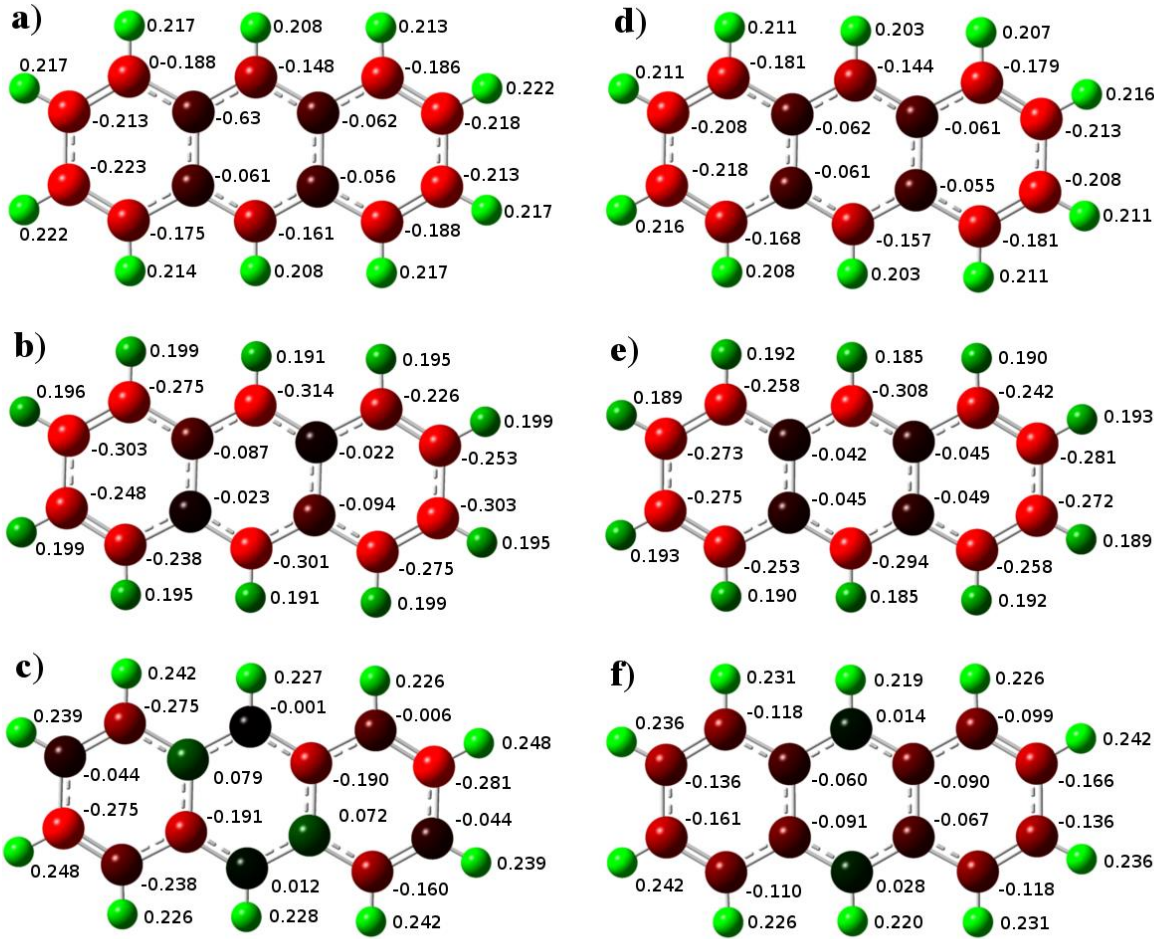

Figure 3.1. Representation of the NBO charge distribution and accompanying charge values as determined at the MP2/6-31+G(d,p) (left) and CCSD/6-31+G(d,p) (right) levels of theory for the neutral (a, d), radical-anion (b, e), and radical-cation (c, f) states of naphthalene. Atoms with net positive charges are represented in green, those with negative charges in red, and those that remain essentially neutral in black.

The AMOEBA force field, described in detail in Section 2.4, was parameterized according to Section 2.4.1 wherein a single molecule is extracted from the respective crystal structure and the single-particle density matrices for the neutral, radical-cation, and radical-anion states were determined through single-point energy calculations using second-order Møller-Plesset perturbation theory (MP2) in a 6-31+G(d,p) basis[26,27] as implemented in the

Gaussian 09 (revision A.02) software suite.[2829] As a check for accuracy, single-point coupled-cluster computations with single and double excitations (CCSD) were also carried out; see Figure 3.1. These charge distribution calculations show quantitatively modest and qualitatively no difference versus MP2.

The single-particle density matrices are then used as input for a distributed multipole analysis[30] to generate atom-centered multipoles as parameters. It is important to note that the molecular geometries are "frozen" to those extracted from the crystals during the evaluations of the different redox states and that subsequent electronic polarization energies determined through the methodology described here refer solely to those corresponding to vertical ionization processes, a constraint that allows us to focus solely on the electronic polarization (*i.e.*, solving only for the terms E_{qQ} and E_{id} from Equation 1.6 as additional multipole contributions should be small).[12,14]

Single-point energy calculations are then performed within the Tinker software suite using the newly derived parameters for both isolated molecules and clusters of varying size. Spherical clusters[31,32] were constructed where molecules with their center-of-mass inside a given radius were selected from a larger supercell and the charged molecule was set at the center of the cluster; see Figure 3.2. For calculations of the charged states, the atom types of the central molecule were replaced with those of the radical-cation or radical-anion, whose parameters were defined in a way analogous to the neutral species. The polarization energies, $P_{\pm}$, were then determined using the gas-phase and solid-state ionization energies and electron affinities according to Equations 3.1 and 3.2.

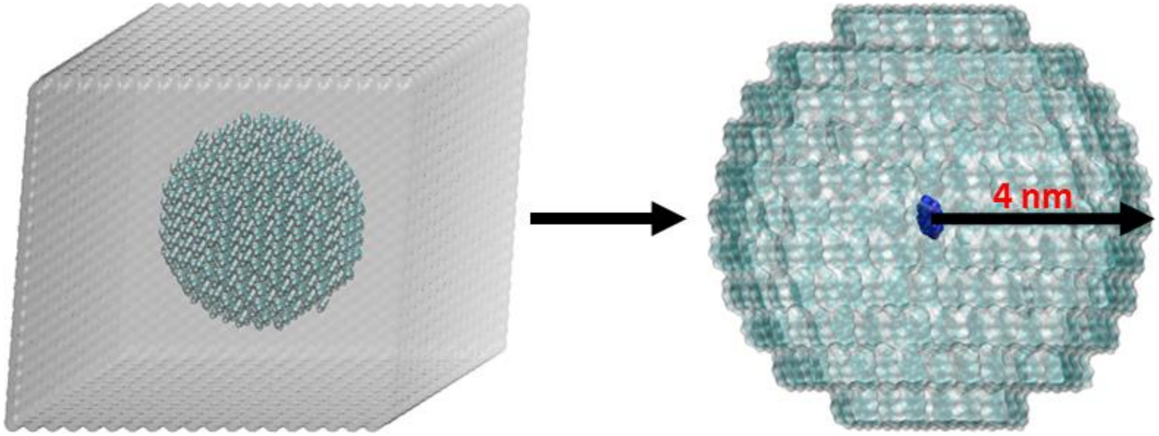

Figure 3.2. Naphthalene cluster (4 nm) cut from a larger supercell where the center-of-mass of the cluster is located at the center-of-mass of the molecules closest to the center of the supercell. The location of the charge naphthalene located at the center of the spherical cluster is shown in blue.

3.3 Results and Discussion

3.3.1 Polarization Energy Model Validation

The oligoacenes, as noted previously, present no permanent dipole moment due to symmetry; as a result, the quadrupole is the largest non-zero multipole and is the dominant component influencing the intermolecular electrostatic interactions. For the oligoacenes studied here, the herringbone packing motif found in the crystal leads to favorable positive-moment–negative-moment interactions among the quadrupole moments on neighboring molecules,[33] as schematically depicted in Figure 3.3 using the MP2/6-31+G(d,p)-derived values for isolated molecules. Importantly, as the redox state of the molecule changes, there is a large change in the electrostatic potential (ESP) profile of the molecule that in turn alters the interactions within the polarizable environment. We note that the naphthalene molecule extracted from the crystal has a modest twist along the backbone plane that induces a slight asymmetry in the ESP of the radical cation. For the radical anion, the ESPs show clear evidence of increased negative charge above/below the plane of the molecular backbone (*i.e.*, the π cloud of the aromatic structure); in the radical cation, there occurs a shift of the relative negative charge distribution to the ends (long axis) of the molecule. These shifts in electron density in turn affect the magnitude and sign of the multipole parameters.

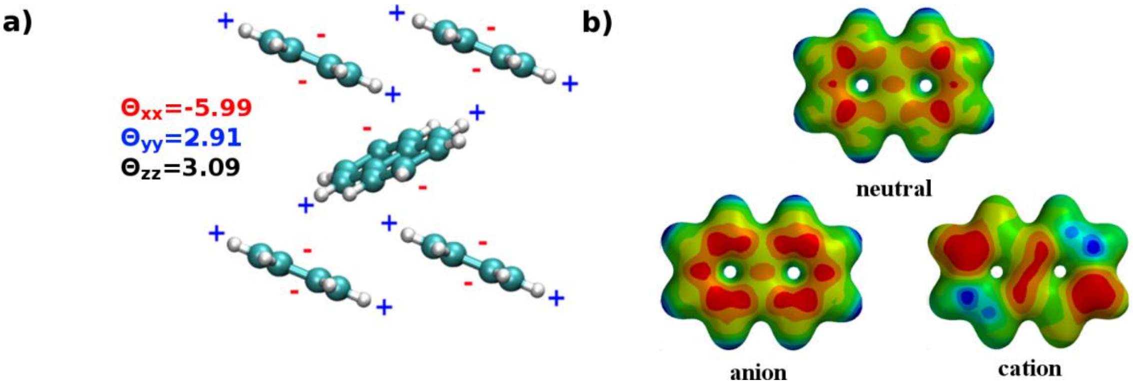

Figure 3.3. (a) Representation of the naphthalene crystal herringbone packing motif and quadrupole-quadrupole interactions for a neutral system with quadrupole moments (Debye Å) calculated at the MP2/6-31+G(d,p) level for isolated molecules. The quadrupole moments are with respect to the normal (*x*), long (*z*), and short (*y*) axes. (b) Plots of the electrostatic potentials (iso-surface value = 0.03 $e/\text{Å}^3$) for the neutral, radical-anion, and radical-cation states of naphthalene in the crystalline geometry at the MP2/6-31+G(d,p) level of theory. Red areas represent areas of electron accumulation and blue areas show electron deficiency.

As stated earlier, quadrupole moments are paramount to the description of oligoacene polarization in the solid state. Therefore, our model must have the capacity to reproduce the molecular quadrupole moments. Indeed, as shown in Table 3.1, the quadrupoles derived from our parameterized model present the same sign and relative magnitude as those from MP2, displaying qualitative agreement. The model data for naphthalene also compare favorably, if slightly smaller, to experimental data reported by Munn[34] and those previously reported at the MP2/6-311++G(2d,2p) level of theory.[14] For the perfluorinated species, we note that the model-derived multipoles are significantly larger than those determined through MP2 calculations; while the cause of this is not immediately evident, the relative differences between the naphthalene/perfluoronaphthalene and pentacene/perfluoropentacene pairs are similar, and we therefore expect similar trends in the comparison. We recall that the charge-quadrupole interaction scales as $1/r^5$, so the differences between our model quadrupole moments and those derived from MP2 will have minor impact on the polarization energies.

Table 3.1. Principal quadrupole moments (Debye Å) of the neutral oligoacenes as determined at the MP2/6-32+G(d,p) level and using our parameterized model with respect to the normal (*x*), long (*z*), and short (*y*) axes.

	MP2			*AMOEBA*		
	θ_{xx}	θ_{yy}	θ_{zz}	θ_{xx}	θ_{yy}	θ_{zz}
Naphthalene	-5.99	2.91	3.09	-2.96	1.36	1.59
	-14.36[a]	7.24[a]	7.11[a]			
	-13.31[b]	6.14[b]	7.17[b]			
Anthracene	-8.29	3.80	4.50	-6.75	2.48	4.27
Tetracene	-10.59	4.49	6.10	-7.41	2.45	4.96
Pentacene	-12.93	5.59	7.34	-12.08	4.29	7.79
Perfluoronaphthalene	6.71	-3.70	-3.01	22.30	-12.30	-9.96
Perfluoropentacene	17.07	-8.61	-8.46	54.69	-29.04	-25.65

[a] Determined at the MP2/6-311++G(2d,2p) level of theory and reported in Reference 14.
[b] Derived from theoretical calculations scaled to the experimental results of benzene in Reference 34.

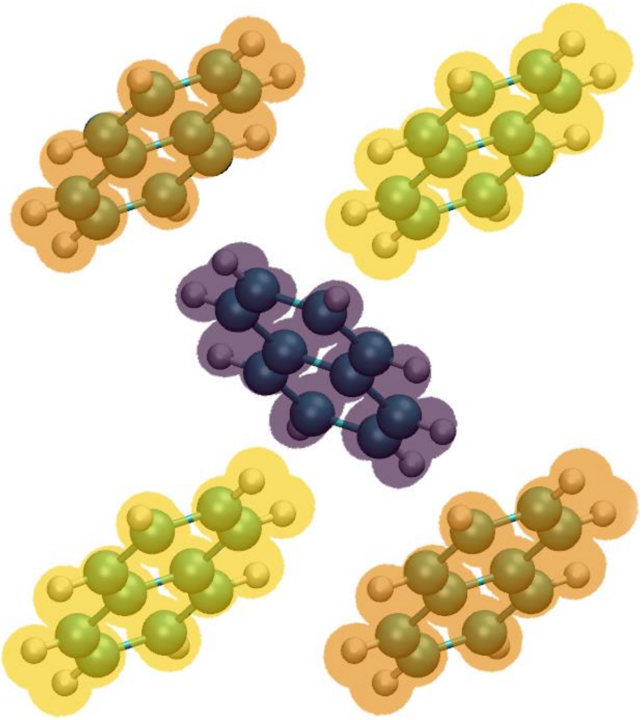

Figure 3.4. Magnitudes of the dipoles induced on the nearest molecules to a negatively charged naphthalene (central molecule). The molecules in yellow have induced dipoles of 0.094 Debye, and those in orange, of 0.084 Debye.

We now turn to how our model performs with regard to describing electrostatic interactions in the solid state. Using the basic (five-molecule) herringbone packing unit for naphthalene as a model and taking the central molecule to carry an excess electron (Figure 3.4), the model produces differences in the induced-dipole moments on the neighboring naphthalene molecules as one would expect due to the differences in position and orientation with respect to the central charged naphthalene. Those molecules that interact with the face of the central anion have a larger induced dipole (0.094 D) versus those that interact with the edge (0.084 D), *i.e.*, a difference of 11%. When the central molecule is charged, the charge-quadrupole term becomes the dominant electrostatic interaction responsible for the polarization asymmetry.[35] Considering the relative molecular quadrupole orientation shown in Figure 3.3, the large induced-dipole moments occur for the two molecules where the positive poles of the quadrupole point directly towards the central negative charge, and lead to the, albeit relatively small, asymmetry in the induced-dipole moments.

3.3.2 Bulk Polarization in Linear Oligoacenes

As our model is able to account for variations in electrostatic interactions in small model clusters, we now expand our view to probe the electronic polarization in the bulk oligoacene crystals. To create clusters representative of the bulk materials a supercell was constructed from which spherical clusters were extracted by fixing the radius of the sphere at the center-of-mass of the molecule closest to the origin of the original unit cell within the supercell. The clusters we consider vary in size from a radius of 1 nm (~10 molecules) through a radius of 3 to 4 nm (100s-1000s of molecules). This upper limit to the cluster size has been determined reasonable as there is minimal change to the polarization energy as the cluster size increases beyond 4 nm; for instance, P_+ and P_- for naphthalene show differences of less than 0.02 eV between 3 and 4 nm radius clusters (Figure 3.5). As the charge-quadrupole and induced-dipole effects are short-range, the variations in polarization energy are larger for smaller clusters, but quickly saturate for larger clusters. Note that for the larger clusters the change in the polarization energy remains mainly a function of induced-dipole interactions as these interactions act through a cascade effect that feeds through the system.

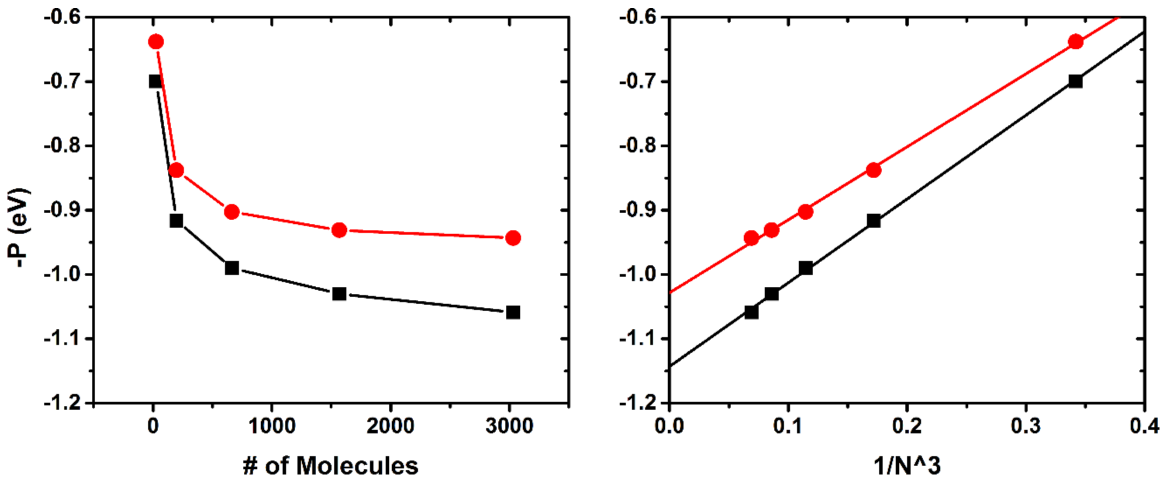

Figure 3.5. (Left) The polarization energy in naphthalene versus the number of molecules in the clusters. The points represent clusters of 1, 2, 3, 4, and 5 nm radii. There is about 0.01 eV difference between the two largest clusters considered. (Right) The polarization energy plotted *vs.* $N^{-1/3}$, where N is the number of molecules in the cluster.

To determine the bulk polarization energies, the cluster polarization energies were extrapolated to infinity *vs*. the inverse of the cube of the number of molecules in the cluster due to the spherical nature of the extracted systems ($N^{-1/3}$, Figure 3.5). The polarization energies for the oligoacene series are presented in Table 3.2 alongside available experimental data. Expanding the oligoacene structure from naphthalene to anthracene through tetracene and pentacene, the characteristic trends observed experimentally emerge with the present model:

(i) The magnitude of P_+ decreases by 0.1 eV as the oligoacenes become large; from 1.14 eV in naphthalene to 1.02 eV in pentacene;

(ii) P_+ is more stabilizing than P_- due to the nature of the charge-quadrupole interaction, in agreement with the results of Bounds and Munn;[36,37]

(iii) the correct polarization asymmetry is obtained in view of the experimental data reported by Sato *et al*.[10]

Table 3.2. Comparison of our current model and experimental data for the bulk polarization energy of naphthalene, anthracene, tetracene, pentacene, and the perfluorinated species.

(eV)	P_+		P_-	
	This Work	Exp.[10]	This Work	Exp.[10]
Naphthalene	-1.14	-1.72	-1.03	-1.10
Anthracene	-1.11	-1.65	-0.85	-1.09
Tetracene	-1.04	-1.63[a]	-0.92	-0.92[b]
Pentacene	-1.02	-1.63	-0.79	-1.17
Perfluoronaphthalene	-0.76	---	-1.18	---
Perfluoropentacene	-0.50	---	-1.27	---

[a]Refs. 38 & 39. [b]Ref. 40.

The polarization energies for our calculations are of the same order of magnitude as those determined experimentally, increasing from 0.1 to 0.2 eV as the oligoacene length increases versus the 0.1-0.7 eV differences determined in earlier theoretical works.[14,41,42] We note, however, that the magnitude of the asymmetry is smaller in our calculations *vs.* experiment, a function of the fact that our focus is solely on the electronic polarization and that we currently neglect potential stabilization from geometric and lattice relaxation, charge delocalization, and stabilizing charge penetration effects.[21, 25] The inclusion of some or all of these effects may greatly increase the agreement between the model results and experimental evaluations.

To compare the current model with the earlier QMMM method of Reference 14, it is important to note the contrasting methods by which the charge and higher-order interactions are accounted. The QMMM model used the self-consistent charge-equilibration scheme (QEq) of Rappé and Goddard,[43] employing point charges located at atom centers and allowing them to fluctuate in response to a charged molecule. The point charges fluctuate based on a feedback loop with electronic-structure calculations where: (i) the charged molecule is treated quantum mechanically; (ii) all other atoms are treated as charged points; and (iii) the values of these charged points equilibrate in a self-consistent fashion in response to the charge distribution on the quantum-mechanically treated molecule. Though this method allows for the net atomic charges representing the bulk material to fluctuate and in essence model polarization, it does not include terms for the quadrupole and induced-dipole interactions that Bounds and Munn[55, 60] have shown to be necessary to accurately model the bulk polarization (especially in the oligoacenes). Note that while the quadrupole and induced-dipole interactions are indirectly accounted for in the QEq model the quality of these descriptions is questionable. For point charge models it is difficult to reproduce the quadrupoles of molecular systems with even qualitative accuracy without the use of auxiliary charges.[44] Thus, because of this deficiency the quadrupoles in the QEq model are most likely to be qualitatively incorrect, and therefore, the magnitude of the quadrupole, induced dipoles, and quadrupole – induced-dipole interactions are likely to be incorrect, resulting in the reversal of the polarization asymmetry observed in the QMMM model. Our current model, however, does allow for interactions among charges, dipoles, and quadrupoles through a static picture that provides for the appropriate asymmetry of polarization in response to positive and negative charges.

The lack of charge equilibration in our current model, though, can also account somewhat for the smaller overall $P_{\pm}$ compared to the QMMM model.

It should be noted that our current model and the previously implemented models all display a trend for P_{-} that is in relative disagreement with experimental results, namely a decrease of P_{-} with increasing oligoacene length. We observe a decrease of 0.24 eV in P_{-} compared to a very small increase of 0.07 eV measured via electron capture techniques; however, it must be borne in mind that these values are smaller than the *ca*. 0.5 eV experimental resolution, and that this trend may not be experimentally discernible.[45-47] The reason for the decreasing polarization energy has not been detailed in earlier work; as with the polarization energy due to a positive charge carrier, it is likely an effect of the increased charge delocalization in the longer oligoacenes.

There is also evidence of an odd-even effect regarding the polarization asymmetry of the oligoacenes. Anthracene and pentacene (odd-numbered ring systems) show an asymmetry of 0.26 and 0.23 eV, respectively, while naphthalene and tetracene (even-numbered ring systems) both have a polarization asymmetry of 0.11 eV. The reason behind this odd-even effect is not clear at this time, but it is of interest that the systems with an even number of fused ring display one-half the polarization asymmetry as the odd-numbered ring structures.

3.3.3 Effects of Changing Molecular Quadrupole on Polarization Energy

We now turn our attention to the perfluorinated oligoacenes as a further test of the model. The strong electron-withdrawing nature of the fluorine atoms reverses the bond polarity for the C–F bond *vs*. the C–H bond, leading to a reversal of sign of the principal quadrupole moments. These trends are evident when comparing the ESP maps of pentacene and perfluoropentacene; see Figure 3.6.

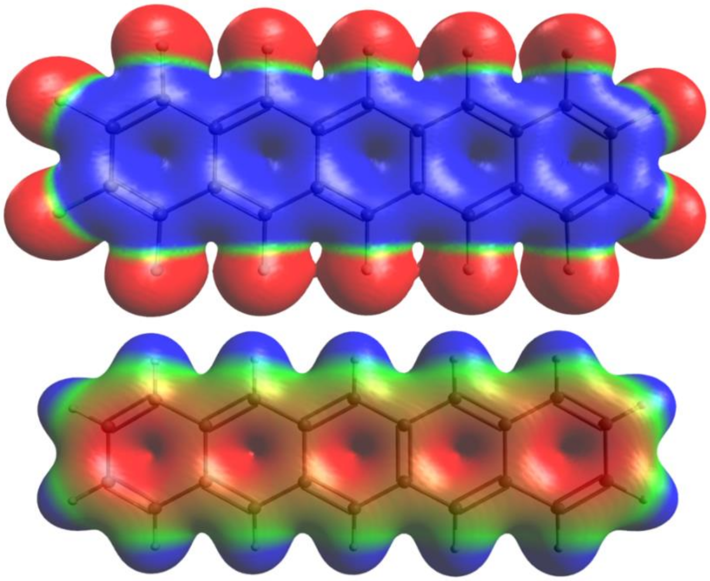

Figure 3.6. ESP map (iso-surface value = 0.03 e/Å^3) of pentacene (top) and perfluoropentacene (bottom) as determined at the MP2/6-31+G(d) level of theory. Red areas represent areas of electron accumulation and blue areas show electron deficiency.

For both perfluoronaphthalene and perfluoropentacene, P_- is more stabilizing than P_+ by more than 0.4 eV (Table 3.2); this is a direct function of the changes in sign of the principal quadrupole moments due to the substitution of the electron withdrawing fluorine atoms that result in a change of sign in the charge-quadrupole interactions. We note that there is also an apparent change in trend of the polarization energy as a function of the oligoacene length: perfluoronaphthalene has a larger P_+ versus perfluoropentacene, as is the case for the unsubstituted oligoacenes, whereas P_- is larger for perfluoropentacene, in contrast with the trends of the unsubstituted oligoacenes. As the number of perfluorinated systems experimentally available is limited, it is difficult to establish the reliability of this trend, especially as the consequences due to the differences in polarization as a function of odd-even effects could be playing a role.

3.4 Conclusions

We have employed a methodology that makes use of a polarizable force field to evaluate the bulk electronic polarization energy due to the presence of a localized charge carrier in organic molecular crystals. This method has been applied to unsubstituted and perfluorinated oligoacenes in order to demonstrate general applicability. As our focus was strictly on electronic polarization, effects due to geometric and lattice relaxations, charge delocalization, and charge penetration were not taken into account. These effects, in conjunction with that of the induced dipoles highlighted here, are needed to obtain a more robust understanding of polarization.

The electronic polarization energy results presented are in good qualitative agreement with experimental polarization energies both in terms of the magnitude and progression of the polarization energies when going from naphthalene to pentacene. The asymmetry of the

P_+ and P_- polarization in the oligoacenes is also qualitatively well described with respect to experimental data. On a more quantitative level, while the polarization asymmetries generated here are approximately a factor of 2-5 smaller than those observed experimentally, they are about three times larger than those given in earlier works based on INDO. As our method correctly predicts the experimental trends, we expect the model used here to be a reliable descriptor of bulk polarization in organic molecular solids as well as of polarization effects at materials interfaces.

3.5 References

(1) Tang, C. W. *Appl. Phys. Lett.* **1986**, *48*, 183.

(2) Tang, C. W.; VanSlyke, S. A. *Appl. Phys. Lett.* **1987**, *51*, 913.

(3) Garnier, F.; Horowitz, G.; Peng, X.; Fichou, D. *Adv. Mater.* **1990**, *2*, 592.

(4) Burroughes, J. H.; Bradley, D. D. C.; Brown, A. R.; Marks, R. N.; Mackay, K.; Friend, R. H.; Burns, P. L.; Holmes, A. B. *Nature* **1990**, *347*, 539.

(5) O'Regan, B.; Gratzel, M. *Nature* **1991**, *353*, 737.

(6) Kippelen, B.; Bredas, J. L. *Ener. Envir. Sci.* **2009**, *2*, 251.

(7) Lyons, L. E. *J. Chem. Soc.* **1957**, 5001.

(8) Silinsh, E. A. *Organic Molecular Crystals: Their Electronic States*; Springer: New York, 1980.

(9) Sato, N.; Seki, K.; Inokuchi, H. *J. Chem. Soc., Faraday Trans. 2* **1981**, *77*, 1621.

(10) Sato, N.; Inokuchi, H.; Silinsh, E. A. *Chem. Phys.* **1987**, *115*, 269.

(11) Griffith, O. L.; Anthony, J. E.; Jones, A. G.; Shu, Y.; Lichtenberger, D. L. *J. Am. Chem. Soc.* **2012**, *134*, 14185.

(12) Silinsh, E. A.; Čápek, V. *Organic Molecular Crystals: Interaction, Localization, and Transport Phenomena*, 1994.

(13) The QM/MM scheme displayed polarization magnitudes in agreement with experimental results, but the ordering of the polarization was reversed, with respect to the sign of the charge carrier.

(14) Norton, J. E.; Brédas, J.-L. *J. Am. Chem. Soc.* **2008**, *130*, 12377.

(15) Sakamoto, Y.; Suzuki, T.; Kobayashi, M.; Yuan, G.; Inoue, Y.; Tokito, S. *Mol. Cryst. Liq. Cryst.* **2006**, *444*, 225.

(16) Ren, P.; Ponder, J. W. *J. Comput. Chem.* **2002**, *23*, 1497.

(17) Ren, P.; Ponder, J. W. *J. Phys. Chem. B* **2003**, *107*, 5933.

(18) Ponder, J. W.; Wu, C.; Ren, P.; Pande, V. S.; Chodera, J. D.; Schnieders, M. J.; Haque, I.; Mobley, D. L.; Lambrecht, D. S.; DiStasio, R. A.; Head-Gordon, M.; Clark, G. N. I.; Johnson, M. E.; Head-Gordon, T. *J. Phys. Chem. B* **2010**, *114*, 2549.

(19) Ryno, S. M.; Lee, S. R.; Sears, J.; Risko, C.; Bredas, J. L. *J. Phys. Chem. C* **2013**, *117*, 13853.

(20) Allen, F. H. *Acta Crystallogr.* **2002**, *B58*, 380.

(21) Brock, C. P.; Dunitz, J. D. *Acta Crystallogr., Sect. B: Struct. Sci.* **1982**, *38*, 2218.

(22) Brock, C. P.; Dunitz, J. D. *Acta Crystallogr., Sect. B: Struct. Sci.* **1990**, *46*, 795.

(23) Holmes, D.; Kumaraswamy, S.; Matzger, A. J.; Vollhardt, K. P. C. *Chem. Eur. J.* **1999**, *5*, 3399.

(24) Mattheus, C. C.; Dros, A. B.; Baas, J.; Meetsma, A.; Boer, J. L. d.; Palstra, T. T. M. *Acta Crystallogr., Sect. C: Cryst. Struct. Commun.* **2001**, *57*, 939.

(25) Akhmed, N. A. *Russ. J. Struct. Chem.* **1973**, *14*, 573.

(26) Rick, S. W.; Stuart, S. J. *Rev. Comput. Chem.* **2002**, *18*, 89.

(27) Halgren, T. A.; Damm, W. *Curr. Opin. Struct. Biol.* **2001**, *11*, 236.

(28) Frisch, M. J.; Trucks, G. W.; Schlegel, H. B.; Scuseria, G. E.; Robb, M. A.; Cheeseman, J. R.; Scalmani, G.; Barone, V.; Mennucci, B.; Petersson, G. A.; Nakatsuji, H.; Caricato, M.; Li, X.; Hratchian, H. P.; Izmaylov, A. F.; Bloino, J.; Zheng, G.; Sonnenberg, J. L.; Hada, M.; Ehara, M.; Toyota, K.; Fukuda, R.; Hasegawa, J.; Ishida, M.; Nakajima, T.; Honda, Y.; Kitao, O.; Nakai, H.; Vreven, T.; Montgomery Jr., J. A.;

Peralta, J. E.; Ogliaro, F.; Bearpark, M. J.; Heyd, J.; Brothers, E. N.; Kudin, K. N.; Staroverov, V. N.; Kobayashi, R.; Normand, J.; Raghavachari, K.; Rendell, A. P.; Burant, J. C.; Iyengar, S. S.; Tomasi, J.; Cossi, M.; Rega, N.; Millam, N. J.; Klene, M.; Knox, J. E.; Cross, J. B.; Bakken, V.; Adamo, C.; Jaramillo, J.; Gomperts, R.; Stratmann, R. E.; Yazyev, O.; Austin, A. J.; Cammi, R.; Pomelli, C.; Ochterski, J. W.; Martin, R. L.; Morokuma, K.; Zakrzewski, V. G.; Voth, G. A.; Salvador, P.; Dannenberg, J. J.; Dapprich, S.; Daniels, A. D.; Farkas, Ö.; Foresman, J. B.; Ortiz, J. V.; Cioslowski, J.; Fox, D. J.; Gaussian, Inc.: Wallingford, CT, USA, 2009.

(29) We note that the 6-31+G(d,p) basis was chosen to provide the capability to scale the method described here to larger systems.

(30) Stone, A. J. *J. Chem. Theory Comput.* **2005**, *1*, 1128.

(31) We note that care needs to be taken during construction of the clusters as even slight asymmetry can lead to spurious results.

(32) Tsiper, E. V.; Soos, Z. G. *Phys. Rev. B* **2003**, *68*, 085301.

(33) Williams, J. H. *Acc. Chem. Res.* **1993**, *26*, 593.

(34) Eisenstein, I.; Munn, R. W. *Chem. Phys.* **1983**, *77*, 47.

(35) In these charged systems the charge-quadrupole interaction will be the primary interaction that results in asymmetry of the polarization energy, and the splitting will of opposite signs for holes and electrons. This splitting, though, may not be equivalent depending on the charge distribution along the molecule.

(36) Bounds, P. J.; Munn, R. W. *Chem. Phys.* **1981**, *59*, 41.

(37) The charge interaction energy is proportional to the charge on the species multiplied by the quadrupole moment and divided by the distance between the quadrupole point and the charge point.

(38) Pope, M.; Burgos, J.; Giachino, J. *J. Chem. Phys.* **1965**, *43*, 3367.

(39) Berry, R. S.; Jortner, J.; Mackie, J. C.; Pysh, E. S.; Rice, S. A. *J. Chem. Phys.* **1965**, *42*, 1535.

(40) Ando, N.; Mitsui, M.; Nakajima, A. *J. Chem. Phys.* **2008**, *128*, 154318.

(41) Verlaak, S.; Heremans, P. *Phys. Rev. B* **2007**, *75*, 115127.

(42) Soos, Z. G.; Tsiper, E. V.; Pascal Jr, R. A. *Chem. Phys. Lett.* **2001**, *342*, 652.

(43) Rappé, A. K.; Goddard, W. A. *J. Phys. Chem.* **1991**, *95*, 3358.

(44) Here, auxiliary charges refer to additional point charges, generally, placed above and below the plane of bonding of the atom center.

(45) Lyons, L. E.; Morris, G. C.; Warren, L. J. *J. Phys. Chem.* **1968**, *72*, 3677.

(46) Wentworth, W. E.; Chen, E.; Lovelock, J. E. *J. Phys. Chem.* **1966**, *70*, 445.

(47) Lyons, L.; Morris, G.; Warren, L. *Aust. J. Chem.* **1968**, *21*, 853.

CHAPTER 4

IMPACT OF MOLECULAR PACKING ON ELECTRONIC POLARIZATION IN ORGANIC MOLECULAR CRYSTALS: THE CASE OF PENTACENE VS TIPS-PENTACENE

4.1 Introduction

Organic molecular crystals, such as the oligoacenes and their substituted derivatives (*e.g.*, rubrene, alkylsilylethynyl-substituted acenes, or heteroatom-substituted acenes), often serve as representative systems to develop an understanding of the electronic and optical phenomena in π-conjugated electro-active materials.[1-14] Overall, these molecular materials are held together through the interplay among electrostatic (multipole) interactions, dispersion and induction effects, and short-range exchange-repulsion terms.[15-17] A detailed understanding of how these intermolecular interactions determine the available molecular packing arrangements, for both crystalline and disordered materials, is necessary if the full power of computational materials chemistry is to be used to design systems presynthesis, from isolated molecules to bulk packing, and design the material's (*e.g.*, electronic and optical) properties. Increasingly sophisticated methodologies are under development with the goal of predicting molecular packing through a variety of theoretical approaches and are being applied to systems that range from molecular crystals to proteins.[18-22]

The conjugated backbones of molecular- and polymer-based electronic materials are often appended with linear, branched, and other types of bulky alkyl-based chains to increase solubility and aid in the formulation of inks for solution deposition/printing. However, there is only sparse study of the interplay between electrostatic interactions and molecular packing in bulk solids as a function of the variations in substitution patterns. UPS investigations by Lichtenberger and co-workers started to address this issue by comparing the polarization energies of oligoacenes to their tri-iospropylsilylethynyl (TIPS)-substituted counterparts.[23-25] Interestingly, these studies revealed large variations in the evolution of the ionization energy (IE) on going from the gas phase to the solid state as a result of the addition of the TIPS functionality. Lichtenberger and co-workers measured that, in the gas phase, the IEs for pentacene and TIPS-pentacene were 6.54 and 6.28 eV, respectively, indicating that TIPS-pentacene is intrinsically better able to stabilize the resulting positive charge as expected from its more extended conjugation.[25] In thin films, however, pentacene is measured to have a considerably larger polarization energy (1.73 eV; solid-state IE of 4.81 eV) compared to TIPS-pentacene (0.44 eV; solid-state IE of 5.84 eV). Similar trends are observed for the anthracene- and tetracene-based systems.[26,29,30] While results from Kahn and co-workers[31,32] provide the same qualitative evolutions for TIPS-pentacene and pentacene the magnitude of the polarization energies differ considerably; in their studies, the polarization energy of TIPS-pentacene is 1.24 eV (corresponding to an IE of 5.04 eV), while that of pentacene is only 0.24 eV larger, 1.49 eV (solid-state IE of 5.05 eV).[26,27]

The quantitative variations found between the data from Kahn and co-workers and those from Lichtenberger and co-workers could be related to the differences in the nature of the

TIPS-pentacene films used in the photoelectron spectroscopy studies: The measurements from Kahn and co-workers employed a film derived from a polystyrene:TIPS-pentacene blend that is expected to lead to an ordered TIPS-pentacene layer through stratification of TIPS-pentacene at the air interface, while the pristine TIPS-pentacene film grown directly on a polycrystalline gold foil in the work of Lichtenberger and co-workers is suspected to be more disordered.[31,33-35] Hence, these variations, in principle, point to the impact that morphology – which can include deviations in the packing configurations and orientations induced by interactions with the substrate or film processing protocol or grain boundaries – can have on the polarization properties of molecular-based materials, which is addressed in this Chapter. We note that the large differences in the polarization energies of pentacene and TIPS-pentacene were initially suggested by Lichtenberger and co-workers to be a result of the reduced packing density in TIPS-pentacene (1.104 g/cm^3) compared to (crystalline) pentacene (1.314 g/cm^3).[25]

It is also worth pointing out that the trends concerning the electrochemical oxidation potentials of TIPS-pentacene and pentacene are not clear, as they have been shown to be nearly identical in *o*-dichlorobenzene[25] but differ by some 0.3 V in a 0.1 M solution of Bu_4NPF_6 in dichloromethane (with pentacene being more readily oxidized).[28] These discrepancies underline the extreme caution that must be exercised when extrapolating solution electrochemical data to the solid state.[29]

The goal of this Chapter is to investigate the impact of the nature of the packing configurations on the solid-state electronic polarization energies in the pentacene and TIPS-pentacene systems. Pentacene (and other unsubstituted oligoacenes) packs in a herringbone motif, while TIPS-pentacene displays a well-defined two-dimensional brickwork packing configuration (that can be further altered by the nature of the alkyl groups on the silyl moiety and/or substitution on the acene backbone);[30-32] the packing configurations of TIPS-anthracene and TIPS-tetracene differ from herringbone or brickwork packing and assume configurations intermediate to those found for pentacene and TIPS-pentacene. Our results demonstrate that the smaller bulk electronic polarization energy of TIPS-pentacene is mainly related to the differences in the nature of the electrostatic interactions, involving the monopole, quadrupole, and induced-dipole moments, that arise from the variations in (explicitly crystalline) packing configurations.[16,41-43] This work has been published in the *Journal of the American Chemical Society*, **2014**, 136, 6421.[33]

4.2 Computational Methodology

The geometries of the isolated molecules were extracted from the experimentally determined structures as reported in the Cambridge Structural Database: anthracene (ANTCEN09),[34] tetracene (TETCEN01),[35] pentacene (PENCEN04),[36] and TIPS-pentacene (VOQBIM).[30] Additionally, structures for TIPS-anthracene and TIPS-tetracene were provided by Professor J. E. Anthony at University of Kentucky. For the sake of comparison, we have also considered brickwork pentacene geometries. These were adapted from TIPS-pentacene structures in which the TIPS functionalities are removed; the 6 and 13 positions of pentacene are then capped with a hydrogen atom in the position of the *sp*-carbon that was removed. Quadrupole and electrostatic potential data were calculated at the MP2/6-31+G(d,p) level as implemented in the Gaussian 09 (revision B.01) software suite.[37] Polarizability data were obtained with the INDO Hamiltonian using the Mataga-Nishimoto potential to describe the Coulomb repulsion via the ZINDO program.[38-40]

Using the crystal packing configurations, dimers were extracted as sets of neighboring molecules. Total interaction energies and magnitudes of the non-covalent interactions were determined via symmetry-adapted perturbation theory (SAPT) as implemented in the Psi4 code with the SAPT0 truncation in jun-cc-pvdz basis.[15,17,53-5941] The distributed multipole analysis (DMA) algorithm as implemented in the Molpro program[42] was used, at the restricted Hartree-Fock level with the 6-311G(d,p) basis set, to evaluate atom-centered multipoles through the 32-pole. The electrostatic interactions were calculated using a script based on the derivations of A. J. Stone.[43]

All classical force-field calculations on dimers and clusters were carried out with the Tinker software suite[44] using the AMOEBA force field,[45-47] parameterized as described in Chapter 2. Interaction energies were calculated using the GROUP-INTER and GROUP-MOLECULE keywords to exclude intramolecular interactions.

Polarization energy calculations were carried out using the methodology previously described in Chapter 3. Spherical clusters were constructed where molecules with a center-of-mass within a given radius were extracted from a larger supercell. The central molecule is either neutral of takes a negative/positive charge. The polarization energy for a given cluster was calculated using the Lyons model with the bulk polarization energy being determined by increasing the cluster radius and plotting the calculated polarization energies versus $1/N^3$, where N is the number of molecules in the cluster.

It is important to keep in mind that positively and negatively charged molecules may have different intermolecular interactions with their environments, leading to an asymmetry in the polarization energies, *i.e.*, P_+ is not necessarily equivalent to P_-. For instance, as shown below, the induced-dipole moments resulting from the excess charges may act to stabilize the system to different amounts depending on the sign of the excess charge.

4.3 Results and Discussion

4.3.1 Electronic Properties of Isolated Molecules

We first examine the electrostatic properties of the isolated molecules and then turn to dimer to study the intermolecular forces at play and how they change as a function of the molecular packing configurations. Note that our focus will be directed towards pentacene and TIPS-pentacene, as similar trends are obtained for the other acenes considered.

The electrostatic potentials (ESP) reveal that the electron density is distributed in a similar manner in both pentacene and TIPS-pentacene, and that the attraction/repulsion of a test charge is comparable in both systems; see Figure 4.1. As neither pentacene nor TIPS-pentacene possesses a permanent molecular dipole moment, the molecular quadrupole moments dominate the intermolecular electrostatic interactions. In pentacene, a large positive quadrupole component is positioned along the long axis of the backbone (*z*-axis) with a smaller positive quadrupole component along the backbone short axis (*y*-axis); a large negative component lies normal to the backbone (*x*-axis), see Figure 4.1. These quadrupole components make intuitive sense given that the slightly positively charged hydrogen atoms lie along the periphery of the pentacene backbone plane (defined here as the *yz*-plane), while the π electron density is perpendicular (*x*-axis) to the molecular plane. TIPS-pentacene shares a similar positive quadrupole component along the long axis (*z*-axis), while the presence of TIPS groups makes the *y*-axis quadrupole component larger as compared to pentacene; again, the component perpendicular to the backbone is large and negative. The linear polarizabilities, likewise, are similar for the two molecules. Hence, based on such modest dissimilarities in the electrostatics and polarizabilities of the isolated molecules, one might not expect *a priori* the large differences in polarization energy measured for these systems.

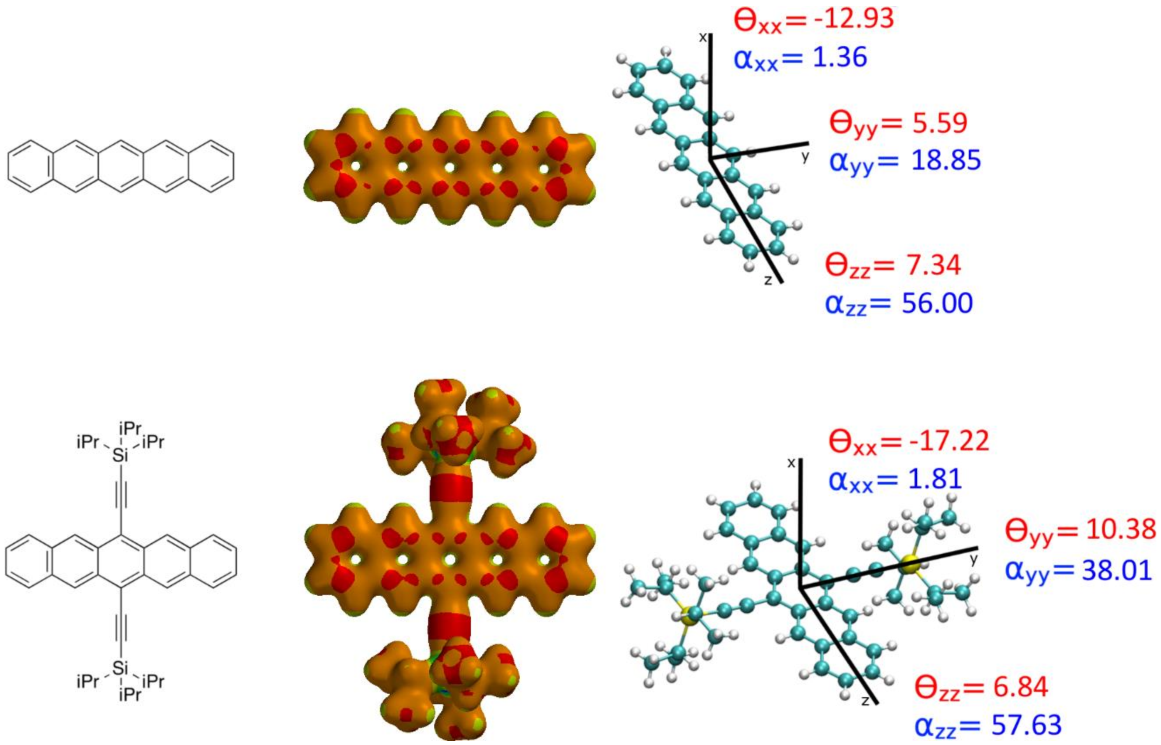

Figure 4.1. Chemical structures of pentacene (top left) and TIPS-pentacene (bottom left) and ball-and-stick models (right) that display the principal components of the quadrupole (θ, in units of Debye Å) and polarizability (α, in units of Å^3) tensors. Quadrupole data were derived from calculations at the MP2/6-31+G(d,p) level, while polarizability data were obtained with the INDO Hamiltonian. (Center) Electrostatic potential surface (iso-value of 0.03 e/Å^3) of pentacene (top) and TIPS-pentacene (bottom). The electron attraction/repulsion of the acene backbones are similar in both molecules. Note the color scale of both systems are equal and shifted due to the highly attractive region associated with the Si atoms of TIPS-pentacene.

4.3.2 Electrostatic Interactions in Crystalline Dimers and Small Clusters

We now turn our attention to pentacene and TIPS-pentacene dimers to obtain insight into the non-covalent interactions at play in the solid state. In particular, we will focus on the interplay among the stabilizing electrostatic, dispersion, and induction interactions and the destabilizing interactions due to electron exchange, through SAPT0-based energy decomposition analyses. Of relevance to our comparison between pentacene and TIPS-pentacene are the number of studies on stacked benzene dimers (and derivatives thereof) and the effect of moving from perfectly co-facial (sandwich) configurations to slip-stack and T-shape geometries.[48-55] We note that an important result from these investigations is that simple multipole descriptions of intermolecular interactions do break down for substituted benzene dimers in co-facial configurations at short distances (3.45 Å – 3.95 Å).[15] This is related to the increased significance of electrostatic charge penetration, an effect that is not taken into account in current force-field-based methodologies describing solid-state polarization (however, since we are not interested here in optimizing crystal structures but rather use experimentally determined structures, this feature does not alter the conclusions of our classical force-field studies).

To better understand how functionality and packing affect the intermolecular interactions in pentacene and TIPS-pentacene, we have considered three model systems: (i) the herringbone pentacene dimer, taken from the pentacene crystal structure; (ii) the brickwork TIPS-pentacene dimer, taken from the TIPS-pentacene crystal structure; and (iii) a brickwork pentacene dimer derived from the TIPS-pentacene crystal, with the TIPS functionalities replaced by hydrogen atoms. It is important to note that previous studies have used idealized structures for consideration of the non-bonded interactions. The systems that are of interest here, being experimentally determined, are not idealized from both a rotational and displacement perspective. For example, the herringbone pentacene is not perfectly T-shaped having an offset angle of 52° from ideal. The SAPT0 total energies and energy decompositions are reported in Table 4.1; we recall that non-covalent interaction energies are usually small when compared to chemical bond energies and total (molecular) electronic energies, and as such the differences are expected to be small.[56]

From the SAPT0 interaction energies, the brickwork TIPS-pentacene dimer is found to be more strongly bound with respect to pentacene in the herringbone configuration (-30 kcal/mol *vs*. -20 kcal/mol). However, a more apples-to-apples comparison is obtained by removing the TIPS moieties and looking at herringbone and brickwork pentacenes. The pentacene brickwork dimer is in fact less stable than the pentacene herringbone dimer by some 1.7 kcal/mol. While the changes to the electrostatic and induction terms essentially offset on going from the herringbone to the brickwork configuration, the increase in the dispersion term in the brickwork configuration is not able to compensate for the additional exchange repulsion that results from the larger overlap of the frontier π-orbitals. The considerable influence of the TIPS-functionality (other than the obvious steric bulk) arises from a large increase in the stabilizing dispersion interactions (by some 13-15 kcal/mol) as compared to either unsubstituted pentacene dimer.

Table 4.1. Dimer interaction energies, as determined by AMOEBA force-field calculations and SAPT0/jun-cc-pvdz calculations, and SAPT0 interaction energy components for pentacene herringbone, pentacene brickwork, and TIPS-pentacene. All energies in kcal/mol.

(kcal/mol)	*AMOEBA*	*SAPT Total Interaction Energy*	*Electrostatic*	*Dispersion*	*Induction*	*Exchange*
Pentacene Herringbone	-10.73	-19.81	-6.51	-26.28	-2.21	15.19
Pentacene Brickwork	-11.38	-18.14	-6.87	-28.07	-1.83	18.63
TIPS-Pentacene	-16.75	-29.16	-8.79	-41.49	-2.13	23.26

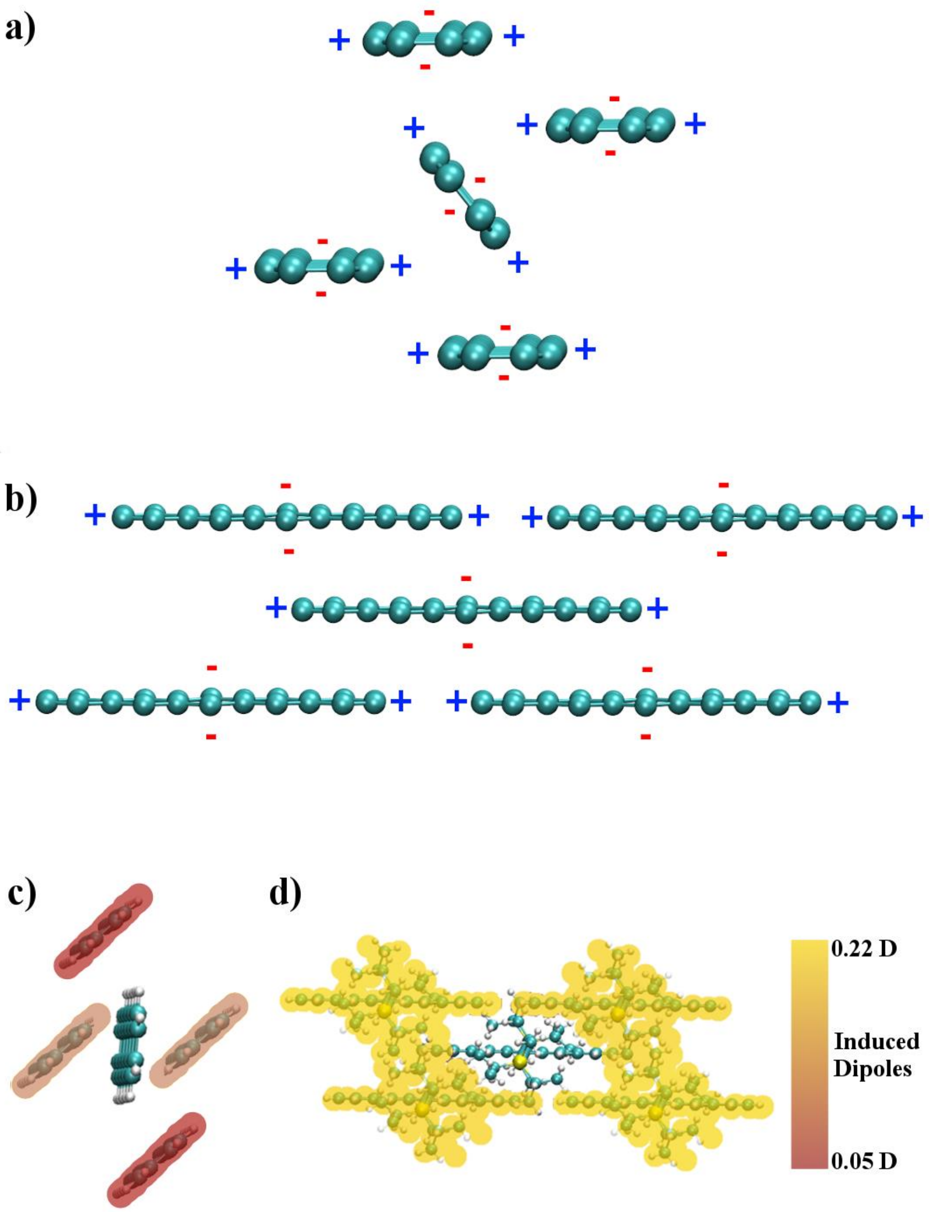

Figure 4.2. Illustration of the quadrupole interactions in herringbone (a) and brickwork (b) packed pentacene. Parts (c) and (d) display the induced dipoles on the nearest neighbors of a positively charged pentacene and TIPS-pentacene, respectively, determined with the parameterized AMOEBA force field. Dark red molecules in (c) have induced dipoles of 0.059 D, and those in light red have induced dipoles of 0.063 D. All nearest neighbors in (d) have induced dipoles of 0.214 D.

To scale to the system sizes (up to tens of thousands of atoms) required to study bulk polarization, currently relies on the use of classical-based models. Many classical models, though, fail to appropriately describe the intricacies of the intermolecular interactions in sandwich and brickwork structures, often describing the electrostatic interaction as exclusively repulsive.[57] For example, a commonly used methodology for the classical description of electrostatic interactions, the distributed multipole analysis (DMA) method,[58] fails to correctly describe the pentacene structures of interest here: Taking the same series of dimer structures, the DMA results suggest that the pentacene herringbone dimer is the only stable configuration (-1.27 kcal/mol), while the brickwork pentacene (+1.62 kcal/mol) and TIPS-pentacene (+0.95 kcal/mol) dimers are repulsive. While these total interaction energies are clearly incorrect, the individual terms arising from the DMA method (Table 4.2) reveal an interesting trend, namely that the quadrupole-quadrupole interactions are stabilizing in herringbone pentacene and destabilizing in the brickwork structures; the quadrupole-quadrupole interactions of these configurations, using the signs of the quadrupole moments derived at the MP2/6-31+G(d,p) level, are depicted qualitatively in Figure 4.2.

Table 4.2. DMA quadrupole-quadrupole electrostatic interaction energies for dimers of pentacene and TIPS-pentacene. DMA data calculated at the HF/6-311G(d,p) level. All units in kcal/mol.

(kcal/mol)	*Quadrupole-Quadrupole Interaction Energy*
Pentacene Herringbone	-0.0514
Pentacene Brickwork	0.1031
TIPS-Pentacene	0.2567

The AMOEBA force field significantly extends beyond simple DMA by not just including point multipoles (up to quadrupoles) at each atomic site, but also by incorporating polarization and van der Waals interactions.[47] Hence, the interaction energies derived from the AMOEBA-based analysis of the dimers are all stable, see Table 4.1, and are about half the values obtained at the SAPT0 level. The TIPS-pentacene dimer is the most stable in both models; in contrast to SAPT0, AMOEBA predicts that brickwork pentacene is slightly more stable than the herringbone configuration, a result that arises from stronger van der Waals interactions in the brickwork configuration. Given that the evaluation of the bulk polarization energies mainly deals with longer-range interactions (as opposed to the influence of exclusively short-range interactions such as charge penetration) and that we consider only the herringbone pentacene and brickwork TIPS-pentacene configurations whose interaction energies AMOEBA qualitatively describes well, our AMOEBA-based methodology is expected to provide a correct description of the polarization energies.[59]

Figure 4.2(c-d) also illustrates the magnitudes of the dipole moments induced by the presence of a positive charge on the central molecule of five-molecule clusters. For pentacene, there is a very slight asymmetry in the induced dipole moments (0.063 Debye *vs*. 0.059 Debye) in the herringbone packing configuration. Importantly, the induced dipole moments are much larger in TIPS-pentacene (0.21 Debye for all neighbors, with no asymmetry observed). These differences point to another key dissimilarity as a function of molecular packing and indicate that induced dipole moments will be of considerable importance in the stabilization of charge carriers in the brickwork-packed TIPS-pentacene.

In view of the above discussion, it can be anticipated that quadrupole and induced-dipole effects will strongly impact the bulk electronic polarizations. Charge−permanent-quadrupole interactions in the systems here (we recall that these molecules possess no permanent dipole moment) are expected to have considerable contribution to the magnitude and asymmetry (due to differences in the sign of the charge) of the electronic polarization; on the other hand, the induced-dipole interactions are expected to act to reduce the asymmetry as they form so as to stabilize the charge and, depending on the local quadrupoles, will result in varying degrees of stabilization.

4.3.3 Polarization in Pentacene and TIPS-Pentacene Bulk Systems

We now expand the system sizes under consideration through a range of clusters that can include upwards of many thousands of atoms by relying on our recently described approach to evaluate the bulk electronic polarizations.[59] The results presented in Figure 4.3 show that the bulk polarization energy for positive charges (holes) is some 0.4 eV larger in pentacene (1.02 eV) than in TIPS-pentacene (0.59 eV), which is in good general agreement with the experimental results reported by Kahn and co-workers.[23-26] The polarization energies for negative charges (electrons) are 0.79 eV in pentacene (~0.2 eV *smaller* than for holes) and 0.69 eV in TIPS-pentacene (~0.1 eV *larger* than for holes). In pentacene, experimental data confirm that the electronic polarization energy for a hole is larger than for an electron; the same holds true for the other unsubstituted acenes.[60-63]

That there is a difference as to which charge carrier leads to the larger polarization energy in TIPS-pentacene *vs*. pentacene is an interesting consequence of the molecular packing configurations. If we first examine the contributions to the polarization energy arising solely from the permanent multipole moments (*i.e*., monopole-quadrupole and quadrupole-quadrupole interactions), we obtain that: (i) TIPS-pentacene has a larger polarization energy asymmetry than pentacene (0.67 eV *vs*. 0.45 eV for the largest clusters, respectively); and (ii) both systems have larger polarization energies for holes than for electrons. This picture changes dramatically when the induced dipoles are included: (i) the polarization energy asymmetries markedly decrease, with that for TIPS-pentacene (0.10 eV) now being smaller than in pentacene (0.23 eV); and (ii) the electron in TIPS-pentacene becomes the charge carrier with the larger polarization energy. Hence, the interplay between the molecular packing structures and the permanent multipole and induced-dipole moments plays a defining role in determining the polarizations in these materials.

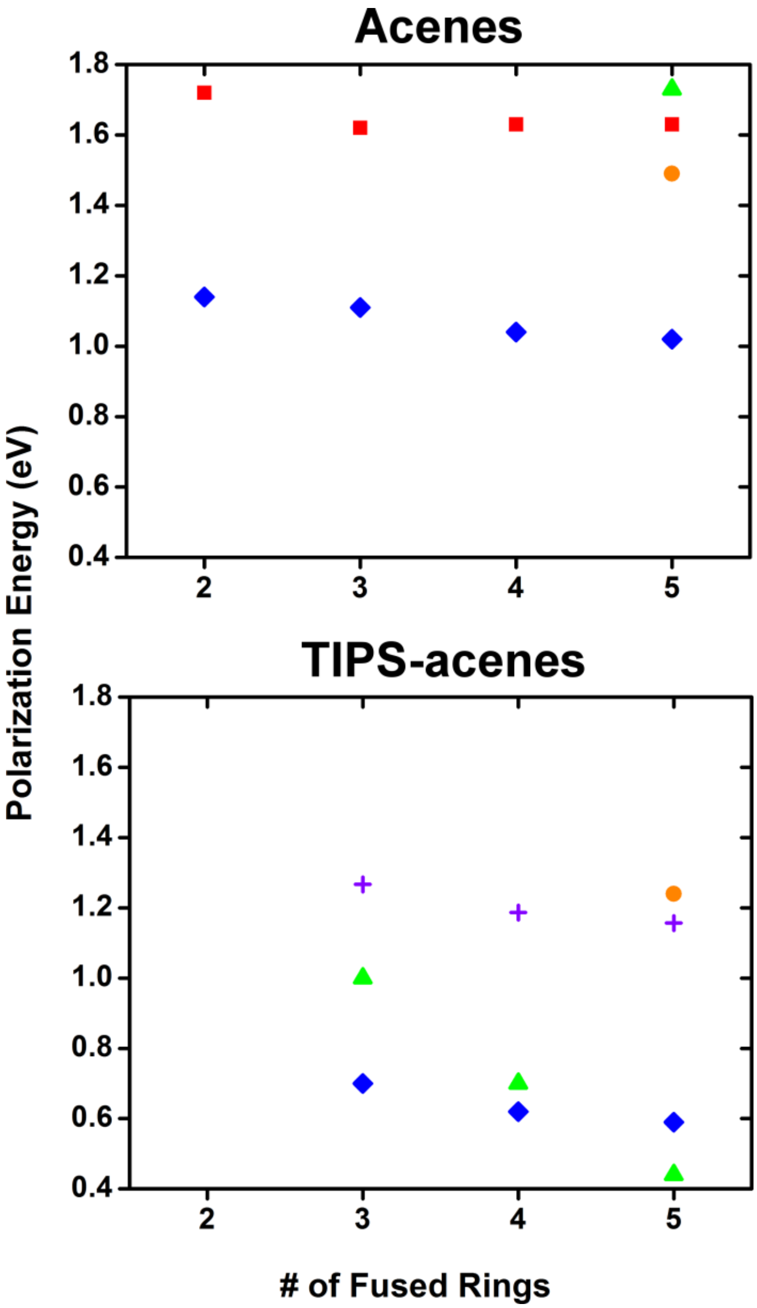

Figure 4.3. Bulk polarization energies due to a hole for oligoacenes (top) and TIPS-substituted acenes (bottom) as calculated with our model (♦) or reported from experimental measurements by Sato *et al.* (■),[60] Griffith *et al.* (▲),[23] and Qi *et al.* (●).[26] We also show (+) the calculated values for the TIPS-substituted acenes correct by the average difference between the calculated and experimental values for the oligoacenes.

With regard to the polarization energy due to a positive charge carrier as a function of the oligoacene length, there occurs a modest decrease in the polarization energy for the unsubstituted oligoacenes as the molecular backbone expands, with the calculated evolution (0.12 eV decrease from 1.14 eV for naphthalene to 1.02 eV for pentacene)[66] being in excellent agreement with the experimental data of Sato *et al*. (0.09 eV decrease from 1.72 eV for naphthalene to 1.63 eV for pentacene).[28] (The differences between theory and experiment in terms of the absolute values of the P_+ energies have been discussed in Chapter 3). Overall, the decrease of P_+ as a function of increased acene length can be related to the expanded distribution of the hole across the molecule that reduces the size of the charge-quadrupole interactions. Note that as the acene length increases, the charge carrier (hole or electron) becomes more distributed along the molecule. This results in a decrease of the magnitude of the atomic charge at each atom site. In addition, the molecular quadrupole moments increase with acene length, with the atomic-centered quadrupole moments maintaining a consistent value across the series. The combination of these effects leads to overall smaller monopole-quadrupole interactions as a function of increased acene length.

For the TIPS-acenes, we calculate a similar decrease (0.11 eV from 0.70 eV for TIPS-anthracene to 0.59 eV for TIPS-pentacene). The evolution measured by Lichtenberger and co-workers in the TIPS-substituted acenes is quantitatively much larger: P_+ for TIPS-anthracene (1.00 eV) is measured by these authors to be some 0.5 eV larger than P_+ for TIPS-pentacene (0.44 eV).[23,25] However, our calculated difference between the P_+ energies of pentacene and TIPS-pentacene, 0.43 eV, is much closer to the value measured by Kahn and co-workers, 0.25 eV, than that measured by Lichtenberger and co-workers, 1.29 eV.

In fact, if we correct the calculated value of P_+ for TIPS-pentacene by the average difference in calculated *vs*. experimental P_+ values for the oligoacenes, we obtain an estimated value for the TIPS-pentacene P_+ within 0.1 eV of the P_+ value measured by Kahn and co-workers, see bottom of Figure 4.3. The better agreement between our results based on the crystal structure of TIPS-pentacene and the data from Kahn and co-workers measured on ordered thin films *vs*. the data from Lichtenberger and co-workers obtained on more disordered films underlines the importance of morphology and local packing configurations in determining polarization energies.

4.4 Conclusions

We have presented a combined quantum mechanics / molecular mechanics description of the polarization energies for holes and electrons in the unsubstituted and TIPS-substituted acene series. Through a multiscale theoretical approach, we have developed a picture founded in basic electrostatics that explains the origin of the markedly different polarization energies in the two types of systems. Use of a polarizable force-field that includes quadrupole and induced-dipole interactions has allowed us to depict how electrostatic interactions change on going from the (oligoacene) herringbone motif to the (TIPS-substituted acene) brickwork packing structure. Though these systems show very similar electronic and electrostatic characteristics for the isolated molecules, the variations in solid-state packing induce very different electronic polarization effects, *e.g*., the Coulombically favorable intermolecular quadrupole interactions in the pentacene herringbone motif are not accessible to TIPS-pentacene due to variations in molecular packing caused by the presence of the bulky TIPS groups.

These results help clarify previous experimental findings[23-25] by providing an in-depth picture of the electrostatic interactions that result in the shift of the ionization energies on going from the gas phase to the solid state, and offer general insight into the bulk polarization energy in these materials. The brickwork configuration of TIPS-pentacene leads to a fundamental change in the quadrupole and induced-dipole interactions, resulting in smaller bulk polarization energy compared to pentacene.

The main message of this work is that the impact of molecular packing configurations, well established in the case of the charge-carrier transport and optical properties,[23-25,59,64-67] also extends to the polarization properties of π-conjugated materials. The work also underlines that extreme care has to be taken when extrapolating solution electrochemical data (a long time-scale thermodynamic equilibrium measure that includes entropy) for oxidation and reduction potentials to solid-state ionization energies and electron affinities (spectroscopic-based, short-time scale measurements).

4.5 References

(1) Zschieschang, U.; Kang, M. J.; Takimiya, K.; Sekitani, T.; Someya, T.; Canzler, T. W.; Werner, A.; Blochwitz-Nimoth, J.; Klauk, H. *J. Mater. Chem.* **2012**, *22*, 4273.
(2) Ou-Yang, W.; Uemura, T.; Miyake, K.; Onish, S.; Kato, T.; Katayama, M.; Kang, M.; Takimiya, K.; Ikeda, M.; Kuwabara, H.; Hamada, M.; Takeya, J. *Appl. Phys. Lett.* **2012**, *101*, 223304.
(3) Valeev, E. F.; Coropceanu, V.; Filho, D. A. d. S.; Salman, S.; Bredas, J. L. *J. Am. Chem. Soc.* **2006**, *128*, 9882.
(4) Coropceanu, V.; Cornil, J.; Silva, D. A. d.; Olivier, Y.; Silbey, R.; Bredas, J. L. *Chem. Rev.* **2007**, *107*, 926.
(5) Bakulin, A. A.; Rao, A.; Pavelyev, V. G.; van Loosdrecht, P. H. M.; Pshenichnikov, M. S.; Niedzialek, D.; Cornil, J.; Beljonne, D.; Friend, R. H. *Science* **2012**, *335*, 1340.
(6) Ahn, T.-S.; Muller, A. M.; Al-Kaysi, R. O.; Spano, F. C.; Norton, J. E.; Beljonne, D.; Bredas, J.-L.; Bardeen, C. J. *J. Chem. Phys.* **2008**, *128*, 054505.
(7) Saigusa, H.; Lim, E. C. *J. Phys. Chem.* **1994**, *98*, 13470.
(8) Sai, N.; Barbara, P. F.; Leung, K. *Phys. Rev. Lett.* **2011**, *106*, 226403.
(9) van Dijk, L.; Spano, F. C.; Bobbert, P. A. *Chem. Phys. Lett.* **2012**, *529*, 69.
(10) Müller, A. M.; Avlasevich, Y. S.; Schoeller, W. W.; Müllen, K.; Bardeen, C. J. *J. Am. Chem. Soc.* **2007**, *129*, 14240.
(11) Wilson, M. W. B.; Rao, A.; Clark, J.; Kumar, R. S. S.; Brida, D.; Cerullo, G.; Friend, R. H. *J. Am. Chem. Soc.* **2011**, *133*, 11830.
(12) Jadhav, P. J.; Brown, P. R.; Thompson, N.; Wunsch, B.; Mohanty, A.; Yost, S. R.; Hontz, E.; Van Voorhis, T.; Bawendi, M. G.; Bulović, V.; Baldo, M. A. *Adv. Mater.* **2012**, *24*, 6169.
(13) Roberts, S. T.; McAnally, R. E.; Mastron, J. N.; Webber, D. H.; Whited, M. T.; Brutchey, R. L.; Thompson, M. E.; Bradforth, S. E. *J. Am. Chem. Soc.* **2012**, *134*, 6388.
(14) Smith, M. B.; Michl, J. *Chem. Rev.* **2010**, *110*, 6891.
(15) Hohenstein, E. G.; Duan, J.; Sherrill, C. D. *J. Am. Chem. Soc.* **2011**, *133*, 13244.
(16) Silinsh, E. A. *Organic Molecular Crystals: Their Electronic States*; Springer: New York, 1980.
(17) Sherrill, C. D. *Acc. Chem. Res.* **2013**, *46*, 1020.
(18) Neumann, M. A.; Leusen, F. J. J.; Kendrick, J. *Angew. Chem., Int. Ed.* **2008**, *47*, 2427.
(19) Neumann, M. A. *J. Phys. Chem. B* **2008**, *112*, 9810.
(20) Sanderson, K. *Nature* **2007**, *450*, 771.
(21) Price, S. L.; Leslie, M.; Welch, G. W. A.; Habgood, M.; Price, L. S.; Karamertzanis, P. G.; Day, G. M. *Phys. Chem. Chem. Phys.* **2010**, *12*, 8478.
(22) Zhou, H.; Skolnick, J. *Biophys. J.* **2011**, *101*, 2043.
(23) Griffith, O. L.; Jones, A. G.; Anthony, J. E.; Lichtenberger, D. L. *J. Phys. Chem. C* **2010**, *114*, 13838.
(24) Griffith, O. L.; Anthony, J. E.; Jones, A. G.; Shu, Y.; Lichtenberger, D. L. *J. Am. Chem. Soc.* **2012**, *134*, 14185.
(25) Griffith, O. L.; Anthony, J. E.; Jones, A. G.; Lichtenberger, D. L. *J. Am. Chem. Soc.* **2010**, *132*, 580.

(26) Qi, Y.; Mohapatra, S. K.; Kim, S. B.; Barlow, S.; Marder, S. R.; Kahn, A. *Appl. Phys. Lett.* **2012**, *100*, 083305.
(27) Chan, C.; Kahn, A. *Appl. Phys. A* **2009**, *95*, 7.
(28) Anthony, J. E.; Swartz, C. R.; Landis, C. A.; Parkin, S. R. *Proc. SPIE* **2005**, *5940*, 594002.
(29) Bredas, J.-L. *Mater. Horiz.* **2014**, *1*, 17.
(30) Brooks, J. S.; Eaton, D. L.; Parkin, S. R.; Anthony, J. E. *J. Am. Chem. Soc.* **2001**, *123*, 9482.
(31) Chen, J.; Subramanian, S.; Parkin, S. R.; Siegler, M.; Gallup, K.; Haughn, C.; Martin, D. C.; Anthony, J. E. *J. Mater. Chem.* **2008**, *18*, 1961.
(32) Chen, J.; Anthony, J.; Martin, D. C. *J. Phys. Chem. B* **2006**, *110*, 16397.
(33) Ryno, S. M.; Risko, C.; Brédas, J.-L. *J. Am. Chem. Soc.* **2014**, *136*, 6421.
(34) Brock, C. P.; Dunitz, J. D. *Acta Crystallogr., Sect. B* **1990**, *B46*, 795.
(35) Holmes, D.; Kumaraswamy, S.; Matzger, A. J.; Vollhardt, K. P. C. *Chem.−Eur. J.* **1999**, *5*, 3399.
(36) Mattheus, C. C.; Dros, A. B.; Baas, J.; Meetsma, A.; Boer, J. L. d.; Palstra, T. T. M. *Acta Crystallogr., Sect. C: Cryst. Struct. Commun.* **2001**, *57*, 939.
(37) Frisch, M. J.; Trucks, G. W.; Schlegel, H. B.; Scuseria, G. E.; Robb, M. A.; Cheeseman, J. R.; Scalmani, G.; Barone, V.; Mennucci, B.; Petersson, G. A.; Nakatsuji, H.; Caricato, M.; Li, X.; Hratchian, H. P.; Izmaylov, A. F.; Bloino, J.; Zheng, G.; Sonnenberg, J. L.; Hada, M.; Ehara, M.; Toyota, K.; Fukuda, R.; Hasegawa, J.; Ishida, M.; Nakajima, T.; Honda, Y.; Kitao, O.; Nakai, H.; Vreven, T.; Montgomery Jr., J. A.; Peralta, J. E.; Ogliaro, F.; Bearpark, M. J.; Heyd, J.; Brothers, E. N.; Kudin, K. N.; Staroverov, V. N.; Kobayashi, R.; Normand, J.; Raghavachari, K.; Rendell, A. P.; Burant, J. C.; Iyengar, S. S.; Tomasi, J.; Cossi, M.; Rega, N.; Millam, N. J.; Klene, M.; Knox, J. E.; Cross, J. B.; Bakken, V.; Adamo, C.; Jaramillo, J.; Gomperts, R.; Stratmann, R. E.; Yazyev, O.; Austin, A. J.; Cammi, R.; Pomelli, C.; Ochterski, J. W.; Martin, R. L.; Morokuma, K.; Zakrzewski, V. G.; Voth, G. A.; Salvador, P.; Dannenberg, J. J.; Dapprich, S.; Daniels, A. D.; Farkas, Ö.; Foresman, J. B.; Ortiz, J. V.; Cioslowski, J.; Fox, D. J.; Gaussian, Inc.: Wallingford, CT, USA, 2009.
(38) Ridley, J.; Zerner, M. *Theor. Chim. Acta* **1973**, *32*, 111.
(39) Nishimoto, K.; Mataga, N. *Z. Phys. Chem. (Muenchen, Ger.)* **1957**, *12*, 335.
(40) Mataga, N.; Nishimoto, K. *Z. Phys. Chem. (Muenchen, Ger.)* **1957**, *13*, 140.
(41) Turney, J. M.; Simmonett, A. C.; Parrish, R. M.; Hohenstein, E. G.; Evangelista, F. A.; Fermann, J. T.; Mintz, B. J.; Burns, L. A.; Wilke, J. J.; Abrams, M. L.; Russ, N. J.; Leininger, M. L.; Janssen, C. L.; Seidl, E. T.; Allen, W. D.; Schaefer, H. F.; King, R. A.; Valeev, E. F.; Sherrill, C. D.; Crawford, T. D. *WIREs Comput. Mol. Sci.* **2012**, *2*, 556.
(42) Werner, H.-J.; Knowles, P. J.; Knizia, G.; Manby, F. R.; Schütz, M.; Celani, P.; Korona, T.; Lindh, R.; Mitrushenkov, A.; Rauhut, G.; Shamasundar, K. R.; Adler, T. B.; Amos, R. D.; Bernhardsson, A.; Berning, A.; Cooper, D. L.; Deegan, M. J. O.; Dobbyn, A. J.; Eckert, F.; Goll, E.; Hampel, C.; Hesselmann, A.; Hetzer, G.; Hrenar, T.; Jansen, G.; Köppl, C.; Liu, Y.; Lloyd, A. W.; Mata, R. A.; May, A. J.; McNicholas, S. J.; Meyer, W.; Mura, M. E.; Nicklass, A.; O'Neill, D. P.; Palmieri, P.; Peng, D.; Pflüger, K.; Pitzer, R.; Reiher, M.; Shiozaki, T.; Stoll, H.; Stone, A. J.; Tarroni, R.; Thorsteinsson, T.; Wang, M. MOLPRO, version 2012.1, a package of ab initio programs. Published Online: 2012.
(43) Stone, A. J. *The Theory of Intermolecular Forces*; Clarendon Press: Oxford, 1996.

(44) Ponder, J. W. *TINKER: Software Tools for Molecular Design*, 2012.
(45) Ren, P.; Ponder, J. W. *J. Comput. Chem.* **2002**, *23*, 1497.
(46) Ren, P.; Ponder, J. W. *J. Phys. Chem. B* **2003**, *107*, 5933.
(47) Ponder, J. W.; Wu, C.; Ren, P.; Pande, V. S.; Chodera, J. D.; Schnieders, M. J.; Haque, I.; Mobley, D. L.; Lambrecht, D. S.; DiStasio, R. A.; Head-Gordon, M.; Clark, G. N. I.; Johnson, M. E.; Head-Gordon, T. *J. Phys. Chem. B* **2010**, *114*, 2549.
(48) Sinnokrot, M. O.; Sherrill, C. D. *J. Phys. Chem. A* **2006**, *110*, 10656.
(49) Ringer, A. L.; Sherrill, C. D. *J. Am. Chem. Soc.* **2009**, *131*, 4574.
(50) Hohenstein, E. G.; Sherrill, C. D. *J. Chem. Phys.* **2010**, *132*, 184111.
(51) Jaeger, H. M.; Schaefer, H. F.; Hohenstein, E. G.; David Sherrill, C. *Comp. Theor. Chem.* **2011**, *973*, 47.
(52) Seo, J.-I.; Kim, I.; Lee, Y. S. *Chem. Phys. Lett.* **2009**, *474*, 101.
(53) Lutz, P. B.; Bayse, C. A. *Phys. Chem. Chem. Phys.* **2013**, *15*, 9397.
(54) Ansorg, K.; Tafipolsky, M.; Engels, B. *J. Phys. Chem. B* **2013**, *117*, 10093.
(55) Podeszwa, R.; Bukowski, R.; Szalewicz, K. *J. Phys. Chem. A* **2006**, *110*, 10345.
(56) Szalewicz, K. *WIREs Comput. Mol. Sci.* **2012**, *2*, 254.
(57) Sherrill, C. D.; Takatani, T.; Hohenstein, E. G. *J. Phys. Chem. A* **2009**, *113*, 10146.
(58) Stone, A. J. *Chem. Phys. Lett.* **1981**, *83*, 233.
(59) Ryno, S. M.; Lee, S. R.; Sears, J.; Risko, C.; Bredas, J. L. *J. Phys. Chem. C* **2013**, *117*, 13853.
(60) Sato, N.; Inokuchi, H.; Silinsh, E. A. *Chem. Phys.* **1987**, *115*, 269.
(61) Ando, N.; Mitsui, M.; Nakajima, A. *J. Chem. Phys.* **2008**, *128*, 154318.
(62) Pope, M.; Burgos, J.; Giachino, J. *J. Chem. Phys.* **1965**, *43*, 3367.
(63) Berry, R. S.; Jortner, J.; Mackie, J. C.; Pysh, E. S.; Rice, S. A. *J. Chem. Phys.* **1965**, *42*, 1535.
(64) Beaujuge, P. M.; Tsao, H. N.; Hansen, M. R.; Amb, C. M.; Risko, C.; Subbiah, J.; Choudhury, K. R.; Mavrinskiy, A.; Pisula, W.; Brédas, J.-L.; So, F.; Müllen, K.; Reynolds, J. R. *J. Am. Chem. Soc.* **2012**, *134*, 8944.
(65) Pingel, P.; Zen, A.; Abellón, R. D.; Grozema, F. C.; Siebbeles, L. D. A.; Neher, D. *Adv. Funct. Mater.* **2010**, *20*, 2286.
(66) Noriega, R.; Rivnay, J.; Vandewal, K.; Koch, F. P. V.; Stingelin, N.; Smith, P.; Toney, M. F.; Salleo, A. *Nat. Mater.* **2013**, *12*, 1038.
(67) Clark, J.; Silva, C.; Friend, R. H.; Spano, F. C. *Phys. Rev. Lett.* **2007**, *98*, 206406.

CHAPTER 5

IMPACT OF MOLECULAR ORIENTATION AND PACKING DENSITY ON ELECTRONIC POLARIZATION IN THE BULK AND AT SURFACES

5.1 Introduction

In Chapter 4, we demonstrated that differences in the molecular packing of pentacene and TIPS-pentacene have a significant effect on the polarization energies of these electronically similar materials, resulting in a polarization energy difference of up to a few tenths of an eV.[1] As such, we have underlined that care must be taken when extrapolating data that neglect the effects of packing orientation, *e.g.*, the use of cyclic voltammetry data to predict the solid-state ionization energies (IE_{ss}). Considering rubrene and tetracene, two molecular systems that share a conjugated backbone and pack in a herringbone fashion (Figure 5.1), we now proceed to show that changing backbone orientation has a significant impact on the polarization energies of the two materials. To provide additional insight into materials design, we also explore the effect of changing the packing density on the polarization energy and observe a much stronger dependence on the packing in the *a*/*b*-plane, that is within the molecular layer (see Figures 5.1b and 5.1f), than along the *c*-axis, between molecular layers (Figures 5.1c and 5.1g). Along the *c*-axis, interlayer interactions are dominated by peripheral hydrogen contributions, while within the *a*/*b*-plane there are significant π-conjugated backbone interactions.

In addition to the effects of molecular orientation and packing density of the material, we evaluate as well differences between the polarization energy in the bulk versus at an organic-vacuum interface. In 1978, Salaneck measured a 0.3 eV reduction of the ionization energy for the surface of anthracene compared to the bulk material.[2] In recent years this result has garnered additional interest with experimental and theoretical reports arguing both in support of and against this change in polarization.[3-6] As the electronic polarization energy is essentially a combination of static multipole interactions and dynamic induced-dipole interactions, the theoretical debate simplifies to whether the reduced stabilization at the organic-vacuum interface by the dynamic contributions cancels out the increased stabilization by the static interactions. Using our model detailed in Chapter 3, we probe organic-vacuum interfaces to show that there is indeed a decrease in the polarization energy at the interface, although small, and decompose its static and dynamic contributions.[7] We also examine the polarization energy as a function of charge carrier depth at the interface to simulate an ultraviolet photoelectron spectroscopy (UPS) measurement, and highlight the impact of neighboring layers.

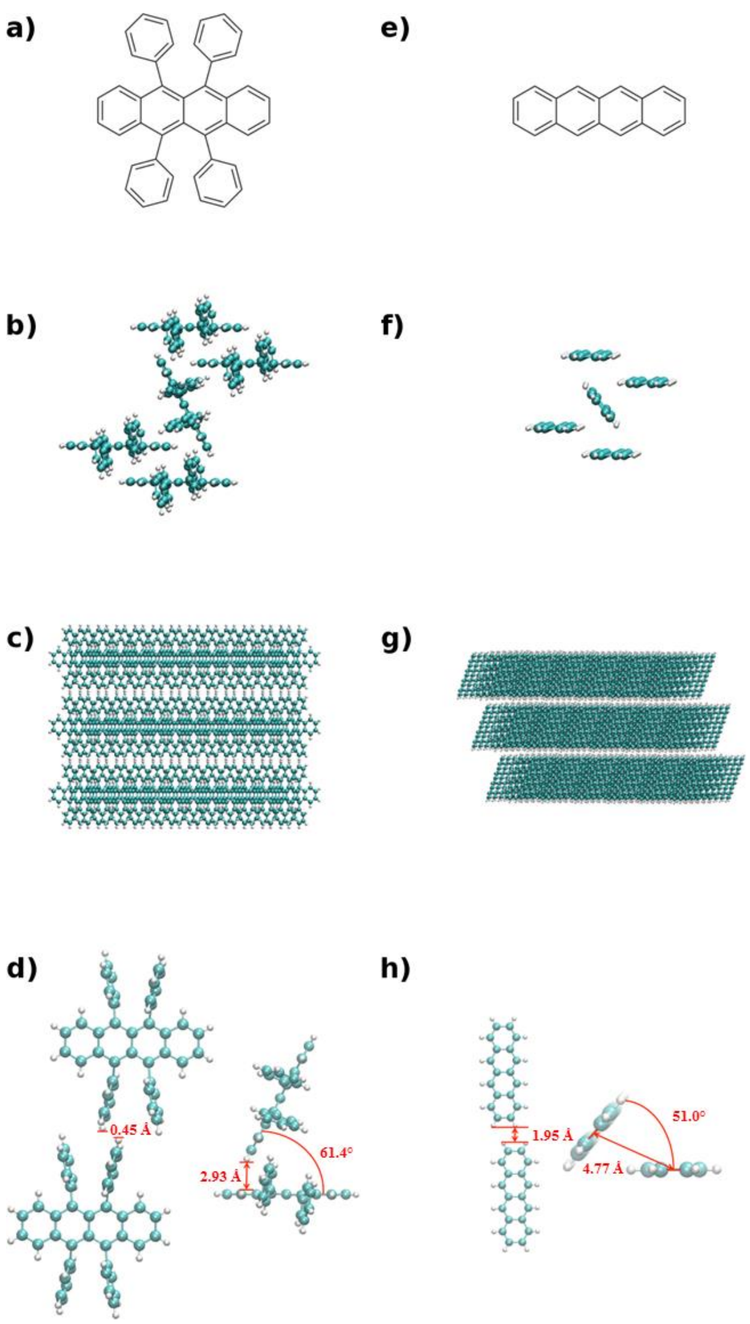

Figure 5.1. (a and e) Schematic representations of rubrene and tetracene, respectively. (b and f) *Intra*layer (*a*/*b*-plane) packing in rubrene and tetracene. Notice that both systems present herringbone packing, although rubrene displays significant backbone overlap. (c and g) *Inter*layer (*c*-axis) packing in rubrene and tetracene. (d and h) Intermolecular distances and angles between layers, and dimer separation and angles within the layers.

5.2 Computational Methodology

The geometries for all molecules used in this study were extracted from the reported crystal structures. Unmodified structures were taken from the tetracene (TETCEN01)[8] and rubrene (QQQCIG04) crystal structures deposited in the Cambridge Structural Database (CSD; CSD identification codes are noted within parentheses).[9,10]

Supercells, constructed from the experimental unit cells, were used to generate spherical clusters, cylinders, and slabs for the polarization studies. Modified unit cells were constructed from reported crystalline structures by increasing the unit-cell parameters while leaving the internal coordinates of the contained molecules unmoved, thus increasing the *inter*layer spacing, *intra*layer spacing, or both. Spherical clusters [cylinders] were constructed where molecules with their center-of-mass inside a given radius [and height] are selected from a larger supercell. Organic-vacuum interfaces were created by defining the origin of the system at the molecule in the center of the layer with the largest Z-axis value (*i.e*., the top-most layer of the supercell). A cylinder is then extracted in the same manner as above, but where half of the cylinder is composed of vacuum. The molecule whose charge is varied in the polarization energy calculations is defined as the origin in all extracted systems.

All calculations of bulk polarization energy were carried out with our previously described method[7] using the AMOEBA force field of Ponder and co-workers.[11,12] All electrostatic parameters were derived from distributed multipole analysis (DMA) using the single-particle density matrices from the neutral, radical-cation, and radical-anion states determined from single-point energy calculations using second-order Møller-Plesset perturbation theory (MP2) and a 6-31+G(d,p) basis as implemented in the Gaussian 09 (revision A.02 and B.01) suite.[13,14]

For calculations of the charged states, the atom types for the molecule of interest were replaced with those derived for the radical-cation or radical-anion state. The polarization energies were then determined using the gas-phase and solid-state ionization energies (IE) and electron affinities (EA) according to the Lyons model (Equations 1.3a and 1.3b). The bulk polarization energies are determined by increasing the system size and plotting the polarization energy versus the cubic root of the number of molecules in the cluster. For cylindrical systems, the polarization energy is plotted versus the square root of the average number of molecules per layer to remove the height dependence of the systems.

5.3 Results and Discussion

5.3.1 Impact of Molecular Orientation

While the packing of rubrene and tetracene are both herringbone, there are some critical differences. As shown in Figure 5.1, tetracene displays edge-to-face packing, and rubrene displays both head-to-face and face-to-face interactions. The polarization energies of rubrene and tetracene have been reported to differ by some 0.5 eV, with Sato reporting a polarization energy for a positive charge carrier in rubrene to be 1.1 eV and that of tetracene to be 1.8 eV.[15] Note that in a later paper, which presented a re-evaluation of polarization energies reported by Sato, the polarization energy of tetracene was determined to be 1.6 eV, in agreement with Pope *et al*. and the theoretical results of Berry *et al*.;[16-18] no additional studies of the polarization energy of rubrene have been reported.

As a first step, we calculated the bulk polarization energies of tetracene and rubrene using our previously reported model. We find the polarization energy due to a positive charge in tetracene (1.04 eV) to be 0.28 eV larger than that of rubrene (0.76 eV). The polarization energies due to a negative charge are 0.92 eV and 0.65 eV for tetracene and rubrene, respectively.

From Figure 5.1, we see that both tetracene and rubrene present a herringbone packing motif, but the rotation of the backbone in rubrene results in a change in the electrostatic interactions thus impacting the polarization energy. As we showed in Chapter 4, the packing configuration of pentacene and TIPS-pentacene has a large impact on the polarization energy, where the change in electrostatic interactions, both static and dynamic, may act to either additionally stabilize or reduce the stabilization of an excess charge. Using DMA,[19] the quadrupolar electrostatic interactions in dimers of rubrene and tetracene were examined to determine the effect of changing the orientation of the molecular backbone and altering the herringbone packing. In tetracene, due to the stabilizing edge-to-face interaction, the quadrupole-quadrupole interaction is stabilizing by about 0.04 eV, while in rubrene, because of the dimer geometry being closer to that of an ideal T-shape, the quadrupole interactions are more than 2 times as stabilizing (0.10 eV). In rubrene there is an additional dimer configuration that must be considered due to the considerable overlap of neighboring π-conjugated backbones. In this configuration the quadrupole interactions are destabilizing by 0.26 eV, a value identical to that found in TIPS-pentacene.

To assess the impact of the changing electrostatic interactions, finite size clusters of 4 nm radius were considered. Since the induced dipoles are calculated independently from the static multipole interactions, the impact of these dynamic interactions can be separated from the static interactions simply by turning the induced dipoles off. In the absence of induced-dipole moments, with respect to the neutral systems, the static multipole interactions for a tetracene anion are stabilizing by 0.30 eV, while a rubrene anion is destabilized by 0.23 eV. For the cationic species, these static interactions are destabilizing be 1.16 eV and 1.49 eV for tetracene and rubrene, respectively. The large difference between the cation and the anion contributions results from the redistribution of charge that occurs between the charged and neutral systems. When the induced-dipole contributions are turned back on, each of the clusters is stabilized by greater than 0.5 eV and up to 1.1 eV. Since the polarization energy ($P_{\pm} = S_{\pm} + D_{\pm}$) is defined as the sum of the change in static ($S_{\pm}$) and dynamic contributions ($D_{\pm}$) with respect to the neutral system, this method of separating these effects allows for their individual contributions to be determined. For tetracene, the static contribution is stabilizing by 0.18 eV while the dynamic part is stabilizing by 0.74 eV for a positive charge carrier; for rubrene, the static and dynamic components are stabilizing by 0.15 eV and 0.50 eV, respectively. For both tetracene and rubrene, the dynamic contributions are some three times more stabilizing than the static contributions highlighting that the dynamic interactions dominate the polarization energy.

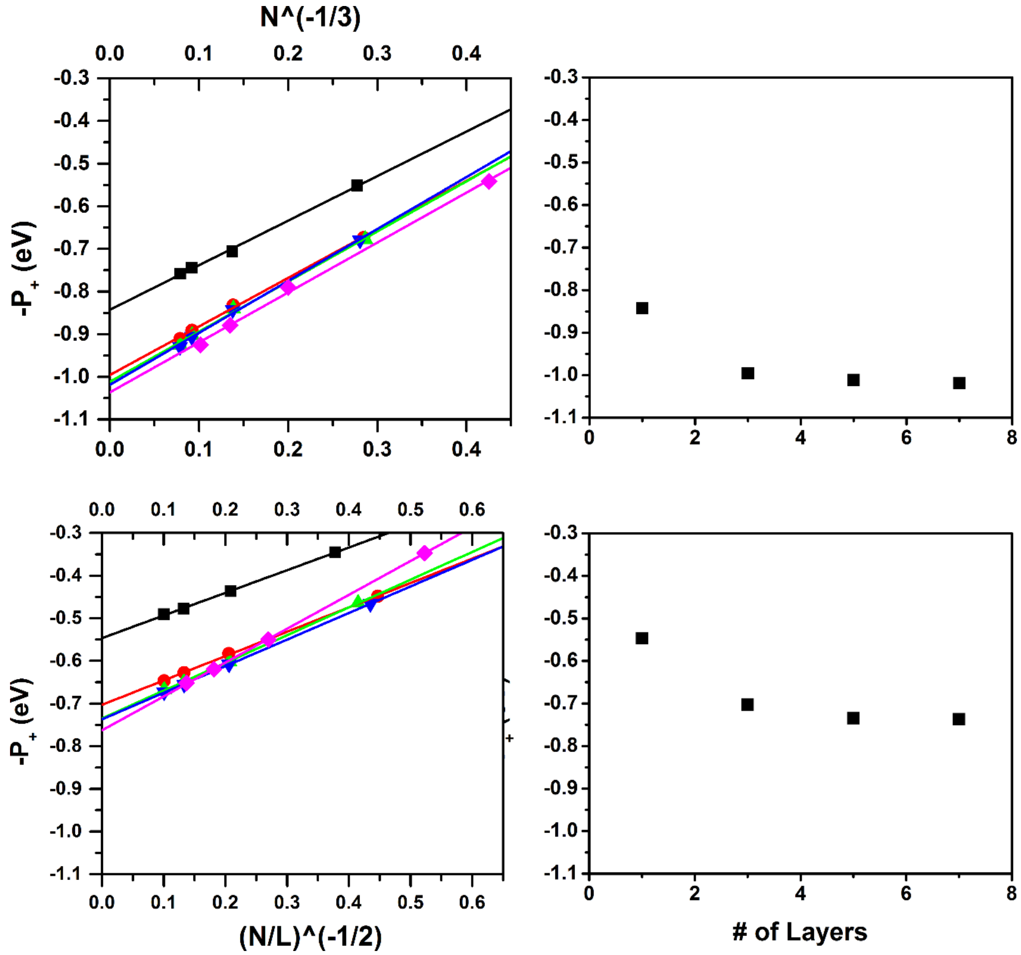

Figure 5.2. (Top left) Polarization energy as a function of the average number of molecules per layer for cylinders of tetracene consisting of 1 layer (black; ■), 3 layers (red; ●), 5 layers (green; ▲), and 7 layers (blue; ▼). The polarization energy for spherical clusters is provided for reference (magenta; ♦). (Top right) Extrapolated polarization energies for cylinders of tetracene as the number of layers is increased. Note there is little change in the polarization energy after the nearest-neighbor layer is added. (Bottom left) Polarization energy as a function of the average number of molecules per layer for cylinders of rubrene consisting of 1 layer, 3 layers, 5 layers, and 7 layers. The polarization energy of spherical clusters is provided for reference. (Bottom right) Extrapolated polarization energies for cylinders of rubrene as the number of layers is increased.

We further expanded the scope of our investigation by exploring cylindrical systems. While spherical clusters allow us to calculate the polarization energy of a material, cylindrical systems allow for the determination of the polarization energy as a function of the average number of molecules per layer, thus the impact of neighboring layers may be obtained. Since the cylindrical systems do not have the $\frac{1}{N^3}$ dependence of the spherical systems they are instead plotted versus $\frac{1}{(\frac{N}{L})^2}$, where N is the number of molecules in the system, and L is the number of layers in the cylinder. For these cylindrical systems, an initial disk (1 layer) is expanded by symmetrically increasing the number of layers on either side of the disk. Figure 5.2 shows the polarization energies for rubrene and tetracene cylinders consisting of 1, 3, 5, and 7 layers. As additional layers are added, the polarization energy per layer increases, but that increase quickly falls off after the nearest-neighbor layers are added. From Figure 5.2, it can be seen that the polarization energy for a single disk of tetracene is 0.84 eV, and increases by 0.16 eV when the nearest-neighbor layers are added. The polarization energy then only increases by an additional 0.02 eV for the next nearest-neighbor layers. The large impact of the nearest-neighbor layers highlights the importance of their inclusion in modeling the impact of the bulk on the properties of organic materials.

5.3.2 Bulk vs. Interfacial Polarization Energy

Since the seminal work of Salaneck, there has been continued debate as to whether the ionization energy, and in turn, the polarization energy at the surface of a material is different than that of the bulk.[2] This difference of environment will become important when discussing organic-vacuum field-effect transistors, where the charge moves along or near to the vacuum interface, and thus experiences an energetic landscape different than the bulk.[20] This change in energetic landscape will be present at organic-organic and organic-inorganic interfaces common in many organic electronic devices. Independent investigations by Tsiper[5] and Gorczak[6] reported that indeed the environment at the organic-vacuum interface is different than the bulk, but there is disagreement as to whether the change in the static and dynamic electrostatic interactions cancel each other out, as has been suggested by Gorczak.[6] While Gorczak reported equivalent polarization energies in the bulk and at the surface of pentacene, Tsiper reported a difference of 0.23 eV, with the surface being less stabilized.[5] Note that the treatment of Tsiper uses $\Delta P = P^S - P$, where $P = P_+ + P_-$, $P^S = P_+^S + P_-^S$. P and P^S are the combined polarization energies due to a positive charge and negative charge in the bulk and at the surface, respectively.

To better assess the environment at the organic-vacuum interface, hemispherical clusters were used, where the organic material on one side of the layer in which the excess charge resides has been removed. The polarization energy due to a positive charge carrier at both tetracene and rubrene surfaces was determined to be approximately 0.07 eV lower than their bulk values. Using the definition of Tsiper, we calculate ΔP to be 0.20 eV and 0.17 eV for tetracene and rubrene, respectively.

As stated earlier, both the static and dynamic interactions will change as a result of variation of the electrostatic environment. To assess the impact of the changing electrostatic interactions, the polarization energy contributions of finite sized clusters and hemispheres are examined (Table 5.1). Comparing the tetracene bulk to the interface, the static contribution to the polarization energy becomes more stabilizing by 0.06 eV while the dynamic contribution (induced-dipole interactions) becomes less stabilizing by 0.13 eV. For rubrene, the static contribution becomes more stabilizing by 0.02 eV and the dynamic contribution destabilizing by 0.09 eV. Both the increase in the static stabilization and decrease in dynamic stabilization result from a smaller number of neighboring molecules in the clusters, with the static interactions becoming more stabilizing because of fewer destabilizing charge-quadrupole interactions, while the dynamic interactions are destabilizing because of fewer polarizable points which always act to stabilize the charge. This is further illustrated when the molecules on both sides of the charged layer are removed, *i.e*., a 2D disk. For tetracene, the increased static contribution is almost doubled to 0.11 eV and the destabilization of the dynamic component increases to 0.26 eV. Similar changes in the static and dynamic contributions are observed for rubrene of 0.04 eV and 0.20 eV, respectively. Unsurprisingly, both sides of the bulk material adjacent to the charged layer contribute equally to the polarization energy with the fewer number of polarizable molecules having the largest impact. Since the static and induced moments of the adjacent layers interact, removing just one side of the layers will not be equivalent to one-half of the contribution from both layers.

Table 5.1. Polarization energies due to a radical-cation in rubrene and tetracene clusters, hemisphere organic-vacuum interfaces, and 2-dimensional disks. Static and dynamic interactions are the energy outputs from the AMEOBA force field for multipole interactions and polarization interactions for systems of 40 Å radius for their respective systems. All energies are reported in eV.

Tetracene/Rubrene (eV)	*Spherical Cluster*	*Hemispherical Interface*	*2D Disk*
P_+	1.04/0.76	0.89/0.63	0.84/0.55
Static Interactions	0.18/0.15	0.24/0.17	0.29/0.19
Dynamic Interactions	0.74/0.50	0.61/0.41	0.48/0.30

One may then expand beyond examining just the surface and the bulk, to simulate the probing of a surface by UPS where electrons are expected to be ejected from the first few layers.[21,22] To do this, cylindrical systems of constant thickness are created where a charge is initially placed at the topmost layer and subsequently moved to deeper layers. From Table 5.2, as the charge is moved from the surface of tetracene to the bulk, the static polarization energy decreases by about 17% and the dynamic contribution increases by about 19%. This results is an overall increase in the polarization energy by almost 10%. Because of the different electrostatic interactions in rubrene, the decrease of the static polarization energy is about 9% while the increase in the dynamic contribution is almost 21%. Thus, while the change in the dynamic polarization energy is similar for both systems, the different electrostatic interactions due to the variations in molecular packing have significant impact. Additionally, as the charge is moved from the interface layer to the adjacent layer, there is a large increase in the polarization energy in both tetracene and rubrene after which the change in only 1-2% as the charge moves into the bulk. As shown earlier, the layers neighboring the charge have the largest impact on the polarization energy. This indicates that for UPS measurements care must be taken to only probe the surface layer if the characteristics of the surface are desired, as the probing of any other layers are more representative of the bulk than of the surface.

Table 5.2. The polarization energy of cylindrical clusters of 7-layers as a radical-cation is moved from the top-most interfacial layer to the middle layer that is representative of the bulk material. Static, dynamic and static-plus-dynamic data represent finite sized cylinders of 4 nm radius while P_+ data are extrapolations. All energies are reported in eV.

Tetracene/Rubrene (eV)	*Static P_+*	*Dynamic P_+*	*S+D*	*P_+*
Layer 1 (interface)	0.23/0.16	0.64/0.44	0.87/0.59	0.93/0.66
Layer 2	0.20/0.15	0.73/0.51	0.94/0.66	1.01/0.73
Layer 3	0.19/0.15	0.75/0.52	0.94/0.67	1.01/0.74
Layer 4 (bulk)	0.19/0.15	0.76/0.53	0.95/0.67	1.02/0.74

These results clearly underline that the environment of an excess charge at the surface of an organic material is different than that of an excess charge in the bulk Furthermore, as shown by Beljonne and co-workers, the presence of a second organic system will introduce strong electrostatic interactions at the interface that further change the energetic landscape and impact the behavior of an excess charge or charges.[23]

5.3.3 Polarization Energy as a Function of Interlayer and Intralayer Packing Densities

Selective substitution of the phenyl rings of rubrene can allow for control of the molecular packing and thus control of the polarization energy.[24] This level of control will assist in the development of a roadmap to obtain desirable and interesting material morphologies for fundamental and applications studies. To provide a guide for future experimental efforts, we have investigated the effect of modifying the packing distances of rubrene and tetracene through expansion of the molecular crystal (Figure 5.3). First, we focus on expansions between layers, followed by expansion within molecular layers, and then as an extreme limit, combined expansion allowing for a better understanding of how the polarization energy and intermolecular interactions evolve as a function of separation distance along the unit-cell axes.

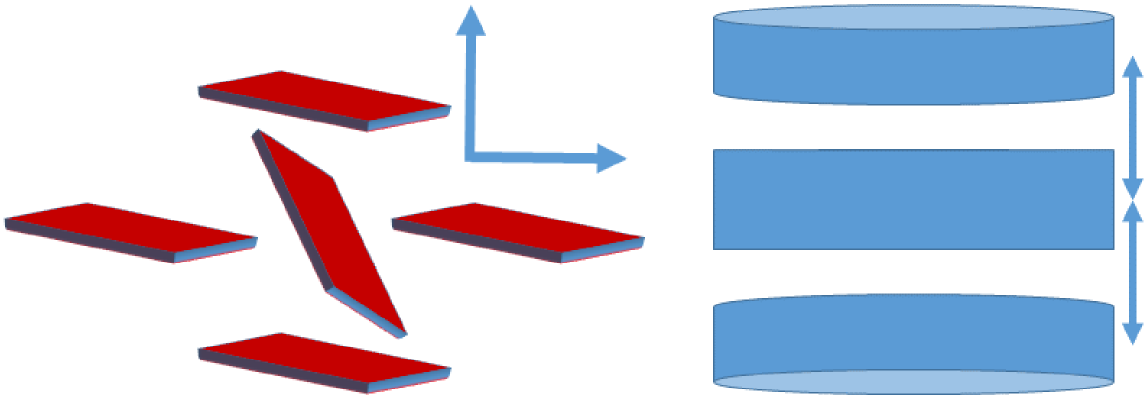

Figure 5.3. Block representation of the *intra*layer expansion (Left) within the *ab*-plane and *inter*layer expansion (Right) along the *c*-axis.

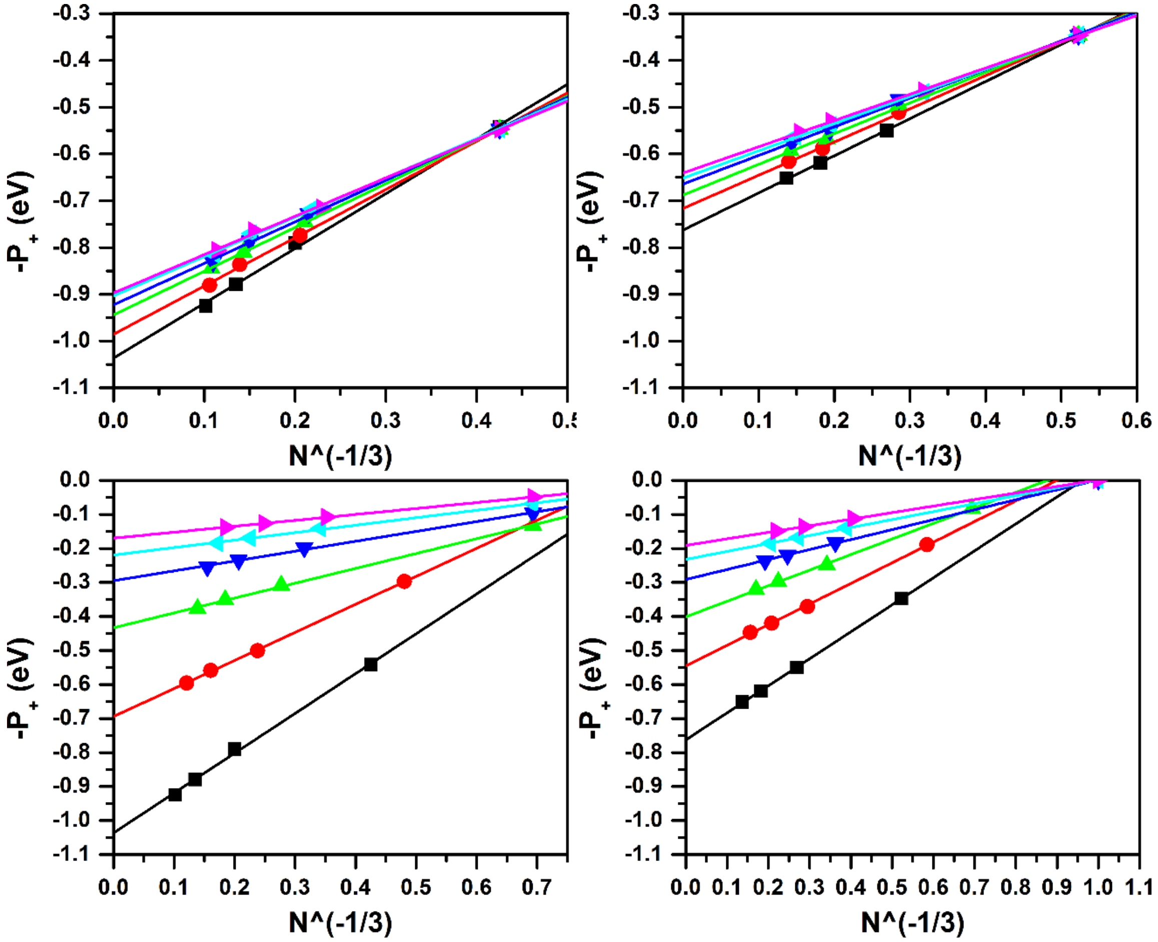

Figure 5.4. (Top) Extrapolated polarization energies of tetracene (left) and rubrene (Right) as the *inter*layer separation distance is increased from the crystalline value (black; ■) by an additional 1 Å (red; ●), 2 Å (green; ▲), 3 Å (dark blue; ▼), 4 Å (light blue; ◀), and 5 Å (magenta; ▶). (Bottom) Extrapolated polarization energies of tetracene (left) and rubrene (right) as the *intra*layer separation distance is increased from the crystalline value to an additional 5 Å.

As with intermolecular electronic couplings (*i.e.*, wavefunction overlap or transfer integrals), the interactions between linear oligoacenes in the crystals is weaker between layers than within layers.[25,26] In agreement with these previous assessments, changing the *inter*layer packing density results in a much smaller change than changing the *intra*layer packing density. From Figure 5.4, there is a decrease in the polarization energy of about 0.1 eV for both rubrene and tetracene as the distance between the layers is increased from that determined crystallographically to an extra 5 Å. As the separation increases to infinity the polarization energy approaches that of the $2D$-disk configurations (rubrene: 0.55 eV; tetracene: 0.84 eV). This limit is quickly approached as the charge-quadrupole interactions have a $\frac{1}{r^3}$ distance dependence and induced-dipole interactions have a stronger distance dependence, determined by the induction source.

The polarization energy is much more sensitive to the *intra*layer packing density, leading to a much diminished polarization energy as the density is reduced. For rubrene, the polarization energy diminishes by 0.57 eV as the distance between molecules is increased by 5 Å. The decrease in the polarization energy is even larger for tetracene, where the calculated decrease is 0.87 eV, a result of the larger dynamic component of the polarization energy and its strong distance dependence. For both systems, the polarization energy trends not toward zero, but approaches that of a 1D chain stacked along the *c*-axis of the unit cell. This is in agreement with what has been previously shown for intermolecular couplings where the *intra*layer packing has a larger impact compared to the *inter*layer packing; this is unsurprising when one considers the strength of the intermolecular interactions for face-to-edge interactions, that have many interacting points (present within layers), compared to edge-to-edge interactions (present between layers). We have in the previous Chapter shown using pentacene and TIPS-pentacene, that there is a change in the sign of these intermolecular interactions between face-to-edge (attractive) and face-to-face (repulsive), which may be considered analogous to the edge-to-edge interactions as the sign of the interacting quadrupoles are the same sign, i.e., like-sign interactions.

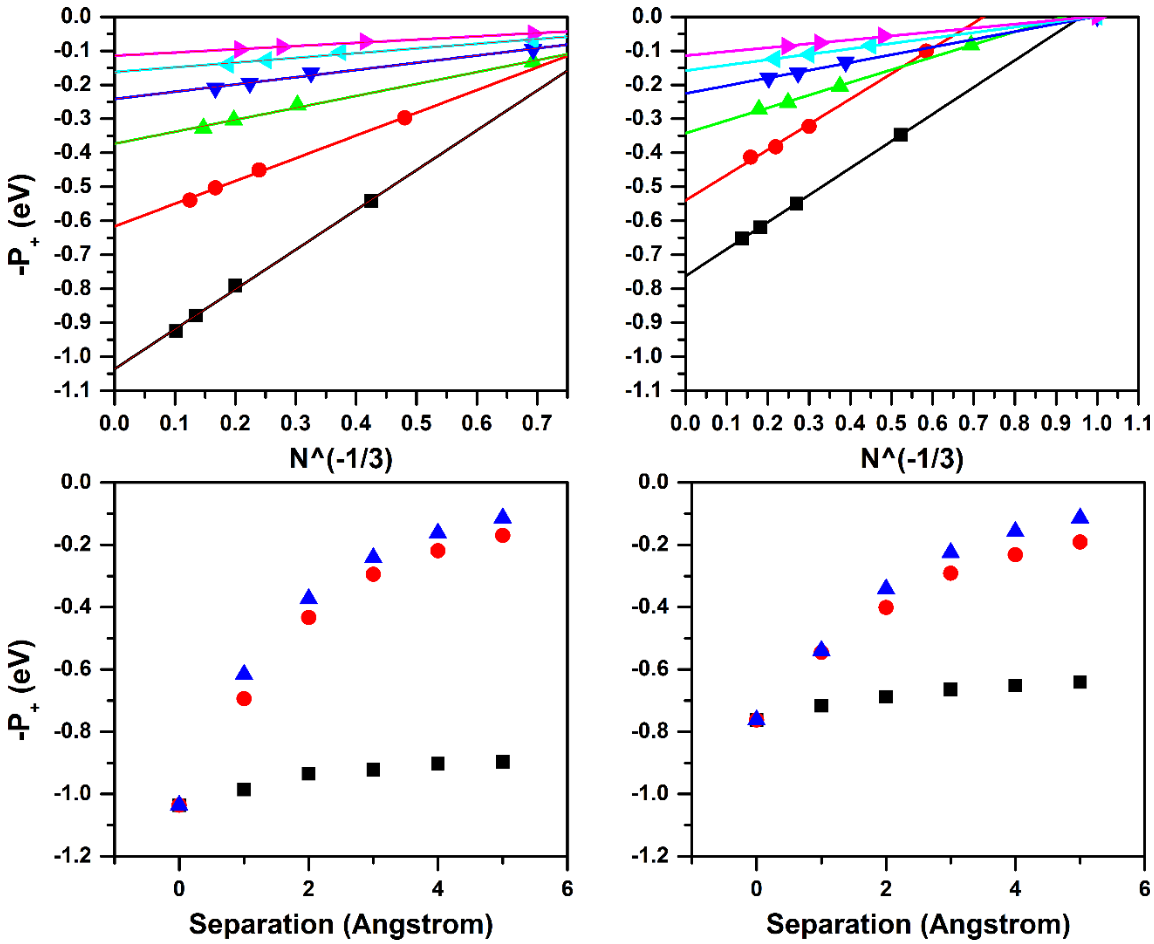

Figure 5.5. (Top) Extrapolated polarization energies of tetracene (left) and rubrene (right) as both the *inter*layer and intralayer separation distances are increased from the crystalline value (black; ■) by an additional 1 Å (red; ●), 2 Å (green; ▲), 3 Å (dark blue; ▼), 4 Å (light blue; ◀), and 5 Å (magenta; ▶). (Bottom) The combined polarization energies of tetracene (left) and rubrene (right) as a function of increased *inter*layer expansion (black; ■), *intra*layer expansion (red; ●), and combined symmetric expansion (blue; ▲).

Finally, we examined the extreme case of symmetric molecular expansion wherein both the *intra*layer and *inter*layer separations are concurrently increased at the same rate (Figure 5.5). In the range of expansions considered, we calculate a decrease of 0.92 eV for tetracene and 0.65 eV for rubrene. This expansion may be envisioned as beginning with a spherical cluster and then expanding the system to the point that it becomes a collection of non-interacting molecules. Hence, we observe that the polarization energy trends towards zero at the limit of infinite separation. It should be noted that if the unit cell contains asymmetric molecules, such as in the case of tetracene, then the same molecule must be used in both gas-phase and solid-state calculations. If the same molecule is not used, then there will be a remainder of polarization energy at the limit of infinite expansion equivalent to the site energy difference between the two molecules (about 0.02 eV for tetracene). As may be seen from the above, *intra*layer expansion has the most significant impact on the polarization energy, wherein small decreases in the packing density result in large reductions of the polarization energy. By possessing a fuller understanding of how molecular packing impacts material properties, *e.g.*, polarization energy, materials can be designed with desirable properties; thus, the work presented here in regards to *intra*layer and *inter*layer packing provide a general framework for which to base future experimental efforts to tune the polarization energy in organic molecular crystals.

5.4 Conclusions

Through the use of our model for polarization energy in organic molecular crystals, we developed a description of the impact of molecular orientation and packing density on the polarization energy, and provided an analysis of the change in the electrostatic interactions at an organic-vacuum interface to show how the energetic landscape changes as molecules are removed from layers adjacent to the layer in which a charge carrier resides. Similar to our prior investigation of pentacene and TIPS-pentacene, which allowed a comparison between herringbone and brickwork packing motifs,[1] we have investigated tetracene and rubrene, which both present herringbone packing, but where the backbones are rotated approximately 90° with respect to each other. Through the use of a distributed multipole analysis and decomposition of the static and dynamic components of the polarization energies of the respective systems, there is a qualitative change in the static multipole interactions even though both tetracene and rubrene present herringbone packing, but where the latter also displays face-to-face interactions, similar to TIPS-pentacene.[19]

Beyond simply investigating the polarization energies of the bulk material, we have also expanded the scope to examine organic-vacuum interfaces where, as a result of the reduced number of neighboring sites, the static component of the polarization energy becomes more stabilizing while the dynamic component becomes much less stabilizing. Although the overall change in the polarization energy because of the interface is relatively small compared to the total polarization energy, the change in the individual components is a much larger portion of the total. Finally, in continuing along the lines of modifying the environment of a charged molecule, we investigated the effect of reducing the packing density on the bulk polarization energy. Similar to previously reported results in the context of electronic couplings, we have shown that the *intra*layer molecular interactions have the largest effect on the polarization energy with a decrease of 0.92 eV for tetracene. Although the *inter*layer separation does impact the polarization energy of these systems, its effect is an order of magnitude lower than that of the *intra*layer packing.

Through these studies, we showed that although the tetracene and rubrene molecules are of similar structure and their electronic properties and crystalline packing are similar, small changes in the electrostatic interactions can result in large changes in the polarization energy. With this work we hope to have provided some general guidance for tuning the polarization energy of organic electronic materials through molecular orientation and packing density, and to provide insight into the electrostatic interactions at organic-vacuum interfaces that will assist with future device and materials engineering efforts through an increased understanding of the energetic landscape.

5.5 References

(1) Ryno, S. M.; Risko, C.; Brédas, J.-L. *J. Am. Chem. Soc.* **2014**, *136*, 6421.

(2) Salaneck, W. *Phys. Rev. Lett.* **1978**, *40*, 60.

(3) Casu, M. B.; Zou, Y.; Kera, S.; Batchelor, D.; Schmidt, T.; Umbach, U. *Phys. Rev. B* **2007**, *76*, 193311.

(4) Yoshida, H.; Sato, N. *J. Phys. Chem. C* **2012**, *116*, 10033.

(5) Tsiper, E. V.; Soos, Z. G. *Phys. Rev. B* **2003**, *68*, 085301.

(6) Gorczak, N.; Swart, M.; Grozema, F. C. *J. Mater. Chem. C* **2014**, *2*, 3467.

(7) Ryno, S. M.; Lee, S. R.; Sears, J.; Risko, C.; Bredas, J. L. *J. Phys. Chem. C* **2013**, *117*, 13853.

(8) Holmes, D.; Kumaraswamy, S.; Matzger, A. J.; Vollhardt, K. P. C. *Chem. Eur. J.* **1999**, *5*, 3399.

(9) Allen, F. H. *Acta Crystallogr.* **2002**, *B58*, 380.

(10) Fletcher, D. A.; McMeeking, R. F.; Parkin, D. *J. Chem. Inf. Comput. Sci.* **1996**, *36*, 746.

(11) Ren, P.; Ponder, J. W. *J. Phys. Chem. B* **2003**, *107*, 5933.

(12) Ponder, J. W.; Wu, C.; Ren, P.; Pande, V. S.; Chodera, J. D.; Schnieders, M. J.; Haque, I.; Mobley, D. L.; Lambrecht, D. S.; DiStasio, R. A.; Head-Gordon, M.; Clark, G. N. I.; Johnson, M. E.; Head-Gordon, T. *J. Phys. Chem. B* **2010**, *114*, 2549.

(13) Stone, A. J. *Chem. Phys. Lett.* **1981**, *83*, 233.

(14) Frisch, M. J.; Trucks, G. W.; Schlegel, H. B.; Scuseria, G. E.; Robb, M. A.; Cheeseman, J. R.; Scalmani, G.; Barone, V.; Mennucci, B.; Petersson, G. A.; Nakatsuji, H.; Caricato, M.; Li, X.; Hratchian, H. P.; Izmaylov, A. F.; Bloino, J.; Zheng, G.; Sonnenberg, J. L.; Hada, M.; Ehara, M.; Toyota, K.; Fukuda, R.; Hasegawa, J.; Ishida, M.; Nakajima, T.; Honda, Y.; Kitao, O.; Nakai, H.; Vreven, T.; Montgomery, J. A.; Peralta, J. E.; Ogliaro, F.; Bearpark, M.; Heyd, J. J.; Brothers, E.; Kudin, K. N.; Staroverov, V. N.; Kobayashi, R.; Normand, J.; Raghavachari, K.; Rendell, A.; Burant, J. C.; Iyengar, S. S.; Tomasi, J.; Cossi, M.; Rega, N.; Millam, J. M.; Klene, M.; Knox, J. E.; Cross, J. B.; Bakken, V.; Adamo, C.; Jaramillo, J.; Gomperts, R.; Stratmann, R. E.; Yazyev, O.; Austin, A. J.; Cammi, R.; Pomelli, C.; Ochterski, J. W.; Martin, R. L.; Morokuma, K.; Zakrzewski, V. G.; Voth, G. A.; Salvador, P.; Dannenberg, J. J.; Dapprich, S.; Daniels, A. D.; Farkas; Foresman, J. B.; Ortiz, J. V.; Cioslowski, J.; Fox, D. J. Wallingford CT, 2009.

(15) Sato, N.; Seki, K.; Inokuchi, H. *J. Chem. Soc., Faraday Trans. 2* **1981**, *77*, 1621.

(16) Sato, N.; Inokuchi, H.; Silinsh, E. A. *Chem. Phys.* **1987**, *115*, 269.

(17) Berry, R. S.; Jortner, J.; Mackie, J. C.; Pysh, E. S.; Rice, S. A. *J. Chem. Phys.* **1965**, *42*, 1535.

(18) Pope, M.; Burgos, J.; Giachino, J. *J. Chem. Phys.* **1965**, *43*, 3367.

(19) Stone, A. J. *The Theory of Intermolecular Forces*; Clarendon Press: Oxford, 1996.

(20) Coropceanu, V.; Cornil, J.; Silva, D. A. d.; Olivier, Y.; Silbey, R.; Bredas, J. L. *Chem. Rev.* **2007**, *107*, 926.

(21) Seah, M. P.; Dench, W. A. *Surf. Interface Anal.* **1979**, *1*, 2.

(22) Tanuma, S.; Powell, C. J.; Penn, D. R. *Surf. Interface Anal.* **1994**, *21*, 165.

(23) Linares, M.; Beljonne, D.; Cornil, J. r. m.; Lancaster, K.; Brédas, J.-L.; Verlaak, S.; Mityashin, A.; Heremans, P.; Fuchs, A.; Lennartz, C.; Idé, J.; Méreau, R. l.; Aurel, P.; Ducasse, L.; Castet, F. d. r. *J. Phys. Chem. C* **2010**, *114*, 3215.
(24) McGarry, K. A.; Xie, W.; Sutton, C.; Risko, C.; Wu, Y.; Young, V. G.; Brédas, J.-L.; Frisbie, C. D.; Douglas, C. J. *Chem. Mater.* **2013**, *25*, 2254.
(25) Delgado, M. C. R.; Pigg, K. R.; da Silva Filho, D. A.; Gruhn, N. E.; Sakamoto, Y.; Suzuki, T.; Osuna, R. M.; Casado, J.; Hernández, V.; Navarrete, J. T. L.; Martinelli, N. G.; Cornil, J.; Sánchez-Carrera, R. S.; Coropceanu, V.; Brédas, J.-L. *J. Am. Chem. Soc.* **2009**, *131*, 1502.
(26) Salman, S.; Delgado, M. C. R.; Coropceanu, V.; Brédas, J.-L. *Chem. Mater.* **2009**, *21*, 3593.

CHAPTER 6

ENERGETIC LANDSCAPE AT ORGANIC–ORGANIC INTERFACES: THE CASE OF DONOR-ACCEPTOR INTERFACE IN ORGANIC SOLAR CELLS

6.1 Introduction

Organic photovoltaics (OPVs) holds promise of providing large-area, low-cost solar power conversion, with current multijunction devices exceeding 12% power conversion efficiency.[1,2] The active layers of these devices typically consist of two components, an electron donor and an electron acceptor, in either a bilayer structure or as a blend termed a bulk heterojunction. Morphology plays a critical role in the efficiencies of the various electronic and optical processes – including optical absorption, exciton formation, exciton migration, exciton dissociation, and charge collection – involved during solar cell operations, which are thought to be largely similar in the two device architectures.[3] While the importance of the donor-acceptor interface has been acknowledged in previous investigations,[4-10] of particular focus over the past few years has been the purity of the interface between the two materials. What was once thought to be fairly clear-cut interfaces between the donor and acceptor components, has been replaced by a complex morphological picture that includes pure domains with different extents of ordered and disordered packing and regions where the two materials are intermixed and where charge generation primarily occurs.[11-21]

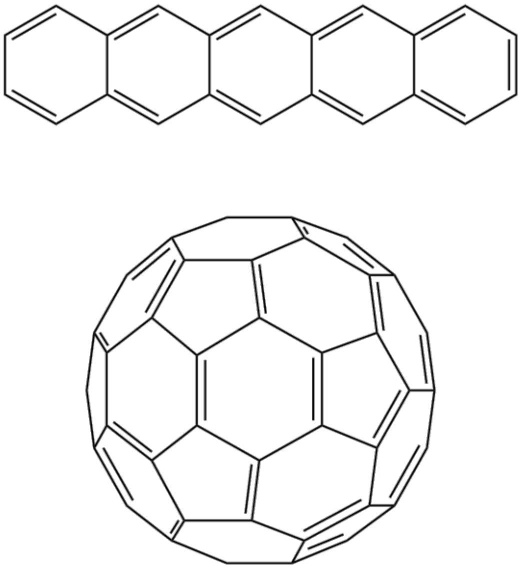

Figure 6.1. Chemical structures of pentacene (top) and the C_{60} Fullerene (bottom).

As discussed in Chapter 5, the energetic landscape at an interface is significantly different from that within the bulk of a crystalline material. One would expect, furthermore, the addition of a second organic component to further complicate the landscape. In the bulk of an organic molecular crystal or at an organic-vacuum interface all molecular sites are essentially identical, except for the difference in site energies due to nonequivalent molecules. In contrast, at organic-organic interfaces, the molecular sites reside in unique environments that will result in a distribution of site energies or polarization energies. Verlaak *et al*. showed, using the microelectrostatic model described in Chapter 1.3.3.1

and a static (fixed) configuration of the interface, that ideal ideal *edge-on* pentacene (001)/C_{60} interface presents an approximately 0.4 eV barrier to charge separation, while charge separation at a *face-on* pentacene (01-1)/C_{60} interface is quasi-barrierless, leading one to assume that the *face-on* orientation is preferable.[7] Yi *et al.*[6], however, showed that this is not necessarily the case, as the rate of charge recombination is calculated to be several orders-of-magnitude faster for the *face-on* orientation (10^{10} s^{-1}) than the *edge-on* orientation (10^{7} s^{-1}). For this reason we have chosen to focus on the *edge-on* pentacene/C_{60} interface for molecular dynamics (MD) studies, although we also consider the *face-on* orientation in some instances. Because of the anisotropic nature of the environment, the barrier to charge separation is expected to vary from site to site. By using a combination of MD simulations together with our methodology for determining the electronic polarization energy in organic molecular crystals, we provide in this Chapter a picture of the energetic landscape at a disordered pentacene/C_{60} interface, and observe how the landscape changes in time instead of considering only a static picture.

Thus, a major goal of this Chapter is to investigate how the polarization energy varies as a function of time. We begin by determining the polarization energy of a positive charge carrier in bulk pentacene and a negative charge carrier in bulk C_{60} and obtain good agreement with experiment. To assess the impact of molecular orientation at an interface we then look at model one-dimensional interfaces where pentacene is either *face-on* or *edge-on*. Finally, we examine a bilayer interface composed of bulk pentacene and C_{60} to assess the polarization energy at molecular sites along the interface and into the bulk in both static and dynamic frameworks; we also evaluate the non-interacting electron-hole energies and the geminate pair energies to observe how the barrier to charge separation changes as a function of time; we determine that the barrier to charge separation may vary by about 0.2 eV for the *edge-on* pentacene/C_{60} interface.

6.2 Computational Methodology

The geometries of the isolated pentacene molecules used for the AMOEBA force field parameterization and one-dimensional interfaces, and the unit cells used for bulk and the creation of the interfacial systems, were obtained from the Cambridge Structural Database (PENCEN04).[22,23] As an experimental crystal structure for C_{60} without solvent is not available, the Materials Studio 6.1 software suite was used to create a face-centered cubic C_{60} packing configuration where $\alpha = \beta = \gamma = 60^\circ$ and $a = b = c = 9.943\,\text{Å}$.

Single-point energy calculations at the MP2/6-31+G(d,p) level were performed on neutral, positively-charged, and negatively-charged pentacene, while single-point energy calculations at the B97D/6-31+G(d,p) level were also performed on each of the pentacene systems as well as neutral and negatively-charged C_{60} using the Gaussian 09 software suite.[24] The GDMA program of Stone was used to generate atom-centered multipoles for distributed multipole analysis.[25] Additional information on force-field parameterization is available in Chapter 2. The polarization energy for a given cluster was calculated using the Lyons model (Equations 1.3a and 1.3b) with the bulk polarization energy being determined by increasing the cluster radius and plotting the calculated polarization energies versus $\frac{1}{N^3}$, where N is the number of molecules in the cluster.[26-28]

One-dimensional interfaces were constructed using the isolated geometries from above, wherein each pentacene or C_{60} was replicated to give a total of 10 molecules each separated by 3.5 Å with a pentacene/C_{60} separation at the interface of 3.5 Å; see Figure 6.2. For both of the 1-dimensional interfaces, the chains are either perfectly co-facial or perfectly *edge-on*. Both of these configurations are different than what is observed for the actual materials (*i.e.,* within layers pentacene packs in a herringbone fashion and molecules do not sit perfectly on top of one another), but this simplified interface allows for the extreme of perfect order to be probed without introducing the added complexity of molecular rotation. Probable band bending at the interface is evaluated by placing either a positive or negative charge at the interface and moving towards the bulk.

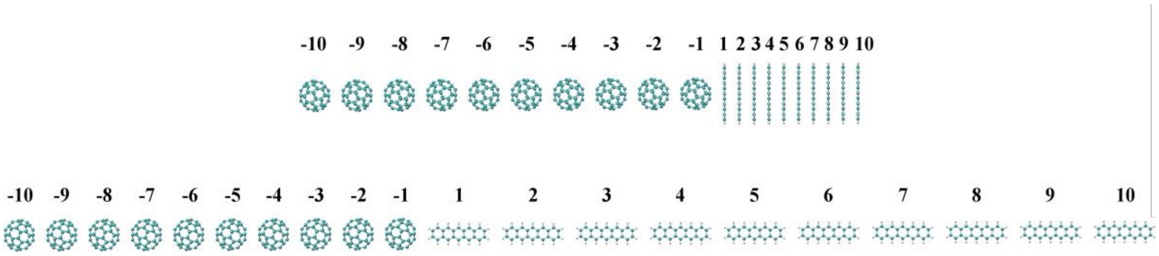

Figure 6.2. (Top) *Face-on* pentacene/C_{60} and (bottom) *edge-on* pentacene/C_{60} one-dimensional interfaces together with the numbering of the molecular sites. Note that only the six closest molecules to the interface have been considered as additional molecules introduce artifacts from the organic-vacuum interface at the edges of the systems.

The model pentacene/C_{60} interface was created by placing a C_{60} slab on top of a pentacene slab followed by a molecular mechanics MM3[29] minimization to optimize the separation distance at the interface. This configuration was then used as the initial configuration for MD simulations in the NVT ensemble at 300 K using the velocity Verlet integrator[30] and Berendsen thermostat.[31] A spherical cutoff of 12 Å for the summation of van der Waals interactions and Ewald summation[32] for Coulomb interactions was used. The rattle algorithm[33] was used to constrain C-H bonds. Polarization energies at various sites at the interface and sites in layers moving away from the bulk were then calculated.

6.3 Results and Discussion

6.3.1 Bulk Polarization Energy and DFT Parameterization

As a first step to exploring the effects of an organic-organic interface on the polarization energy due to an excess charge carrier, we have calculated the polarization energies of the respective bulk materials. In our previous investigations of electronic polarization energy the parameterization of the electrostatic component of the AMOEBA force field has been carried out via *ab initio* MP2 calculations followed by a distributed multipole analysis to generate atom-centered multipoles.[28,34] As shown in Figure 6.3, this parameterization procedure leads to the excess anion becoming localized to one portion of the C_{60} molecule. To obtain a charge distribution in which the charge is delocalized across the entirety of C_{60}, as one would expect from previous theoretical studies,[35,36] the parameterization of the electrostatic component was carried out using density functional theory at the B97D level.[37] This method results in an anionic C_{60} with charge evenly distributed across the entire molecule while maintaining a similar charge distribution for both anionic and cationic pentacene.

To validate this new parameterization, we calculated the polarization energies due to a positive charge and a negative charge in crystalline pentacene, and compared the DFT parameterized results to values obtained via MP2 parameterization, see Figure 6.4. For both charges there is minimal change in the calculated polarization energy: by -0.03 eV for a positive charge and by -0.02 eV for a negative charge when comparing the DFT results to the MP2 results. The polarization energy asymmetries for the MP2 and DFT parameterizations are 0.23 eV and 0.22 eV, respectively. Importantly, while there is a slight reduction in the polarization energies, the slope of the fitted extrapolations is essentially unchanged, leading one to conclude that the change in parameterization method leads to very minute quantitative differences between the two parameterizations for pentacene. As the DFT parameterization of pentacene results in a negligible change in the calculated polarization energies while also providing a charge distribution similar to what one would expect from previous studies, this new parameterization procedure should prove to be more robust than a model parameterized via Hartree-Fock calculations.

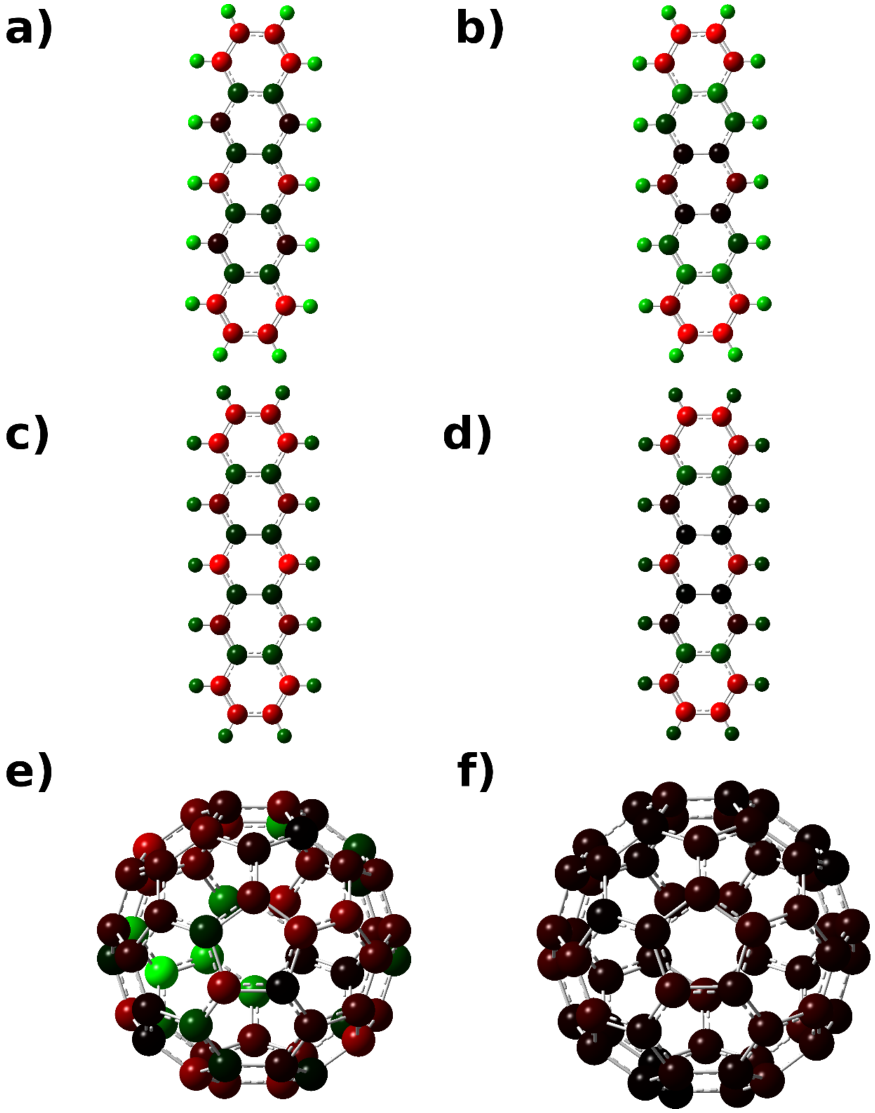

Figure 6.3. Charge distributions for pentacene cation (a, b), pentacene anion (c, d), and C$_{60}$ anion (e, f) as calculated at the MP2/6-31+G(d,p) (pentacene; left)), HF/6-31+G(d,p) (C$_{60}$; left), or B97D/6-31+G(d,p) (right) levels. Green represents partial positive charge and red represents partial negative charge.

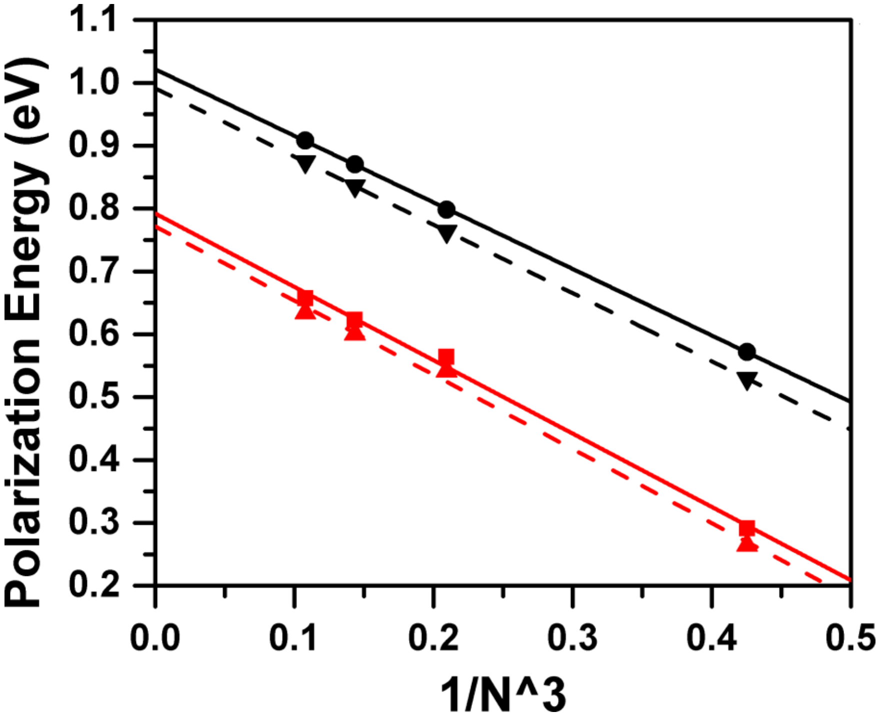

Figure 6.4. Electronic polarization energy of pentacene due to a positive charge (black) and negative charge (red) parameterized using the original MP2 method (solid line) and DFT method (dashed line).

Through the revised parameterization procedure, we determined the bulk polarization energy due to a positive charge in pentacene and a negative charge in C_{60}, since pentacene acts as an electron-donor and C_{60} acts as an electron-acceptor in the systems we wish to investigate. While there have been a number of studies that experimentally determined the polarization energy due to a positive charge in pentacene,[23,38-41] only Sato and co-workers[42] evaluated the polarization energy in C_{60} due to a positive or negative charge. Using the gas-phase ionization energy (IE) calculated by Lichtenberger and co-workers[43] and their solid-state IE, they estimate P_+ to be 1.1 eV, and by comparison to available gas-phase electron affinity (EA) data, estimate P_- to be larger than P_+ by some

0.3 eV – 0.5 eV, *i.e*., 1.4 eV – 1.6 eV. These numbers suggest that $P_{-} > P_{+}$ in C_{60}, which is opposite to the trend observed for the unsubstituted linear oligoacenes in Chapter 3.[28] This results from the absence of a molecular quadrupole in C_{60} and a zero charge-quadrupole interaction contribution. Thus, the polarization energy is determined by the induced interactions, where the anion is more stabilized that the cation, which is analogous to what was observed for TIPS-pentacene in Chapter 4.

Experimentally, there is an estimated difference of about 0.2 eV between the polarization energy due to a positive charge carrier in pentacene ($P_{+,P5}$) and the polarization energy due to a negative charge carrier in C_{60} ($P_{-,C_{60}}$).[39,42] Using our model, we have calculated each of the respective polarization energies through extrapolation of the polarization energy of finite clusters and observe that the polarization energy of a positive charge carrier in pentacene (0.99 eV) is some 0.27 eV larger than that of a negative charge carrier in C_{60} (0.72 eV), see Figure 6.5. This is in relative agreement with the calculations of D'Avino *et al.*[44] who have applied both the microelectrostatic and semiempirical models discussed in Chapter 2 to the bulk of pentacene and C_{60} to obtain differences, $P_{+,P5} - P_{-,C_{60}}$, of 0.07 eV and 0.16 eV, respectively, and the work of Gorczak *et al.*[8] who have calculated a difference of 0.31 eV.

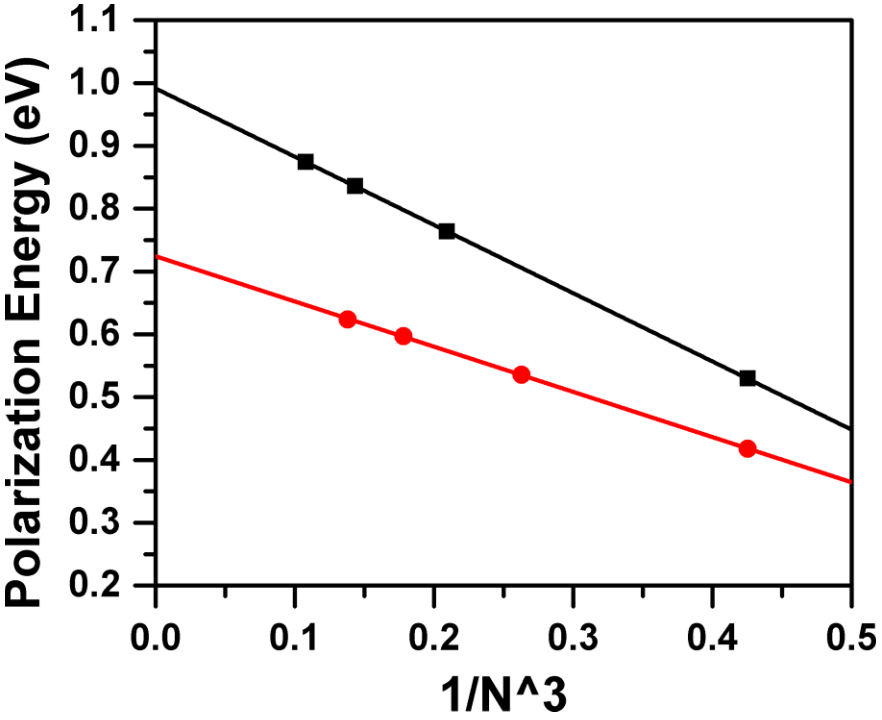

Figure 6.5. Electronic polarization energies for a positive charge in pentacene (black) and negative charge in C_{60} (red).

6.3.2 Band Bending in One-Dimensional Chains

To compare with previous theoretical results,[4,5] the band bending in one-dimensional donor-acceptor chains, see Figure 6.2, has been evaluated. These one-dimensional chains allow us to use a step-up approach and observe have the interactions change as the complexity of the system increases. Within these one-dimensional interfaces, each molecule is separated by 3.5 Å. We begin with a neutral system and then place a charge on either pentacene (site 1) or C_{60} (site -1) at the interface and move the charge to the nearest-neighbor away from the interface. At each site the IE or EA is calculated as a function of molecular position (Figure 6.6).

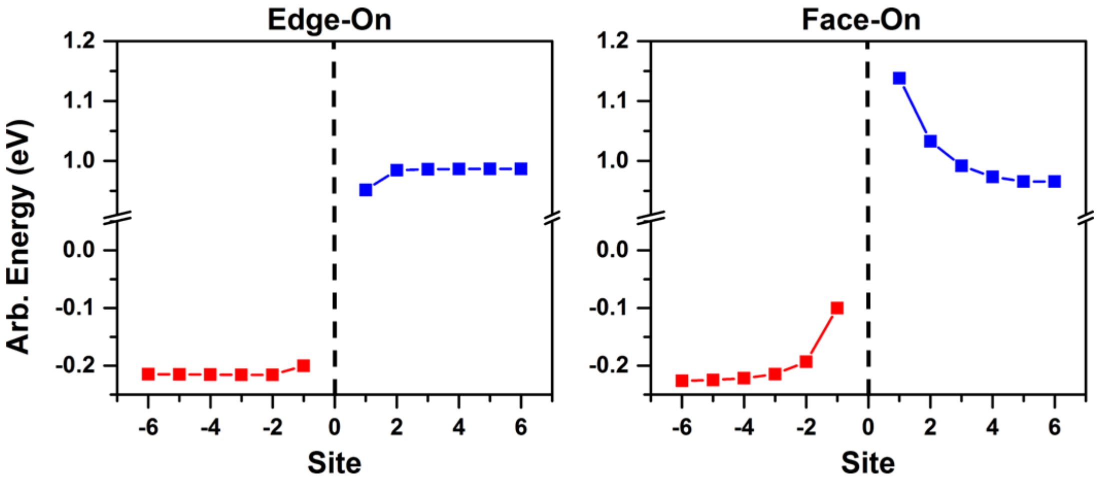

Figure 6.6. Shift in the ionization energy of pentacene (blue) and electron affinity of C_{60} (red) for an *edge-on* pentacene/C_{60} interface (left) and *face-on* pentacene/C_{60} interface (right). A more negative value for the EA represents a larger, *i.e*., more stabilizing, EA. For the IE, a more positive value represents a larger IE, *i.e*., less stabilizing.

There is a destabilization of the electron on C_{60} as it is moved towards the interface for both orientations of pentacene with the *face-on* pentacene configuration having a larger destabilization. This is a result of the larger charge-quadrupole interactions in the *face-on* orientation and the increased magnitude of the induced dipoles, as previously shown by Linares *et al*.[4] Also note, as we have discussed in Chapter 5, that for *edge-on* pentacene, which is similar to the *inter*layer packing in bulk pentacene, the band bending and thus the polarization energy changes very little after moving one layer from the interface (*i.e*., sites other than 1 or 2). For the *face-on* orientation, which is somewhat similar to the *intra*layer packing, the band bending falls off much more slowly, not saturating until the charge is on site 5 for pentacene; this is consistent with the behavior observed in the bulk, where the polarization energy does not stabilize until about 4 nm from the charge carrier.

For pentacene, there is also a qualitative change in the band bending wherein a hole is destabilized at the interface for a *face-on* pentacene interface and stabilized at the *edge-on* interface. Again, this results from the change in quadrupole interactions where in the *edge-on* orientation the charged pentacene interacts with a small positive quadrupole on the neighboring pentacene and in the *face-on* orientation the charged pentacene interacts with a large negative quadrupole, *i.e*. positive-negative interaction *vs*. negative-negative interaction.

Looking more closely at the neutral systems, there is an induced dipole at the interface due to the quadrupole moment of pentacene. This induced dipole impacts not only the molecules at the interface but also induces dipole moments along the chain as one moves away from the interface, although with lessening strength approaching zero far from the interface. Depending on the orientation of the pentacenes, the direction of the induced dipole is different as the sign of the quadrupole component closest to C_{60} changes, *i.e*., the induced dipole points towards the C_{60} bulk for *face-on* pentacene and towards the pentacene bulk for *edge-on* pentacene (Figure 6.7). Also note that the induced dipole is an order-of-magnitude smaller for the *edge-on* pentacene configuration, a result of the small quadrupole moment and larger distance between additional atom-centers.

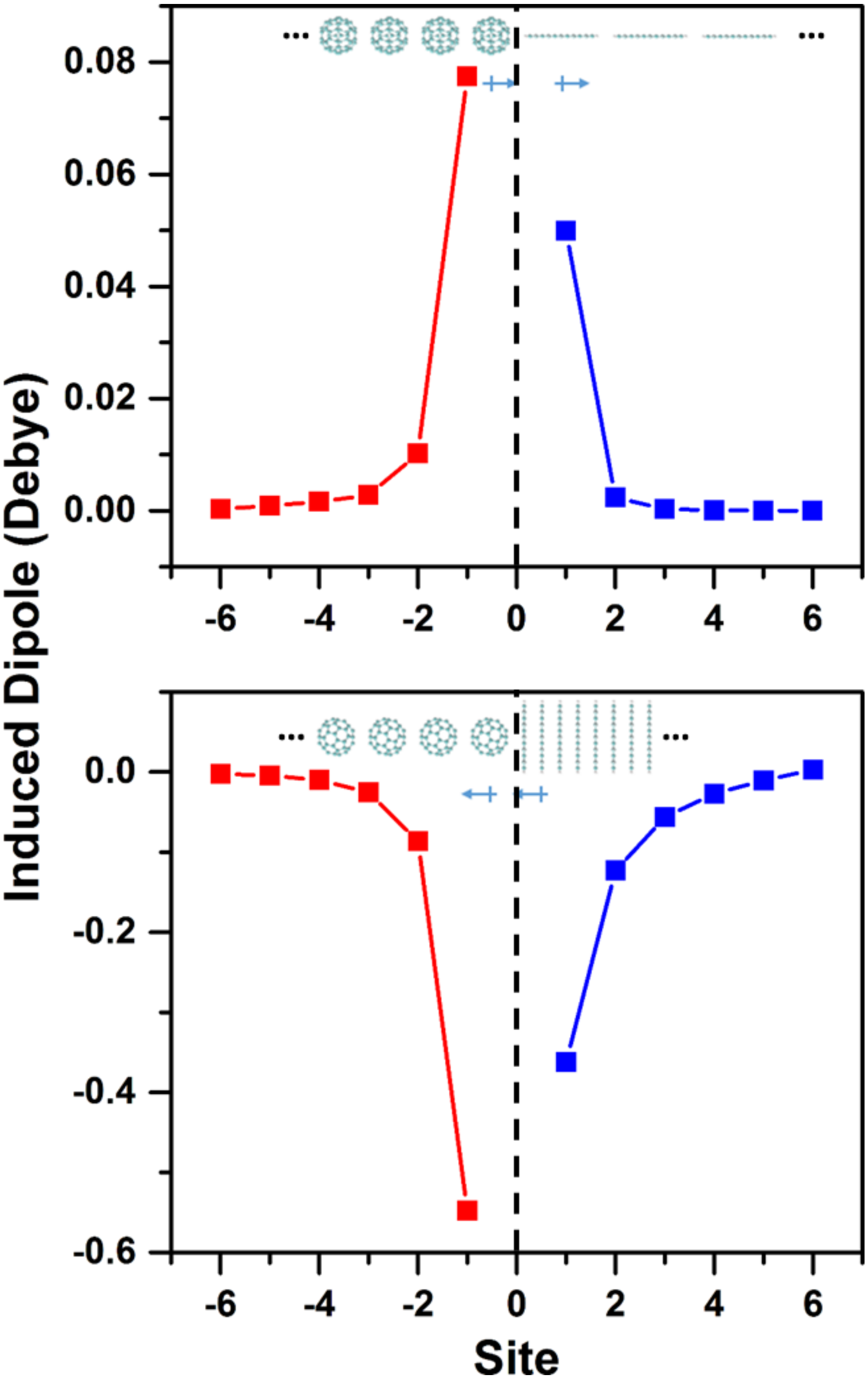

Figure 6.7. Induced dipoles on pentacene (blue) and C_{60} (red) at a model one-dimensional interface where each molecular site is separated by 3.5 Å in an *edge-on* orientation (top) and a *face-on* orientation (bottom). Insert: Illustration of the orientation of the induced dipoles of the interfacial molecules and representation of the molecular systems.

Through the use of one-dimensional chains, one observes that in a highly ordered system the driving force for charges to separate is small for the *edge-on* pentacene orientation and quite large for the *face-on* orientation. These differences stem from a combination of static multipole and dynamic induced-dipole contributions. If the orientation of just a few molecules presents such pronounced effects on a charge at the interface, then the effects of many additional neighbors, causing the electrostatic environment of each molecule to vary, should have an equally important impact.

6.3.3 Polarization Energy and Induced Dipoles at Model Bilayer Interfaces

As the complexity of the model systems is increased, an idealized *edge-on* pentacene/C_{60} interface is considered next, created by layering crystalline surfaces of pentacene and C_{60}, followed by minimization using the MM3 force field to optimize the interface separation distance, see Figure 6.8. From such a static model interface,[4,7,8] it is readily seen in Figure 6.9 that there is a broad range of polarization energies within the pentacene and C_{60} layers, making each site distinctive. For pentacene, the polarization energy due to a positive charge carrier in a 4 nm radius cluster, ranges from 0.76 eV to 0.92 eV, while a negative charge carrier in C_{60} can undergo a polarization stabilization of 0.56 eV to 0.81 eV. The 0.2 to 0.3 eV range in polarization energy for each site suggests that the electrostatic environment of each molecule varies significantly due to the presence of the additional organic material.

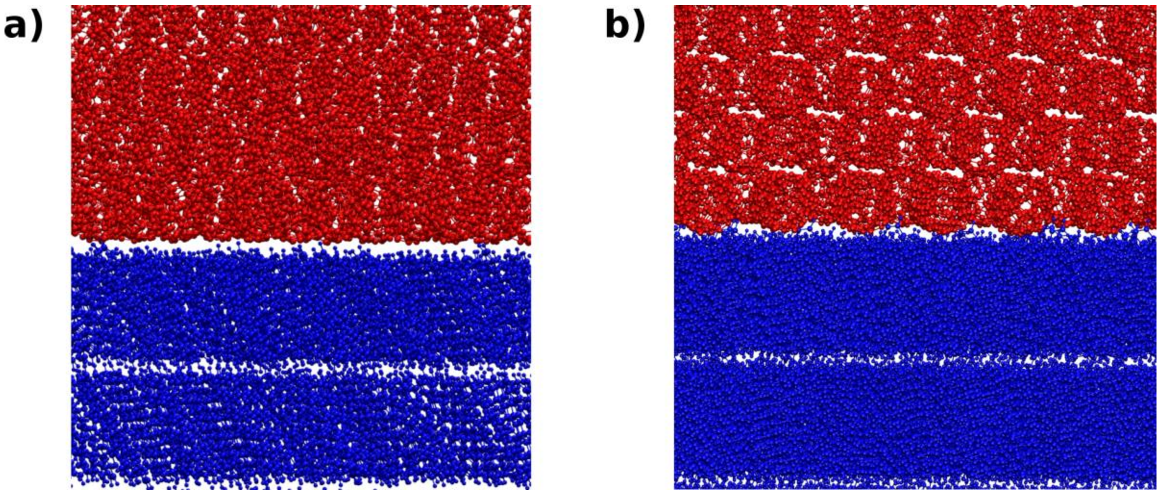

Figure 6.8. (a) MM3 minimized interface between a slab each of C_{60} (red) and *edge-on* pentacene (blue). (b) Interface between C_{60} and *edge-on* pentacene after 1 ns MD simulation at 300 K using the MM3 force field.

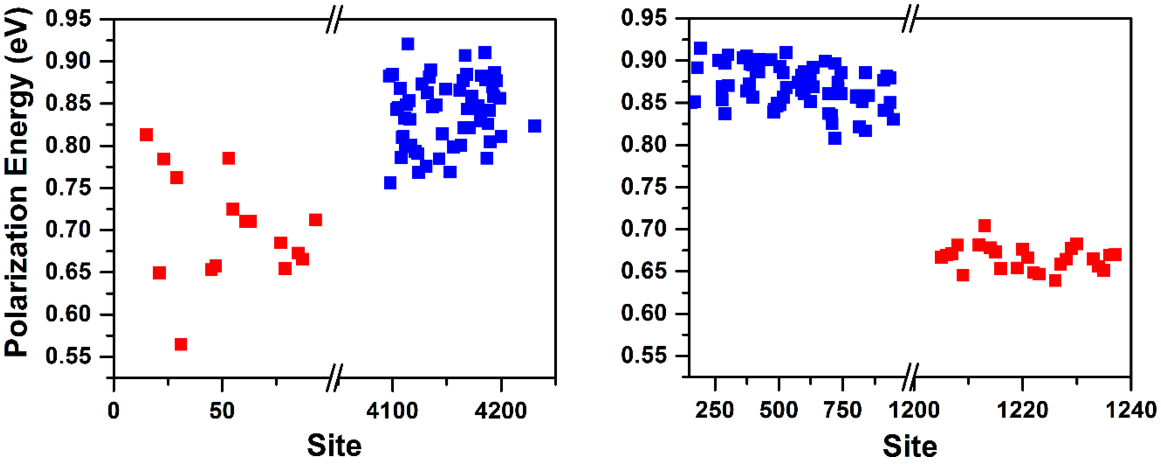

Figure 6.9. Polarization energy for a negative charge carrier in C_{60} (red) and a positive charge carrier in pentacene (blue) at the interface of the two organic components within spherical clusters with a 4 nm radius. Two systems are considered: (Left) A slab of pentacene and a slab of C_{60} glued together followed by a MM3 minimization. (Right) The same system after 1 ns of MD simulation at 300 K.

The MD simulations of Fu *et al*. have shown that the pentacene/C_{60} interface is more complex that is typically accounted for, with the layers undergoing some amount of mixing.[14] To provide a more complete picture, as compared to a static interface composed of two slabs, the MM3 force field has been used for MD simulations to model a disordered interface due to the dynamic processes that occur at room temperature. Following reported methods,[14] we simulated an *edge-on* bilayer interface consisting of six layers of pentacene and 14 layers of C_{60} to give a unit cell of (x=) 6.8 nm x (y=) 6.8 nm x (z=) 50 nm, where a large vacuum space has been included to keep supercell periodicity limited to the xy-plane. This system was equilibrated for 1 ns and then replicated in each of the x and y directions to give a final supercell of 13.7 nm x 13.7 nm x 50 nm composed of 4752 pentacene and 2744 C_{60} molecules, this was followed by a final equilibration of 10 ps and data collection for another 10 ps. The largest energy fluctuation during data collection was about 0.02% of the total energy with a standard deviation of less than 0.01 % (about 67 kcal/mol). We observe that the C_{60} takes on a hexagonal closed packing configuration as has been reported previously.[14]

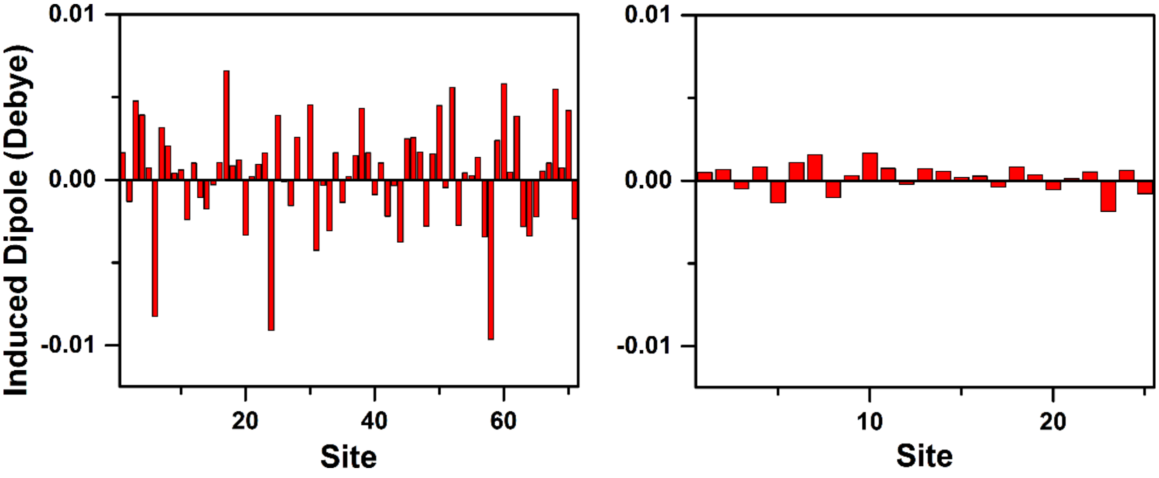

Figure 6.10. The *z*-component of the induced dipole on pentacene (left) and C_{60} (right), as a function of molecular site at a neutral *edge-on* interface.

We considered 25 C_{60} and 71 pentacenes at the interface, extracted from a single MD snapshot after equilibration was reached, for comparison to the molecular-mechanics minimized static interface and analysis of how the interface changes in a dynamic way. Note that the molecular sites are not identical, as highlighted by the large variation in the induced dipole for sites along the interface (Figure 6.10). The largest qualitative difference between the minimized and dynamic interfaces is the narrowing of the distribution of site polarization energies and an increase in the average difference between the polarization energies due to a positive or negative charge (0.14 eV, minimized; 0.21 eV, dynamic); the average polarization energy due to each charge type also increases by ~0.1 eV. This indicates that during the MD simulations the thermal fluctuations act to minimize the overall differences among molecular sites, while these still remain distinct. It is interesting to note that while the site polarization energies are more uniform in the MD snapshot, the sites display a large number of configurations, including pentacene partially moving from the pentacene layer to the space between C_{60} molecules. These dislocations do not result in large changes of the polarization energy.

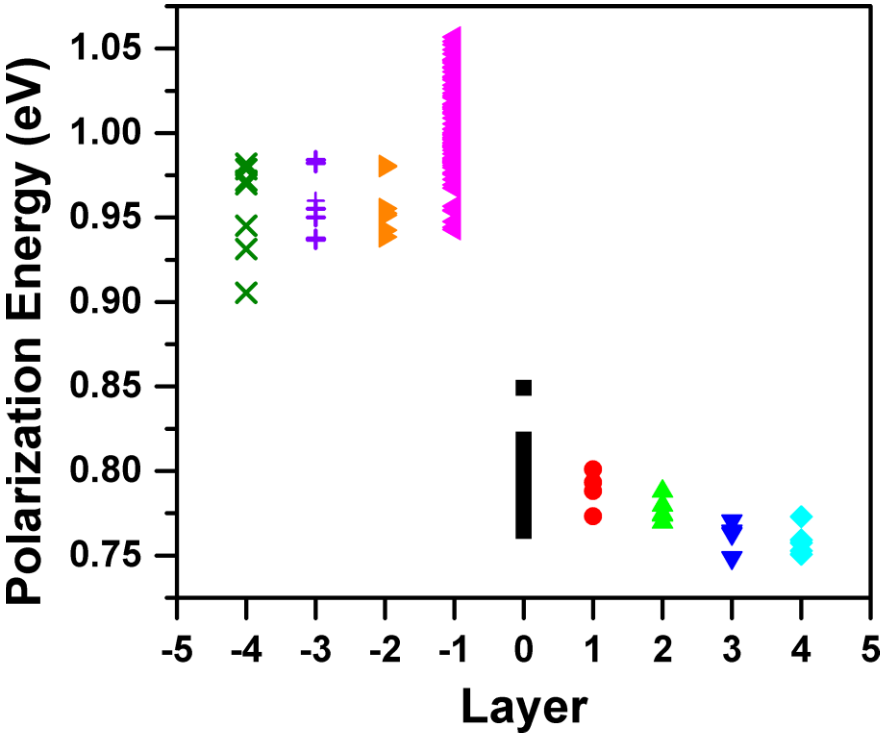

Figure 6.11. Polarization energy due to a positive charge in pentacene and negative charge in C_{60} as a function of molecular layer with respect to the interface. The C_{60} layers considered are: the C_{60} interfacial layer (■, black), 1 layer from the interface (●, red), 2 layers from the interface (▲, green), 3 layers from the interface (▼, blue), and 4 layers from the interface (♦, cyan), with the latter approximating the bulk. The pentacene layers considered are: the interfacial pentacene layer (◀, magenta), 1 layer from the interface (▶, orange), 2 layers from the interface (+, purple), and 3 layers from the interface (×, green), with the latter approximating the bulk.

Using this same snapshot we may then probe molecular sites as the charge is moved away from the interface towards the bulk to observe how the polarization energy changes as a function of molecular layer, see Figure 6.11. Similar to the rubrene and tetracene organic-vacuum interfaces of Chapter 5, we observe that there is a large change in the polarization energy when moving from the interfacial layer of pentacene to one layer from the interface and then little change upon moving farther from the interface. In contrast to an organic-vacuum interface, where the polarization energy at the interface is lower than the bulk, the average polarization energy at the considered organic-organic interface is larger than in the bulk. In an organic-vacuum interface, there is a reduction in the number of polarizable points resulting in a smaller polarization energy; in the pentacene/C_{60} interface, there are still polarizable points, but no static quadrupoles in the second organic component, C_{60}, which would otherwise act to reduce the polarization energies. This causes a net increase in the polarization energy at each molecular site.

A similar trend is seen on the C_{60} side of the interface, though the polarization does not stabilize until the charge moves three layers away from the interface because of the hexagonal closest packed configuration that results in layers that are less well separated than in pentacene. Since the positive quadrupole component of the pentacene is pointed towards the C_{60} slab, the negative charge is more stabilized at the interface than in the bulk, which increases the polarization energy due to a negative charge at the interface as observed for the one-dimensional systems.

Finally, moving onto the examination of site polarization energy as a function of time (Figure 6.12), snapshots were taken at 0.5 ps intervals where the polarization energy at five C_{60} sites and 19 pentacene sites was followed; each collection of sites on either side of the interface occupies a similar area. Compared to the single snapshot, the polarization energy distributions over the whole timespan are larger, where the P_- distribution is ~5%

larger and the P_+ distribution is ~30% larger, indicating that the environment of the pentacene sites vary much more than the C_{60} sites. While it is not unexpected that the polarization energy can vary by a large amount from site to site as the environment of each site is distinct, the large amount that each individual site may change is more interesting. For C_{60}, the polarization energy of a given site is observed to vary by as much as 9% (~0.07 eV) with respect to the site's smallest polarization energy, while the polarization energy of pentacene sites can vary by up to 12% (~0.12 eV).

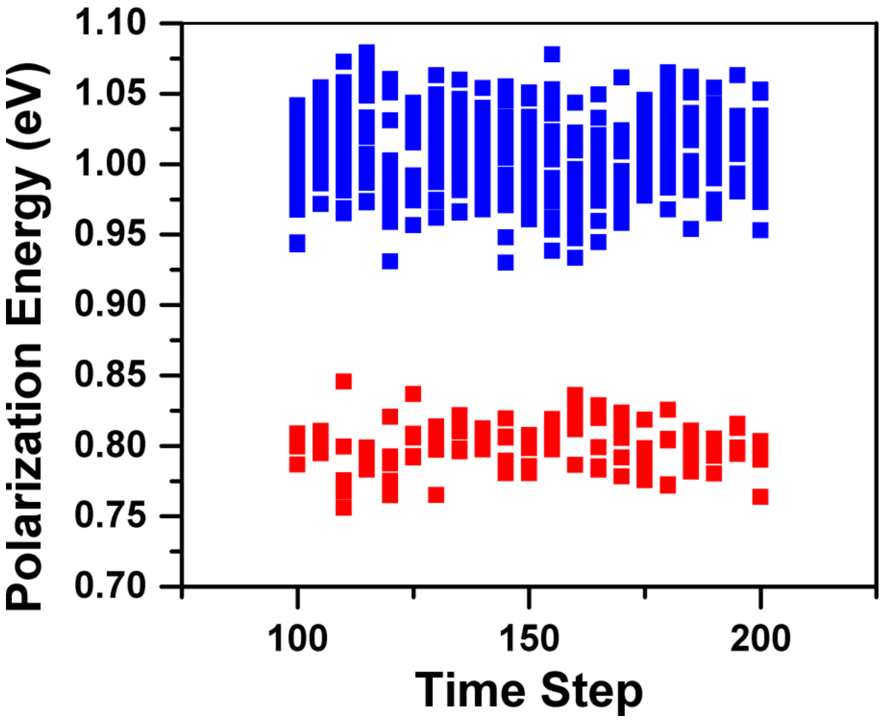

Figure 6.12. Polarization energies at selected sites of pentacene (blue) and C_{60} (red) as a function of time in 0.5 ps increments.

6.3.4 Interface Impact on Charge Separation

The process of exciton dissociation and charge separation is a highly debated topic in the literature.[45-51] The barrier, or lack thereof, to the charge separation process has been the focus of numerous articles with reports as large as 1.4 eV for charge separation in Alq_3 thin films to barriers of less than 10 meV in polymer-fullerene blends where the charge carriers are expected to be largely delocalized.[48,52-57] Theoretical investigations report similar estimates;[7,8] for instance, the interface geometry has been a significant focus of the work of Heremans and co-workers,[7] who report the barrier to charge separation at the pentacene/C_{60} interface to vary from ~0 eV to 0.4 eV as a function of pentacene orientation, while the group of Grozema and co-workers[8] report a barrier to charge separation in an *edge-on* pentacene/C_{60} interface to be as large as 0.85 eV.

To provide additional insight into the charge-separation process, we evaluated the energy of a non-interacting electron-hole pair (E_{NI-EH}), defined as:

$$E_{NI-EH} = P_+ + P_- \tag{6.2}$$

where P_+ and P_- may either correspond to the bulk or interface, and compared it to the energy of a Coulombically-bound electron-hole pair (E_{EH}), defined as:

$$E_{EH} = \Delta E_{pair} - IE_{gas} - EA_{gas} \tag{6.3}$$

where ΔE_{pair} is the change in energy of the system between the presence of the charge pair and the absence of the charge pair. As we have done with the polarization energy of different molecular sites, we have tracked each of these quantities along a MD trajectory to determine how the electrostatic environment of the electron-hole pair changes at a disordered interface as a function of time.

Note that there are two primary configurations of pentacene and C_{60} at the pentacene/C_{60} interface: a first one (Figure 6.13, left) where C_{60} sits directly on top of a pentacene and a second one (Figure 6.13, right) where C_{60} sits above three neighboring pentacene.

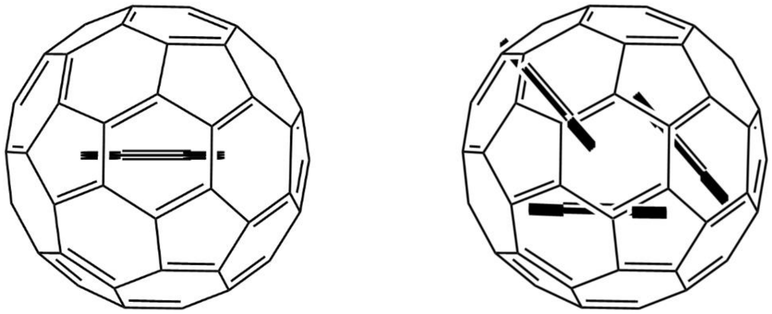

Figure 6.13. Top-down representations of the primary pentacene and C_{60} configurations at the pentacene/C_{60} interface.

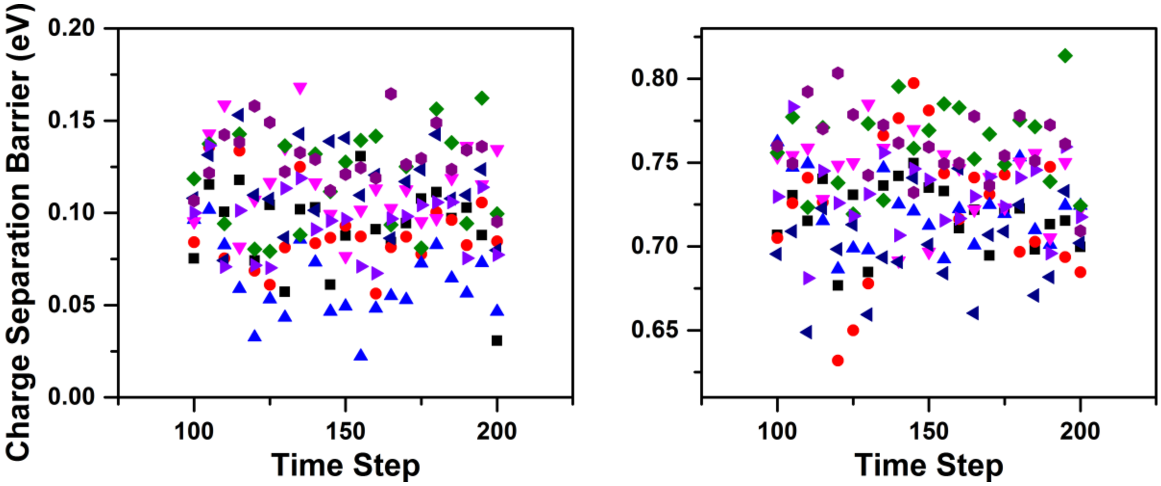

Figure 6.14. (Left) Charge separation barrier for a non-interacting electron-hole pair for eight pairs. (Right) Charge separation barrier for an interacting electron-hole pair for eight pairs. Symbols correspond to the same pairs in both plots.

Looking at a single snapshot from the MD trajectory and comparing the sites within this single frame, we observe that charge separation for a non-interacting electron-hole pair $E_{CS,NI-EH} = E_{NI-EH,\text{int}} - E_{NI-EH,\text{bulk}}$ can vary by as much as 0.13 eV from site-to-site, the same order of magnitude as $E_{CS,NI-EH}$ itself, see Figure 6.14. While $E_{CS,NI-EH}$ does become as small as 0.02 eV, it never appears to become negative. This shows that while the barrier of charge separation for a non-interaction pair may vary by a large amount, the electron and hole are more stable at the interface than in the bulk, to within *kT*.

These calculations, though, do not account for mutual interactions, either inductive or electrostatic, between the hole and electron. However, these interactions are key to properly describing the evolution from a Coulombically-bound electron-hole pair to free charge carriers in the bulk. Analogous to the non-interacting electron-hole pair, we may define the charge separation energy as $E_{CS,EH} = E_{EH,\text{int}} - E_{EH,\text{bulk}}$ where

$E_{\text{EH,bulk}} = E_{NI-EH,\text{bulk}}$ since the hole and electron in their respective bulk are separated enough to have no interaction.

Considering eight electron-hole pairs from a single MD snapshot, we observe that the barrier to charge separation ranges from 0.70 eV to 0.76 eV. These values fall between the previously reported barriers of Grozema and co-workers (0.85 eV)[8] and Heremans and co-workers (0.44 eV).[7] Although these values cover a wide range of energies, it is important to note the differences in these models. While our results agree well with those of Grozema and co-workers, the microelectrostatic model underestimates the charge-separation barrier. This is likely due to the sub-molecular representation of pentacene (described via five points) and C_{60} (described by 12 points); this approximations leads to an overestimation of the polarizability of the molecules and causes the respective bulk regions to over-stabilize the excess charges, which allows for more facile charge separation.[4]

By comparing $E_{CS,EH}$ and $E_{CS,NI-EH}$ the mutual interaction contribution to charge separation may be quantified. These interactions account for the majority of the barrier to charge separation for the interacting pair, upwards of 90% of $E_{CS,EH}$. Thus, it is the change in inductive and electrostatic interactions of the environment when the two opposite charges are near each other that dictates the charge separation barrier. To minimize the barrier to charge separation, it is then necessary to reduce the contributions from these mutual interactions. One approach is the use of a *face-on* pentacene orientation; however, as stated earlier, such an orientation is calculated to cause a large increase in the rate of charge recombination.[6]

This single, static picture, though, does not fully describe the complexity of the pentacene/C_{60} interface, as the individual molecules move in time. For any given site, we observe that $E_{CS,EH}$ varies by as much as 0.17 eV, nearly as much as the largest differences in $E_{CS,EH}$ observed for all sites over a range of 0.5 ps (0.18 eV; from 0.63 eV to 0.81 eV). This large variation in the barrier to charge separation, while not large enough to suggest barrier-less charge separation, must be considered when static pictures of the charge-separation energy are presented.

6.4 Conclusions

Through the use of a combination of quantum-mechanics calculations and molecular-mechanics and molecular-dynamics simulations, we have investigated the effect of the bulk and of an organic-organic interface on the energy of an excess charge carrier. For the bulk materials, we observe that a positive charge in pentacene is more stabilized by its environment than a negative charge in C_{60} (by about 0.27 eV), in agreement with available experimental estimates. When considering a model pentacene/C_{60} bilayer interface consisting of one-dimensional chains, we show that both hole and electron are stabilized at the *edge-on* pentacene interface while a hole is destabilized at the *face-on* pentacene interface. Moving towards more complex systems, we then examined a bulk *edge-on* pentacene/C_{60} interface where a slab of pentacene is glued to a slab of C_{60} and a similar interface after 1 ns of molecular dynamics simulation. We observe that each site at the interface is indeed unique. As such, a range of polarization energies must be considered, as compared to the bulk in which the environment of each molecular site is essentially equivalent. We also find that the polarization energy for both a hole in pentacene and an electron in C_{60} can be greater at the interface than the bulk, which leads to a charge more stabilized at the interface, although due to the different environment of each molecular site this is not always necessarily the case. Lastly, using molecular dynamics, we looked at the barrier to charge separation for an electron-hole pair as it changes in time and at different molecular sites. We observe that the barrier can fluctuate by as much as about 25% of the total charge separation energy.

An important message from our studies is that the energetic landscape at a bilayer interface is more complex than is often considered, with the environment of each molecular site changing considerably over time. While the charge separation energies that we have reported here would seem to indicate that efficient charge separation is not possible in such bilayer configurations, we note that charge delocalization would increase the mean distance between charge centers and thus decrease the magnitude of the charge-separation barrier. Overall, consideration of the large variation of site environments at the interface must be properly taken into account if we are to better understand the electronic processes at organic-organic interfaces.

6.5 References

(1) NREL. NREL Best Research-Cell Efficiencies. Published Online: 2015. http://www.nrel.gov/ncpv/images/efficiency_chart.jpg (accessed March 23, 2015).

(2) Heliatek http://www.heliatek.com/newscenter/latest_news/neuer-weltrekord-fur-organische-solarzellen-heliatek-behauptet-sich-mit-12-zelleffizienz-als-technologiefuhrer/?lang=en#, 2013.

(3) Bredas, J. L.; Norton, J. E.; Cornil, J.; Coropceanu, V. *Acc. Chem. Res.* **2009**, *42*, 1691.

(4) Linares, M.; Beljonne, D.; Cornil, J. r. m.; Lancaster, K.; Brédas, J.-L.; Verlaak, S.; Mityashin, A.; Heremans, P.; Fuchs, A.; Lennartz, C.; Idé, J.; Méreau, R. l.; Aurel, P.; Ducasse, L.; Castet, F. d. r. *J. Phys. Chem. C* **2010**, *114*, 3215.

(5) Mothy, S.; Guillaume, M.; Idé, J.; Castet, F.; Ducasse, L.; Cornil, J.; Beljonne, D. *J. Phys. Chem. Lett.* **2012**, *3*, 2374.

(6) Yi, Y. P.; Coropceanu, V.; Bredas, J. L. *J. Am. Chem. Soc.* **2009**, *131*, 15777.

(7) Verlaak, S.; Beljonne, D.; Cheyns, D.; Rolin, C.; Linares, M.; Castet, F.; Cornil, J.; Heremans, P. *Adv. Funct. Mater.* **2009**, *19*, 3809.

(8) Gorczak, N.; Swart, M.; Grozema, F. C. *J. Mater. Chem. C* **2014**, *2*, 3467.

(9) Castet, F.; D'Avino, G.; Muccioli, L.; Cornil, J.; Beljonne, D. *Phys. Chem. Chem. Phys.* **2014**, *16*, 20279.

(10) Beljonne, D.; Cornil, J.; Muccioli, L.; Zannoni, C.; Bredas, J. L.; Castet, F. *Chem. Mater.* **2011**, *23*, 591.

(11) Coakley, K. M.; McGehee, M. D. *Chem. Mater.* **2004**, *16*, 4533.

(12) Casalegno, M.; Carbonera, C.; Luzzati, S.; Raos, G. *Org. Elect.* **2012**, *13*, 750.

(13) Bartelt, J. A.; Beiley, Z. M.; Hoke, E. T.; Mateker, W. R.; Douglas, J. D.; Collins, B. A.; Tumbleston, J. R.; Graham, K. R.; Amassian, A.; Ade, H.; Fréchet, J. M. J.; Toney, M. F.; McGehee, M. D. *Adv. Energy Mater.* **2013**, *3*, 364.

(14) Fu, Y.-T.; Risko, C.; Brédas, J.-L. *Adv. Mater.* **2013**, *25*, 878.

(15) Correia, H. M. G.; Barbosa, H. M. C.; Marques, L.; Ramos, M. M. D. *Thin Solid Films* **2014**, *560*, 59.

(16) Bloking, J. T.; Giovenzana, T.; Higgs, A. T.; Ponec, A. J.; Hoke, E. T.; Vandewal, K.; Ko, S.; Bao, Z.; Sellinger, A.; McGehee, M. D. *Adv. Energy Mater.* **2014**, *4*, n/a.

(17) Mladenović, M.; Vukmirović, N. *Adv. Funct. Mater.* **2015**, *25*, 1915.

(18) Gehrig, D. W.; Howard, I. A.; Sweetnam, S.; Burke, T. M.; McGehee, M. D.; Laquai, F. *Macromol. Rapid Commun.* **2015**, n/a.

(19) Buchaca-Domingo, E.; Vandewal, K.; Fei, Z.; Watkins, S. E.; Scholes, F. H.; Bannock, J. H.; de Mello, J. C.; Richter, L. J.; DeLongchamp, D. M.; Amassian, A.; Heeney, M.; Salleo, A.; Stingelin, N. *J. Am. Chem. Soc.* **2015**, *137*, 5256.

(20) Noriega, R.; Rivnay, J.; Vandewal, K.; Koch, F. P. V.; Stingelin, N.; Smith, P.; Toney, M. F.; Salleo, A. *Nat. Mater.* **2013**, *12*, 1038.

(21) Collins, B. A.; Tumbleston, J. R.; Ade, H. *J. Phys. Chem. Lett.* **2011**, *2*, 3135.

(22) Allen, F. H. *Acta Crystallogr.* **2002**, *B58*, 380.

(23) Mattheus, C. C.; Dros, A. B.; Baas, J.; Meetsma, A.; Boer, J. L. d.; Palstra, T. T. M. *Acta Crystallogr., Sect. C: Cryst. Struct. Commun.* **2001**, *57*, 939.

(24) Frisch, M. J.; Trucks, G. W.; Schlegel, H. B.; Scuseria, G. E.; Robb, M. A.; Cheeseman, J. R.; Scalmani, G.; Barone, V.; Mennucci, B.; Petersson, G. A.; Nakatsuji,

H.; Caricato, M.; Li, X.; Hratchian, H. P.; Izmaylov, A. F.; Bloino, J.; Zheng, G.; Sonnenberg, J. L.; Hada, M.; Ehara, M.; Toyota, K.; Fukuda, R.; Hasegawa, J.; Ishida, M.; Nakajima, T.; Honda, Y.; Kitao, O.; Nakai, H.; Vreven, T.; Montgomery Jr., J. A.; Peralta, J. E.; Ogliaro, F.; Bearpark, M. J.; Heyd, J.; Brothers, E. N.; Kudin, K. N.; Staroverov, V. N.; Kobayashi, R.; Normand, J.; Raghavachari, K.; Rendell, A. P.; Burant, J. C.; Iyengar, S. S.; Tomasi, J.; Cossi, M.; Rega, N.; Millam, N. J.; Klene, M.; Knox, J. E.; Cross, J. B.; Bakken, V.; Adamo, C.; Jaramillo, J.; Gomperts, R.; Stratmann, R. E.; Yazyev, O.; Austin, A. J.; Cammi, R.; Pomelli, C.; Ochterski, J. W.; Martin, R. L.; Morokuma, K.; Zakrzewski, V. G.; Voth, G. A.; Salvador, P.; Dannenberg, J. J.; Dapprich, S.; Daniels, A. D.; Farkas, Ö.; Foresman, J. B.; Ortiz, J. V.; Cioslowski, J.; Fox, D. J.; Gaussian, Inc.: Wallingford, CT, USA, 2009.
(25) Stone, A. J. *J. Chem. Theory Comput.* **2005**, *1*, 1128.
(26) Lyons, L. *Aust. J. Chem.* **1957**, *10*, 365.
(27) Silinsh, E. A. *Organic Molecular Crystals: Their Electronic States*; Springer: New York, 1980.
(28) Ryno, S. M.; Lee, S. R.; Sears, J.; Risko, C.; Bredas, J. L. *J. Phys. Chem. C* **2013**, *117*, 13853.
(29) Lii, J. H.; Allinger, N. L. *J. Am. Chem. Soc.* **1989**, *111*, 8576.
(30) Swope, W. C.; Andersen, H. C.; Berens, P. H.; Wilson, K. R. *J. Chem. Phys.* **1982**, *76*, 637.
(31) Berendsen, H. J. C.; Postma, J. P. M.; van Gunsteren, W. F.; DiNola, A.; Haak, J. R. *J. Chem. Phys.* **1984**, *81*, 3684.
(32) Darden, T.; York, D.; Pedersen, L. *J. Chem. Phys.* **1993**, *98*, 10089.
(33) Andersen, H. C. *J. Comput. Phys.* **1983**, *52*, 24.
(34) Ryno, S. M.; Risko, C.; Brédas, J.-L. *J. Am. Chem. Soc.* **2014**, *136*, 6421.
(35) Gastel, M. v. *J. Phys. Chem. A* **2010**, *114*, 10864.
(36) Green, W. H.; Gorun, S. M.; Fitzgerald, G.; Fowler, P. W.; Ceulemans, A.; Titeca, B. C. *J. Phys. Chem.* **1996**, *100*, 14892.
(37) Note that previous electronic structure calculations have shown the calculated charge distribution of fullerene anion to be highly sensitive to the amount of included Hartree-Fock exchange.
(38) Sato, N.; Seki, K.; Inokuchi, H. *J. Chem. Soc., Faraday Trans. 2* **1981**, *77*, 1621.
(39) Sato, N.; Inokuchi, H.; Silinsh, E. A. *Chem. Phys.* **1987**, *115*, 269.
(40) Qi, Y.; Mohapatra, S. K.; Kim, S. B.; Barlow, S.; Marder, S. R.; Kahn, A. *Appl. Phys. Lett.* **2012**, *100*, 083305.
(41) Chan, C.; Kahn, A. *Appl. Phys. A* **2009**, *95*, 7.
(42) Sato, N.; Saito, Y.; Shinohara, H. *Chem. Phys.* **1992**, *162*, 433.
(43) Lichtenberger, D. L.; Nebesny, K. W.; Ray, C. D.; Huffman, D. R.; Lamb, L. D. *Chem. Phys. Lett.* **1991**, *176*, 203.
(44) D'Avino, G.; Muccioli, L.; Zannoni, C.; Beljonne, D.; Soos, Z. G. *J. Chem. Theory Comput.* **2014**.
(45) Heeger, A. J. *Adv. Mater.* **2014**, *26*, 10.
(46) Tvingstedt, K.; Vandewal, K.; Zhang, F.; Inganäs, O. *J. Phys. Chem. C* **2010**, *114*, 21824.

(47) Jailaubekov, A. E.; Willard, A. P.; Tritsch, J. R.; Chan, W.-L.; Sai, N.; Gearba, R.; Kaake, L. G.; Williams, K. J.; Leung, K.; Rossky, P. J.; Zhu, X. Y. *Nat. Mater.* **2013**, *12*, 66.
(48) Clarke, T. M.; Durrant, J. R. *Chem. Rev.* **2010**, *110*, 6736.
(49) Deibel, C.; Strobel, T.; Dyakonov, V. *Adv. Mater.* **2010**, *22*, 4097.
(50) Etzold, F.; Howard, I. A.; Mauer, R.; Meister, M.; Kim, T.-D.; Lee, K.-S.; Baek, N. S.; Laquai, F. *J. Am. Chem. Soc.* **2011**, *133*, 9469.
(51) Vandewal, K.; Albrecht, S.; Hoke, E. T.; Graham, K. R.; Widmer, J.; Douglas, J. D.; Schubert, M.; Mateker, W. R.; Bloking, J. T.; Burkhard, G. F.; Sellinger, A.; Fréchet, J. M. J.; Amassian, A.; Riede, M. K.; McGehee, M. D.; Neher, D.; Salleo, A. *Nat. Mater.* **2014**, *13*, 63.
(52) Hill, I. G.; Kahn, A.; Soos, Z. G.; Pascal, J. R. A. *Chem. Phys. Lett.* **2000**, *327*, 181.
(53) Pensack, R. D.; Asbury, J. B. *J. Am. Chem. Soc.* **2009**, *131*, 15986.
(54) Deibel, C.; Strobel, T.; Dyakonov, V. *Phys. Rev. Lett.* **2009**, *103*, 036402.
(55) Durrant, J. R. *Phil. Trans. R. Soc. A* **2013**, *371*.
(56) Murthy, D. H. K.; Gao, M.; Vermeulen, M. J. W.; Siebbeles, L. D. A.; Savenije, T. J. *J. Phys. Chem. C* **2012**, *116*, 9214.
(57) Jeong, K. S.; Pensack, R. D.; Asbury, J. B. *Acc. Chem. Res.* **2013**, *46*, 1538.

CHAPTER 7

NON-COVALENT INTERACTIONS AND CHARGE PENETRATION IN LINEAR OLIGOACENE DIMERS

7.1 Introduction

The molecules in organic molecular crystals such as sexithienyl or the oligoacenes (*e.g.*, naphthalene and pentacene), interact through weak van der Waals forces.[1] Functionalization of such molecules, as discussed in Chapters 4 and 5, can greatly impact the non-bonding interactions in the bulk materials, resulting in changes in packing and materials properties; the latter can vary through increase/decrease in π-conjugation, introduction of dipole moments, or modulation in the sign or magnitude of multipole moments.[2,3] We note that non-covalent interactions also play crucial roles in supramolecular chemistry where they determine the structure of, for instance, DNA and proteins, and are responsible for processes such as molecular recognition and intercalation. [4-14] Because of their importance, a fundamental understanding of the non-covalent interactions in organic materials is a key step for a more complete understanding of such weakly bound systems.

Wheeler, Sherrill, and others have shown that a simple electrostatic picture is not enough to accurately describe these systems, where dispersion effects dominate the interactions and charge penetration is significant at typical intermolecular separations.[10,15-25] Without the inclusion of these additional terms, force fields using atom-centered charge models and semi-empirical models, where only electrostatic interactions are considered for the environment of a given molecules, are of limited use to accurately describe the complex interactions in non-covalently bound systems.

At the electronic-structure level, the evaluation of non-covalent systems is often limited to methods that utilize empirical dispersion terms such as B3LYP-D[26] or computationally expensive methods such as CCSD(T).[27] Empirical dispersion corrections such as Grimme's D2 or D3 corrections,[28,29] including terms to model dispersion as C_6 / R^6 and C_8 / R^8, have been shown to underestimate the dispersion contribution by some 40% compared to wave function-based methods;[20] on the other hand, highly accurate methods such as CCSD(T) are limited to system sizes of a few tens of atoms due to unfavorable scaling, $O\left(n^7\right)$. Because of these limitations, intermediate methods are often used, such as spin-component scaled MP2 (SCS-MP2);[30,31] SCS-MP2 interaction energies have shown good agreement with CCSD(T) interaction energies (within less than 0.2 kcal/mol error);[32] note that SCS-MP2 is parameterized using CCSD(T) reaction energies fit to a test set.

Each of the above methods utilizes a supramolecular approach where the interaction energy is the difference between the energy of the dimer or complex consisting of two molecules and the energies of the isolated molecules. This method, though, is analogous to determining the weight of a person by taking the difference in the weight of a cruise ship with and without the person, *i.e.*, the subtraction of two very large values to obtain a relatively small value where the error associated with the large values can be greater than the desired value. To avoid this issue, the interaction energy can also be treated as a perturbation to the Hamiltonian of the individual monomers. Perhaps the most widespread perturbative approach is symmetry-adapted perturbation theory (SAPT),[33] which has the additional advantage compared to supramolecular approaches of allowing for a decomposition of the interaction energy into physically meaningful components: exchange, dispersion, permanent electrostatics, and induction; each of these terms have been discussed in more detail in Chapter 2. Note that there exist other energy decomposition analysis schemes, such as that derived by Morokuma[34,35] and applied to SCS-MP2 interaction energies by Grimme.[36]

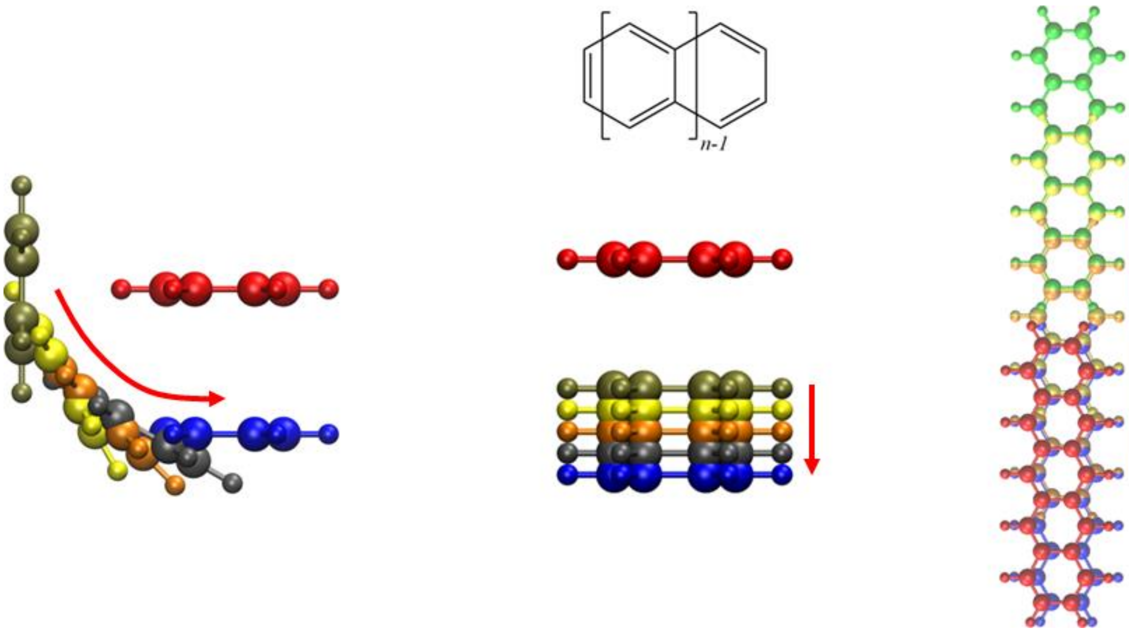

Figure 7.1. (Top middle) Chemical structure of linear oligoacenes where *n* is the number of fused rings, *i.e.*, *n*=1 for benzene and *n*=5 for pentacene. (Bottom left) Ball-and-stick representation of pentacene as a function of dimer angle. Ball-and-stick representations of pentacene displaying increasing dimer separation (bottom center) and long-axis translation (bottom right) as the second monomer moves from an eclipsed configuration to no-overlap. Note one monomer has been offset for clarity.

There have been numerous investigations that explore the non-covalent interactions in linear oligoacenes.[9,18,25,33,37-45] However, these investigations have focused on a few representative dimer configurations (see Figure 7.2); to the best of our knowledge, there have been no previous studies of the potential energy surfaces of these systems to determine how the non-covalent interactions change upon variations in dimer configurations and as a function of acene length. It is also important to note that as acene length increases the crystalline packing changes, which is indicative of changes in the non-covalent interactions; these differences are discussed in more detail below.

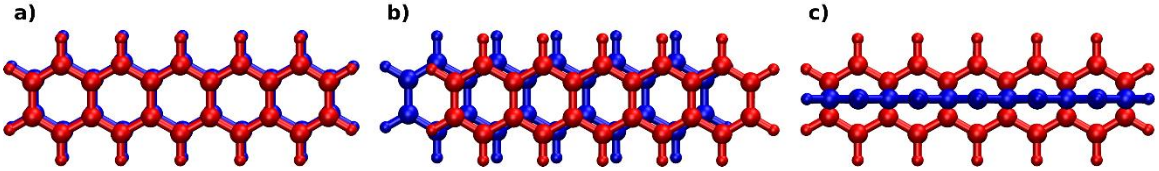

Figure 7.2. (a) Illustration of: an eclipsed configuration; (b) a parallel-displaced configuration; and (c) a T-shaped configuration of the pentacene dimer.

By applying SAPT to dimers of benzene, naphthalene, anthracene, tetracene, pentacene, and hexacene, we explore the influence of acene length on the non-covalent interactions of the oligoacenes and make connections with the preferred crystal packing configurations. For each of the dimer systems, we consider three dimer transformations: (i) dimer angle, where we vary the dimers from a co-facial arrangement to a T-shaped configuration; (ii) separation, where we vary the separation distance from 2.8 Å to 5.0

Å;[46] and (iii) translation, where the dimer is moved along its long-axis from an eclipsed configuration to one of no molecular overlap. In agreement with previous reports, we see that parallel-displaced dimers are more strongly interacting, *i.e*., have a lower energy configuration, than T-shaped dimers, with the interaction energy increasing non-linearly as acene length increases. Compared to dimers extracted from crystal structures, both the lowest-energy parallel-displaced and T-shaped dimers have larger interaction energy. Lastly, we examine the charge penetration contribution to the interaction energy as a function of acene length. The stabilizing charge penetration interaction is due to the electron-nuclear attraction due to the reduced screening of the nuclei of one monomer by its electrons as the electron clouds of the two monomers overlap. We observe that the charge penetration increases linearly with acene length and becomes significant at increasing distances for longer acenes.

7.2 Computational Methodology

All SAPT calculations were completed at the SAPT0/jun-cc-pvdz level (simplified throughout as SAPT0) as implemented in the PSI4 program.[47] This level of calculation has been dubbed the bronze-standard by Parker *et al*.[48] as it allows for accurate calculations of interaction energies (mean absolute error of 0.49 kcal/mol for the S22 test set) in reasonable computational times; which is necessary given the large number of configurations considered. All distributed multipole analysis (DMA) calculations were carried out at the HF/6-311G(d,p) level as implemented in the Molpro software suite.[49] The DMA data were then used to calculate multipole-multipole interaction energies through the 32-pole using a custom script based on the equations of Stone.[50] The geometries of the crystal dimers were taken from the experimentally determined structures as reported in the Cambridge Structural Database: benzene (BENZEN15),[51] naphthalene (NAPHTA06),[52] anthracene (ANTCEN09),[53] tetracene (TETCEN01),[54] and pentacene (PENCEN04).[55] The dimer geometry of crystalline hexacene was extracted from the recently reported crystal structure in Ref. 56.

The geometries of isolated molecules of benzene, naphthalene, anthracene, tetracene, pentacene, and hexacene were optimized at the MP2/6-31+G(d,p) level as implemented in the Gaussian 09 Rev. B.01 software suite.[57] Note that, for pentacene and hexacene, the enforcement of D_{2h} symmetry was required to obtain minimized geometries.

Dimers for SAPT analysis were then created by duplicating the optimized single molecules, followed by a series of transformations using a custom script. The following dimer transformations are considered:

- Separation distance was varied in 0.1 Å increments from 2.8 Å to 5.0 Å.
- Translation along the long-axis of the molecule, from perfectly eclipsed to no molecular overlap in either 0.1 Å or 1.0 Å increments, as discussed below (from 0.0 Å to 17.0 Å for hexacene).
- Dimer angle was varied from 0° (co-facial) to 90°(T-shaped) in 10° increments, except for the inclusion of a 45° dimer.
- All possible combinations of the above dimer configurations are considered.

This strategy allows for the creation of a multidimensional potential energy surface which may then be separated according to individual transformations or combinations of transformations. For each of the dimer configurations that have been considered, both the SAPT0 interaction energy and multipole electrostatic interaction energy have been calculated.

As the DMA interaction between molecules is assumed to be a complete description of the electrostatic term in which only the charge penetration is neglected, the charge penetration contribution to the interaction energy is calculated as the difference between the SAPT0 electrostatic interaction energy and the DMA electrostatic interaction energy. Note that there is some small error associated with this procedure due to the DMA truncation at the 32-pole and the difference in basis sets. The charge penetration contribution has been calculated only along the separation coordinate as this is where its impact should be most pronounced.

7.3 Results and Discussion

7.3.1 Interaction Energies of Crystal Geometry Dimers

To provide a baseline for comparison, we first examine the non-covalent interactions in dimers extracted from the experimentally determined crystal structures (Table 7.1); for asymmetric unit cells, *i.e.*, tetracene, pentacene, and hexacene, the dimer is composed of both molecules of the unit cell. Unsurprisingly, we observe that the interaction energy increases as the acene length increases, by ~220% from benzene to naphthalene and by ~20% from pentacene to hexacene, see Table 7.1. The largest contribution to the interaction energy is dispersion, whose contribution is about 50% larger and of opposite sign as the exchange contribution, and generally displays the largest relative increase as the number of fused rings is increased. While their contributions are smaller, the electrostatic and induction contributions also rapidly increase as acene length increases, with individual contributions being of the same order-of-magnitude and often larger than the difference between the exchange and dispersion contributions, highlighting the importance of these terms to the overall interaction energy.

As stated earlier, the crystalline packing changes as the acene length increases. For benzene, the dimer configuration is more similar to that of an ideal T-shaped dimer with the edge of one of the molecules oriented towards the face of the other and displaying an angle of about 83°. For the other acenes, the picture is not as simple since naphthalene and anthracene possess a rotation in the plane of the backbone of one molecule such that the long-axes of the two molecules are not parallel. Also, the angle between the other acenes is reduced further from the idealized 90° for a T-shaped dimer to between 50° and 53°. This range of configurations necessitates that a large space must be sampled to fully understand how non-covalent interactions determine the crystalline packing morphologies.

Table 7.1. SAPT0/jun-cc-pvdz energy decomposition analysis components of oligoacene dimers extracted from their experimentally determined crystal structures. All units in kcal/mol.

(kcal/mol)	*Total SAPT0*	*Electrostatics*	*Exchange*	*Induction*	*Dispersion*
Benzene	-2.41	-1.19	1.85	-0.25	-2.81
Naphthalene	-5.35	-2.53	5.06	-0.67	-7.21
Anthracene	-8.50	-3.69	7.58	-1.02	-11.36
Tetracene	-12.08	-4.06	8.78	-1.24	-15.57
Pentacene	-16.95	-6.43	14.06	-2.03	-21.89
Hexacene	-20.43	-6.91	15.25	-2.18	-26.59

7.3.2 Evolution of the Intermolecular Interactions upon Dimer Transformation

We now turn to the dimer configurations that are the primary interest of this investigation. Previously, the benzene through tetracene cases have been considered by Grimme[36] who attempted to determine if “special” π-π interactions are present in stacked aromatic complexes that are not present in saturated hydrocarbons; the benzene through pentacene cases were considered by Sherrill[20] in an application of density fitting to SAPT and to further investigate π-π interactions. Both of these studies, though, focused on only a few possible dimer configurations, *i.e.*, ideal T-shaped, eclipsed, or parallel-displaced (Figure 7.2). As noted above, the packing in the solid state is much more complex than these idealized configurations and it is of interest to understand what drives the preferred packing orientations. In order to provide a more complete picture, we investigate here: (i) three each odd- (benzene, anthracene, pentacene) and even-numbered (naphthalene, tetracene, hexacene) ring systems to discern if odd-even effects are present; and (ii) a very large number of configurations, extending into the thousands.

Before looking at trends upon specific transformations, it is important to determine the lowest energy structures for both co-facial and T-shaped arrangements for comparison to prior investigations, see Table 7.2. Note that the dimer configurations are not equivalent for each system: *e.g.*, co-facial benzene prefers a 3.5 Å interplanar separation with a 1.7 Å long-axis translation, while the pentacene planes are separated by 3.4 Å with a 1.0 Å translation; a comparison of dimers in equivalent arrangements will be made later in this Chapter.

For each of the acene systems, we find that the co-facial arrangement is preferred over the T-shaped configuration and that the interaction energy difference between co-facial and T-shaped increases non-linearly with acene length. The primary contributions to the energy difference between the configurations is the dispersion interaction, which is larger for the co-facial dimers, due to the increased degree of interaction of the π-clouds, and the electrostatic component, with both providing approximately equal contributions. The electrostatic contribution is perhaps the more interesting to consider since there is a qualitative difference between the multipole-only-based electrostatic interaction and the SAPT0-determined electrostatic interaction for the co-facial arrangement. This is due mainly to charge overlap, resulting from the overlap of the π-clouds at relatively small intermolecular separations. Also, note that as the number of fused rings increases, the DMA electrostatic energy increases by a relatively small amount (0.5 kcal/mol/ring) compared to the SAPT0 electrostatic energy (1.5 – 2.0 kcal/mol/ring), again being due to the large contribution of charge penetration at short intermolecular distances; this will be discussed in more detail in Section 7.3.3.

Table 7.2. SAPT0/jun-cc-pvdz energy components and DMA electrostatic interaction energies of the lowest-energy oligoacene dimers in co-facial (0°) and T-shaped (90°) arrangements. E_{SAPT0} is the total SAPT0 interaction energy; E_{elect}, E_{exch}, E_{ind}, and E_{disp} are the electrostatic, exchange, induction, and dispersion contributions, respectively, and E_{dma} is the multipole-multipole electrostatic interaction energy. All units in kcal/mol.

(kcal/mol)	E_{SAPT0}	E_{elect}	E_{exch}	E_{ind}	E_{disp}	E_{dma}
			Co-facial			
Benzene*	-2.820	-1.647	6.278	-0.729	-6.723	1.335
Naphthalene*	-7.419	-3.418	11.707	-1.146	-14.563	2.044
Anthracene*	-12.639	-5.178	17.370	-1.560	-23.272	2.727
Tetracene	-18.075	-10.502	33.468	-2.930	-38.111	4.465
Pentacene	-24.092	-13.001	40.950	-3.651	-48.390	5.278
Hexacene	-30.359	-15.555	48.518	-4.409	-58.913	6.090

	T-shaped					
Benzene*	-2.816	-1.795	3.294	-0.528	-3.787	-0.666
Naphthalene*	-5.880	-3.348	6.818	-1.045	-8.305	-1.145
Anthracene*	-9.249	-4.827	10.310	-1.548	-13.184	-1.548
Tetracene	-12.669	-7.432	17.273	-2.461	-20.048	-1.926
Pentacene	-16.305	-9.266	21.947	-3.130	-25.857	-2.300
Hexacene	-20.112	-9.822	22.605	-3.354	-29.541	-2.715

*Configurations obtained from Refs. 20,58 whose interaction energy was lower than those obtained from configuration scans. Geometries were intermediate from those explored in configuration scans.

We have also examined how the potential-energy surfaces of different dimers change under specific transformations. First, we considered the case where only the separation distance is changed. As expected, the interaction energy falls quickly as the separation distance increases beyond *ca.* 3.5 Å.[59] The electrostatics term falls off the quickest,[60] followed by exchange and then dispersion. Dispersion dominates the interaction energy at separations greater than 4.5 Å for co-facial arrangements and greater than 4.0 Å for T-shaped dimers. The slower fall-off of the dispersion for co-facial dimers may be attributed to the large interaction of the π-clouds, and while exchange and charge penetration also depend on π-cloud interactions, their contribution falls off exponentially as distance increases, *i.e.*, much faster than dispersion, which evolves as $1/R^6 + 1/R^8 + 1/R^{10} + \ldots$.

If we begin with dimers that are in an eclipsed, co-facial configuration (no long-axis translation), at 45°, and at 90° (T-shaped) followed by a separation of the dimers we can observe a combination of the angle and length dependence, see Figure 7.3. The 45° dimer is the least stable configuration for each of the acenes, and has its lowest energy configuration at an increased separation (3.8 Å) than either the eclipsed or T-shaped orientations, thus limiting the stabilization due to charge penetration. Furthermore, as the acene length increases, the strongest interacting configuration changes. For example, for benzene, the T-shaped dimer is the most stable, with the curves for the 45° and eclipsed dimers being approximately equal. As the number of fused rings is increased to anthracene, the eclipsed dimer curve becomes intermediate of the 45° and 90° dimers. Finally, for pentacene the eclipsed curve is slightly more stable than the 90° dimer, due to a combination of dispersion and electrostatics.

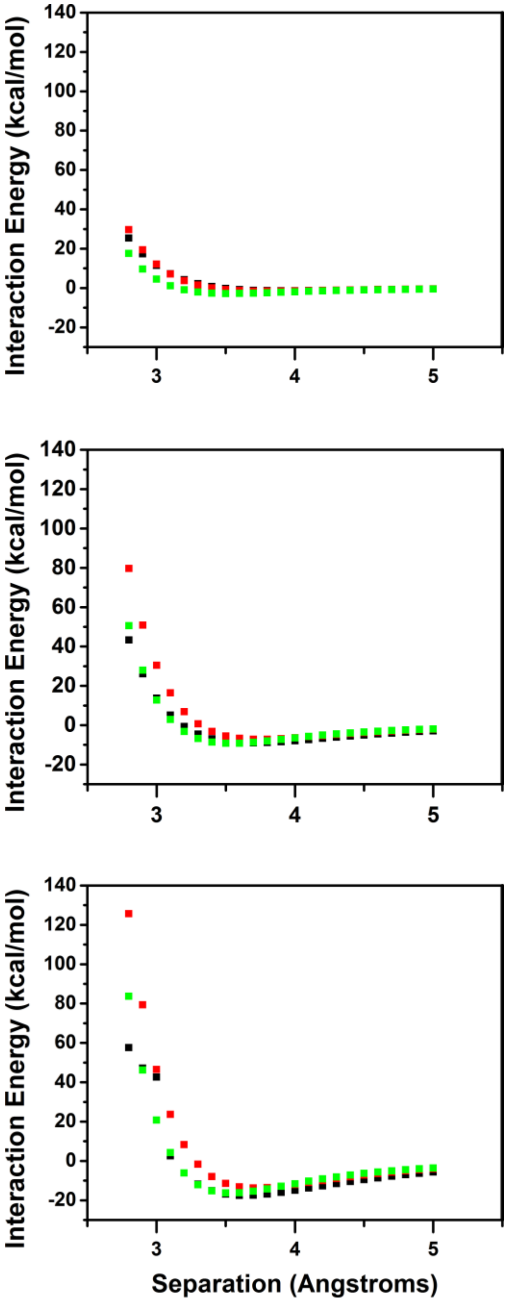

Figure 7.3. Total SAPT0 interaction energy for benzene (top), anthracene (center), and pentacene (bottom) as the separation distance is varied from 2.8 Å to 5.0 Å in 0.1 Å increments for dimers with no long-axis translation in co-facial (0°; black), 45° (red), and T-shaped (90°; green) arrangements.

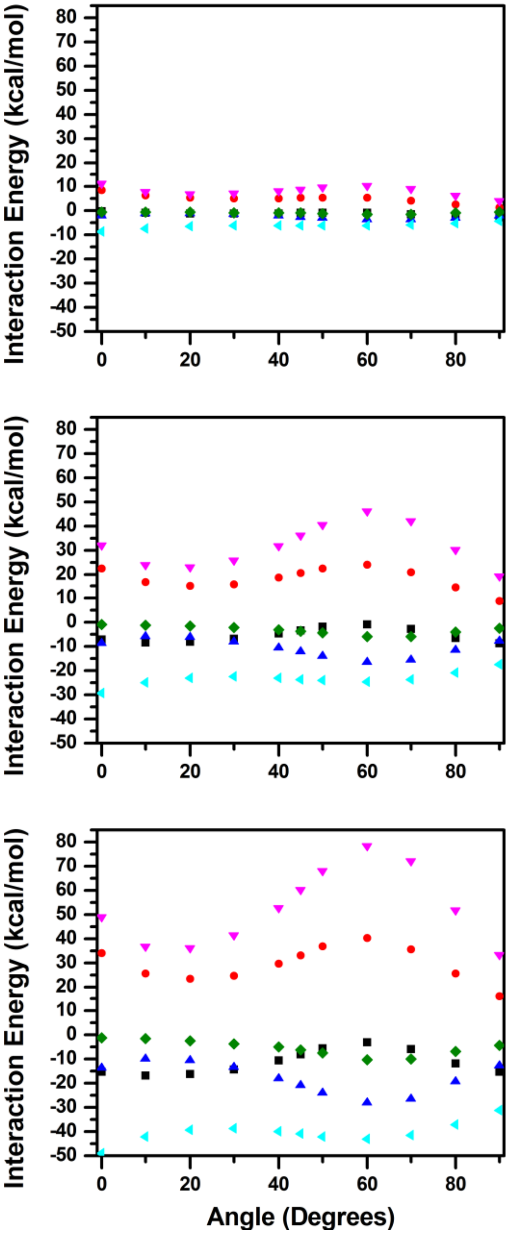

Figure 7.4. SAPT energy components for benzene (top), anthracene (center), and pentacene (bottom) at a separation distance of 3.5 Å , 3.4 Å, and 3.4 Å, respectively, with no long-axis translation as the angle between the molecules is changed from co-facial (0°) to T-shaped (90°). Energy components are: total SAPT0 energy (■; black), HF energy (●; red), SAPT0 electrostatics (▲; blue), SAPT0 exchange (▼; magenta), SAPT0 induction (♦; green), and SAPT0 dispersion (◀; cyan).

From Figure 7.4, we observe that the potential-energy surfaces of benzene, anthracene, and pentacene, as the angle between the dimers is changed, are qualitatively identical although the scales are different. For all of the systems, the evolution of E_{SAPT0} follows qualitatively those of exchange and electrostatics with minima at about 20° and 90° and a maximum at about 60° (*i.e.*, exchange is more repulsive when electrostatics are more attractive). Here, electrostatics are dominated by charge penetration at the separations considered; thus, both exchange and electrostatics are dependent on the extent of orbital overlap with their contributions being of opposite sign.

It is interesting to note that the angles taken from the crystal structures (~50° - ~83°) lie near the maximum of E_{SAPT0}; these results suggest that these configurations should be less stable than other arrangements. That it is not the case underlines that there must be some interactions that are important in the bulk material that are not accounted for in two-body SAPT0, such as non-additive three-body interactions. In benzene trimers, the three-body dispersion correction has been estimated to be in the range of 0.76 kcal/mol to 1.67 kcal/mol, a significant contribution.[13,61-63] Indeed Szakewicz has recently proposed a model to predict crystal packing that requires the inclusion of such three-body terms.[21]

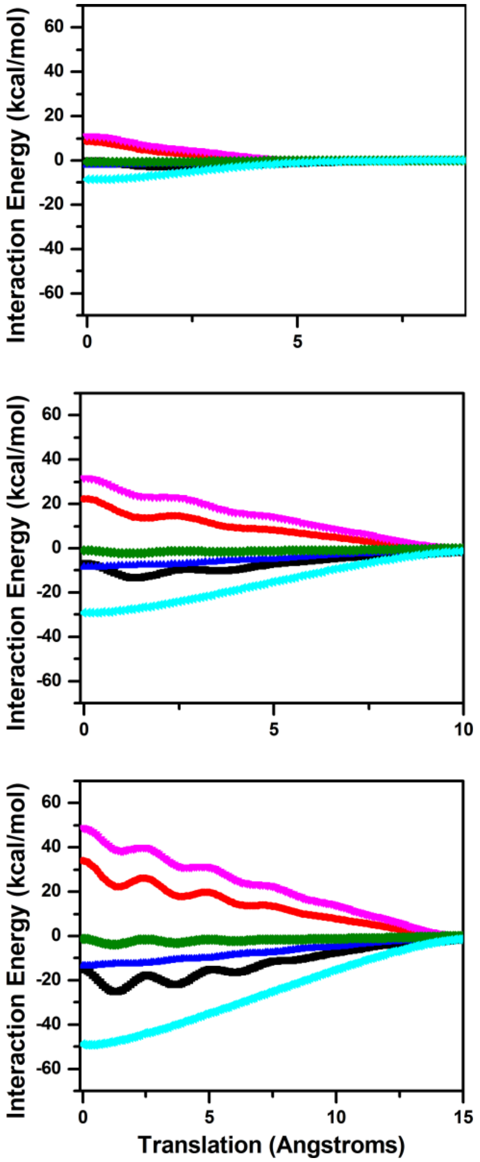

Figure 7.5. SAPT energy components for benzene (top), anthracene (center), and pentacene (bottom) at a separation distance of 3.5 Å , 3.4 Å, and 3.4 Å, respectively, in a co-facial arrangement as the long-axis translation is varied from 0.0 Å to no molecular overlap in 0.1 Å increments. Energy components are: total SAPT0 energy (■; black), HF energy (●; red), SAPT0 electrostatics (▲; blue), SAPT0 exchange (▼; magenta), SAPT0 induction (♦; green), and SAPT0 dispersion (◄; cyan).

More interesting trends present themselves when we consider co-facial or T-shaped dimers at a fixed separation and displace one molecule of each dimer along the long-axis. For each of the co-facial dimers, E_{SAPT0}, E_{exch}, and E_{ind} fluctuate with the number of maxima and minima corresponding to the number of fused rings (*i.e.*, one maximum/minimum for benzene and five maxima/minima for pentacene), while E_{elect} displays maxima and minima opposite the other contributions. The minima in total energy correspond to a staggered arrangement, where bridging carbon-carbon bonds are above the rings of the adjacent molecule. Similar trends are observed for the T-shaped dimers, although the energy difference between the maxima and minima are larger. This is due to the close contacts that occur when the peripheral hydrogen are pointed towards the bridging carbon-carbon bonds.

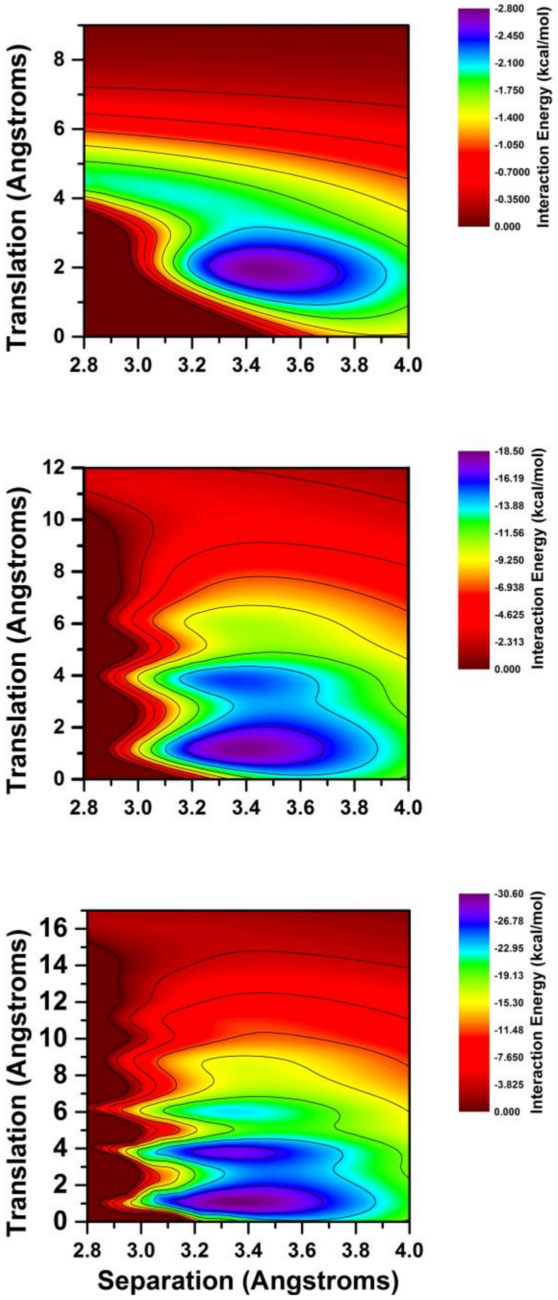

Figure 7.6. Contour plots of the total SAPT0 interaction energies for benzene (top), tetracene (center), and hexacene (bottom) for co-facial configurations as the separation distance and long-axis translation are varied. Note that the color scales have been adjusted for each plot so that qualitative differences are easier to distinguish.

Lastly, we examine co-facial dimers under combined changes of separation distance and long-axis translation, see Figure 7.6. Contour plots provide additional detail that is not otherwise readily apparent with traditional 2-dimensional plots, allowing for the extraction of information that might otherwise be missed. From Figure 7.6, we find that the potential-energy surfaces are indeed complex, with structures that are relatively stable at small intermolecular distances. For example, there is a stable benzene dimer (-1.79 kcal/mol) with only 2.8 Å of separation when one molecule is displaced by 5 Å, at which distance the aromatic rings are no longer spatially overlapping but are still strongly interacting. In this configuration, the electrostatic component is strongly stabilizing (-1.18 kcal/mol), while the exchange (1.81 kcal/mol) and dispersion (-2.22 kcal/mol) terms nearly negate each other. Additionally, as the acene size increases to tetracene, there is the formation of a secondary well with the lowest point in the well possessing a separation distance of 3.3 Å. For tetracene, there also appears to be a third well forming at a long-axis displacement of 6.0 Å. This becomes more apparent in hexacene, and again another stable configuration at about 8.0 Å of long-axis translation. For each of these situations, the low energy structures correspond to staggered co-facial arrangements where the bridging carbon-carbon bonds of one molecule are interacting with the face of the fused rings on the adjacent molecule.

7.3.3 Charge Penetration Contribution to Non-Bonded Interactions

In a traditional multipole electrostatics picture, implemented in most force fields using multipoles of rank 0 (*i.e.*, charge), the electrostatic interactions in T-shaped dimers of the acenes are largely stabilizing, due to the positive-negative quadrupole interactions. In the co-facial dimers, the electrostatic interactions are destabilizing due to the negative-negative quadrupole interactions, as shown in the last column of Table 7.2. However, CCSD(T) and SAPT calculations indicate that the co-facial dimer is more stabilizing,[37] which represents a qualitative discrepancy. From previous energy decomposition analysis studies[30] and SAPT calculations,[20] as well as has been shown here, the E_{elect} component of the non-bonded interactions is more stabilizing in the co-facial configurations than in the corresponding T-shaped dimers, which is due to charge penetration.

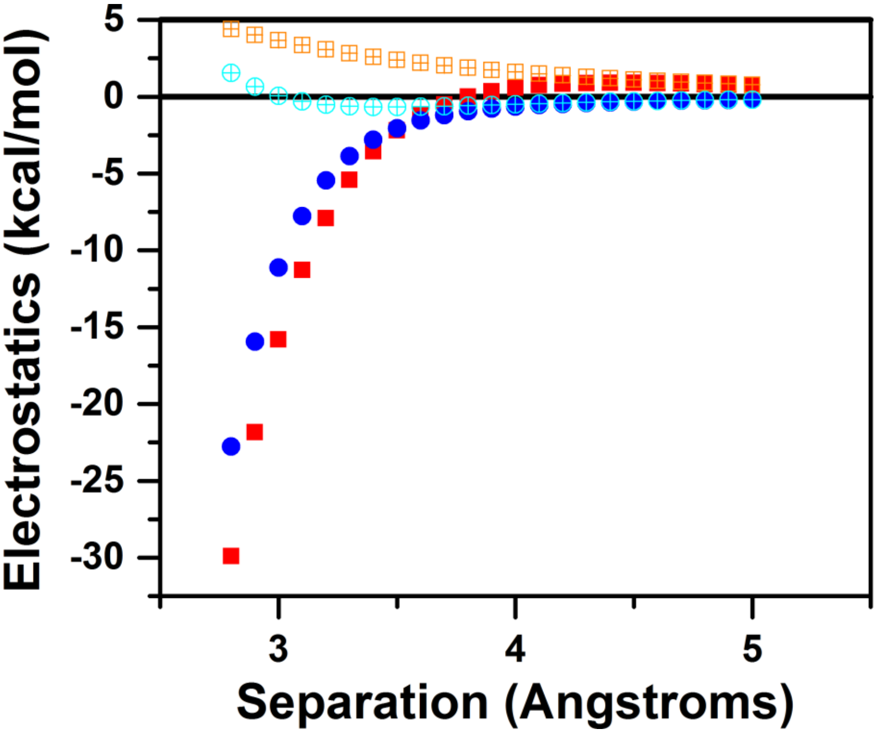

Figure 7.7. Electrostatic interaction energy in benzene co-facial (■; blue, cyan) and T-shaped (●; red, orange) dimers, as calculated at the SAPT0 (solid) and DMA electrostatic (crossed) levels as a function of separation distance.

As the electron clouds of two monomers begin to overlap at small intermolecular distances, the multipole picture breaks down. This comes from the fact that in such instances there is a reduction of the screening of the nucleus in one monomer by its electron distribution. Thus, there appears an attractive electron-nuclear interaction that increases rapidly as the overlap further increases; at the same time E_{exch} also increases rapidly and eventually overwhelms any stabilization due to charge penetration. This breakdown of the multipole approximation and the importance of charge penetration in benzene dimers are highlighted in Figure 7.7. At large separation distance, *i.e.*, greater than 4 Å, the charge penetration contribution is negligible and the electrostatic contribution in the co-facial configuration is repulsive, which agrees very well with the multipole approximation. At separations shorter than 4 Å, the charge penetration is important, with the SAPT electrostatic contribution becoming strongly stabilizing in both dimer configurations, although more so for the co-facial case; this results in a qualitative difference between the multipole approximation and the SAPT electrostatics, as has been highlighted previously by Sherrill and co-workers.[41]

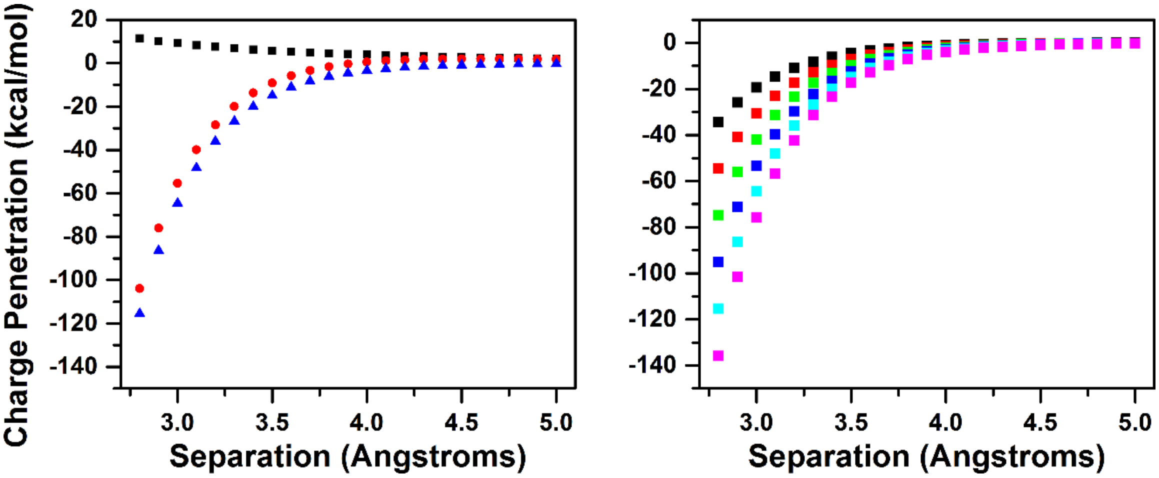

Figure 7.8. (Left) Total SAPT0 interaction energy (●; red) and DMA electrostatic interactions energy (■; black) for pentacene in a co-facial configuration with no long-axis translation, as the separation distance changes in 0.1 Å increments from 2.8 Å to 5.0 Å. The charge penetration contribution (▲; blue) is defined as the difference between the SAPT0 and DMA electrostatic energies. (Right) Charge penetration contributions for benzene (black), naphthalene (red), anthracene (green), tetracene (blue), pentacene (cyan), and hexacene (magenta) for co-facial dimers as a function of separation distance.

In order to quantify the charge penetration contribution in the oligoacene dimers, we calculated the DMA multipole electrostatic interaction energy and the SAPT0 electrostatic interaction energy for each of the acene configurations considered in Section 7.4. We calculated the multipole interaction energy through the 5th rank, *e.g.*, charge–32-pole or octopole-quadrupole, to provide increased accuracy. Thus, the only difference between the SAPT0 electrostatic energy and the multipole electrostatic energy should be the contribution from charge penetration. In Figure 7.8, the difference between the multipole electrostatics and SAPT0 electrostatics is plotted for pentacene, with the resulting charge penetration contribution being more stabilizing than the SAPT0 electrostatics term itself; this result is due to the multipole interaction being destabilizing at smaller distances. For each of the lowest energy co-facial dimer configurations, the charge penetration contribution is calculated to be of the same size as the total SAPT0 interaction energy, which underlines the importance of this contribution (Table 7.3). It is interesting to note that for each system, the charge penetration turns on (greater than 1 kcal/mol) at a different point (4.0 Å for co-facial benzene and 4.4Å for co-facial pentacene) while E_{exch} begins to dominate at about 3.2 Å, resulting in a rapid decrease of the interaction energy.

We can further compare the charge penetration contribution for co-facial and T-shaped dimers in their respective lowest energy configurations, and the charge penetration contribution in the experimental crystalline dimers, see Figure 7.9. For each set of systems, there is a linear increase in the charge penetration contribution as the acene length increases, with the amount of increase dependent on the dimer configurations. As one would expect because of the larger π-π overlap, the co-facial dimers present the largest charge penetration contribution; the T-shaped dimers also present a large charge penetration energy, due to the peripheral hydrogen atoms interacting with the face of the adjacent molecule. Lastly, the charge penetration contribution in the experimental crystal dimers is much smaller than for either model configuration. This is due to the rotation in the plane of the backbone in the smaller acenes and a displacement along the short-axis of one of the molecules in the larger acenes. Nevertheless, the charge penetration energy in the experimental systems still accounts for between 20% - 50% of the total interaction energy.

Table 7.3. SAPT0 interaction energies, DMA interaction energies, and charge penetration contribution in the most stable co-facial oligoacene dimers. All values in kcal/mol.

(kcal/mol)	E_{SAPT0}	E_{DMA}	E_{chp}
Benzene	-2.820	1.335	-6.15
Naphthalene	-7.419	2.044	-9.61
Anthracene	-12.639	2.727	-13.07
Tetracene	-18.075	4.465	-16.51
Pentacene	-24.092	5.278	-19.96
Hexacene	-30.359	6.090	-23.47

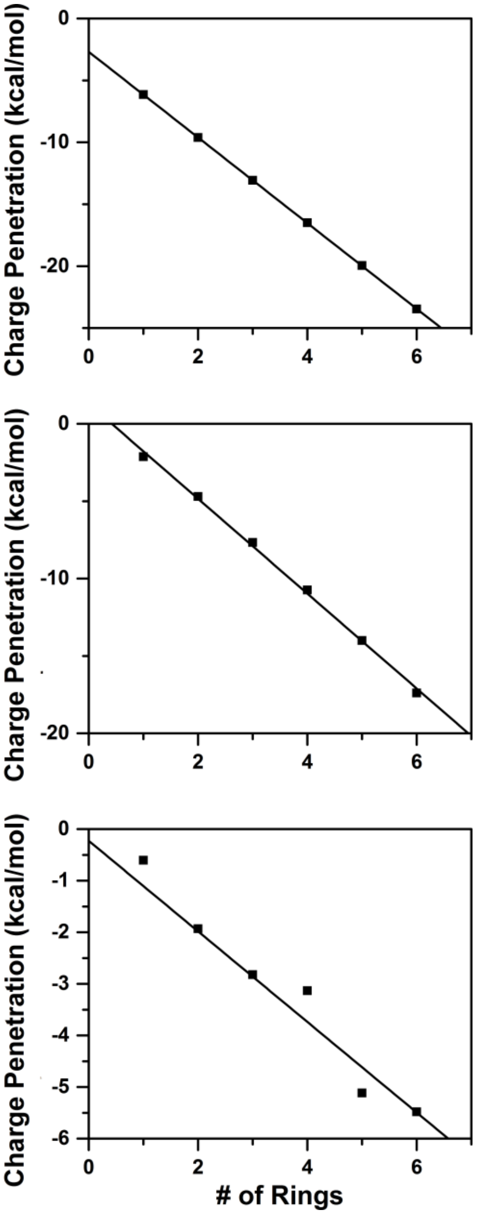

Figure 7.9. Evolution of the charge penetration contribution in the linear oligoacenes as a function of the number of fused rings for lowest energy co-facial dimers (top), lowest energy T-shaped dimers (center), and dimer configurations extracted from the experimental unit cells (bottom).

7.4 Conclusions

The potential energy surfaces of interacting oligoacenes are complex, with the stabilizing charge penetration being nearly equivalent to the total interaction energy. This interaction, often neglected, is necessary to obtain accurate descriptions of intermolecular interactions. We applied wave function-based SAPT and DMA electrostatics to the study of dimers of benzene through hexacene, to create potential energy surfaces under three transformations: (i) angle, (ii) separation, and (iii) long-axis translation. We observe that the lowest-energy model dimers present a parallel displaced arrangement. In each instance, this configuration is significantly more stable than the configuration found in the experimental crystal structures; these results point out that additional interactions outside of those accessible from a dimer model are needed to accurately describe and eventually predict the bulk packing.[21] Under the three transformations, we observe qualitatively identical behavior for both angle and separation transformations as acene length is increased, with the primary difference being one of scale. When long-axis translation is applied to the model systems, there appear a series of peaks and valleys that correspond to the number of fused rings in each acene molecule, When we combine transformations, it is found that, as acene length increases, smaller separation distances become preferred. For all of the acene systems, we observe that E_{elect}, E_{exch}, and E_{ind} have a linear dependence on acene length while E_{disp} and thus E_{SAPT0} have a non-linear dependence.

We then explored the charge penetration stabilization that occurs as electron densities overlap at short distance. First, we demonstrated the breakdown of the multipole approximation at separation distances shorter than 4 Å, noting that this evolution is not restricted to co-facial systems but also occurs for the T-shaped dimers. We then quantified this contribution to the intermolecular interaction energy; we showed that, for both the model systems and the dimers extracted from experimental data, the charge penetration is a stabilizing force of similar size to the total interaction energy. This confirms that for an accurate prediction of the interaction between molecules, proper account of the charge penetration and three-body interactions must be made.

7.5 References

(1) Pope, M.; Swenberg, C. E. *Electronic Processes in Organic Crystals and Polymers*, 1999.

(2) McGarry, K. A.; Xie, W.; Sutton, C.; Risko, C.; Wu, Y.; Young, V. G.; Brédas, J.-L.; Frisbie, C. D.; Douglas, C. J. *Chem. Mater.* **2013**, *25*, 2254.

(3) Ryno, S. M.; Lee, S. R.; Sears, J.; Risko, C.; Bredas, J. L. *J. Phys. Chem. C* **2013**, *117*, 13853.

(4) Hohenstein, E. G.; Parrish, R. M.; Sherrill, C. D.; Turney, J. M.; Schaefer, H. F. *J. Chem. Phys.* **2011**, *135*, 174107.

(5) Li, S.; Cooper, V. R.; Thonhauser, T.; Lundqvist, B. I.; Langreth, D. C. *J. Phys. Chem. B* **2009**, *113*, 11166.

(6) Jurecka, P.; Sponer, J.; Cerny, J.; Hobza, P. *Phys. Chem. Chem. Phys.* **2006**, *8*, 1985.

(7) Jurečka, P.; Hobza, P. *J. Am. Chem. Soc.* **2003**, *125*, 15608.

(8) Elstner, M.; Hobza, P.; Frauenheim, T.; Suhai, S.; Kaxiras, E. *J. Chem. Phys.* **2001**, *114*, 5149.

(9) Ringer, A. L.; Figgs, M. S.; Sinnokrot, M. O.; Sherrill, C. D. *J. Phys. Chem. A* **2006**, *110*, 10822.

(10) Ringer, A. L.; Sherrill, C. D. *Chem. Eur. J.* **2008**, *14*, 2542.

(11) Ringer, A. L.; Senenko, A.; Sherrill, C. D. *Protein Sci.* **2007**, *16*, 2216.

(12) Podeszwa, R.; Rice, B. M.; Szalewicz, K. *Phys. Chem. Chem. Phys.* **2009**, *11*, 5512.

(13) Podeszwa, R.; Rice, B. M.; Szalewicz, K. *Phys. Rev. Lett.* **2008**, *101*, 115503.

(14) Collings, J. C.; Roscoe, K. P.; Robins, E. G.; Batsanov, A. S.; Stimson, L. M.; Howard, J. A. K.; Clark, S. J.; Marder, T. B. *New J. Chem.* **2002**, *26*, 1740.

(15) Sherrill, C. D.; Sumpter, B. G.; Sinnokrot, M. O.; Marshall, M. S.; Hohenstein, E. G.; Walker, R. C.; Gould, I. R. *J. Comput. Chem.* **2009**, *30*, 2187.

(16) Wang, B.; Truhlar, D. G. *J. Chem. Theory Comput.* **2010**, *6*, 3330.

(17) Freitag, M. A.; Gordon, M. S.; Jensen, J. H.; Stevens, W. J. *J. Chem. Phys.* **2000**, *112*, 7300.

(18) Arnstein, S. A.; Sherrill, C. D. *Phys. Chem. Chem. Phys.* **2008**, *10*, 2646.

(19) Geng, Y.; Takatani, T.; Hohenstein, E. G.; Sherrill, C. D. *J. Phys. Chem. A* **2010**, *114*, 3576.

(20) Hohenstein, E. G.; Sherrill, C. D. *J. Chem. Phys.* **2010**, *132*, 184111.

(21) Szalewicz, K. *Acc. Chem. Res.* **2014**, *47*, 3266.

(22) Sherrill, C. D. *Acc. Chem. Res.* **2013**, *46*, 1020.

(23) Bloom, J. W. G.; Wheeler, S. E. *Angew. Chem., Int. Ed.* **2011**, *50*, 7847.

(24) Wheeler, S. E.; Bloom, J. W. G. *J. Phys. Chem. A* **2014**, *118*, 6133.

(25) Wheeler, S. E.; Bloom, J. W. G. *Chem. Commun. (Cambridge, U. K.)* **2014**, *50*, 11118.

(26) Civalleri, B.; Zicovich-Wilson, C. M.; Valenzano, L.; Ugliengo, P. *Cryst. Eng. Comm.* **2008**, *10*, 405.

(27) Raghavachari, K.; Trucks, G. W.; Pople, J. A.; Head-Gordon, M. *Chem. Phys. Lett.* **1989**, *157*, 479.

(28) Grimme, S. *J. Comput. Chem.* **2006**, *27*, 1787.

(29) Grimme, S.; Antony, J.; Ehrlich, S.; Krieg, H. *J. Chem. Phys.* **2010**, *132*, 154104.

(30) Grimme, S. *J. Chem. Phys.* **2003**, *118*, 9095.

(31) Takatani, T.; Hohenstein, E. G.; Sherrill, C. D. *J. Chem. Phys.* **2008**, *128*, 124111.

(32) Hill, J. G.; Platts, J. A.; Werner, H.-J. *Phys. Chem. Chem. Phys.* **2006**, *8*, 4072.

(33) Jeziorski, B.; Moszynski, R.; Szalewicz, K. *Chem. Rev.* **1994**, *94*, 1887.

(34) Morokuma, K. *J. Chem. Phys.* **1971**, *55*, 1236.

(35) Kitaura, K.; Morokuma, K. *Int. J. Quantum Chem.* **1976**, *10*, 325.

(36) Grimme, S. *Angew. Chem., Int. Ed.* **2008**, *47*, 3430.

(37) Sinnokrot, M. O.; Sherrill, C. D. *J. Phys. Chem. A* **2004**, *108*, 10200.

(38) Sinnokrot, M. O.; Sherrill, C. D. *J. Am. Chem. Soc.* **2004**, *126*, 7690.

(39) Sinnokrot, M. O.; Sherrill, C. D. *J. Phys. Chem. A* **2006**, *110*, 10656.

(40) Marshall, M. S.; Steele, R. P.; Thanthiriwatte, K. S.; Sherrill, C. D. *J. Phys. Chem. A* **2009**, *113*, 13628.

(41) Hohenstein, E. G.; Duan, J.; Sherrill, C. D. *J. Am. Chem. Soc.* **2011**, *133*, 13244.

(42) Wheeler, S. E.; Houk, K. N. *J. Am. Chem. Soc.* **2008**, *130*, 10854.

(43) Wheeler, S. E.; McNeil, A. J.; Müller, P.; Swager, T. M.; Houk, K. N. *J. Am. Chem. Soc.* **2010**, *132*, 3304.

(44) Wheeler, S. E. *Acc. Chem. Res.* **2012**, *46*, 1029.

(45) Podeszwa, R.; Bukowski, R.; Szalewicz, K. *J. Phys. Chem. A* **2006**, *110*, 10345.

(46) The separation distance is defined using a weighted function where, in the co-facial arrangement, the distance is defined as face-to-face and in the T-shaped arrangement the distance is defined as the face-to-hydrogen distance.

(47) Turney, J. M.; Simmonett, A. C.; Parrish, R. M.; Hohenstein, E. G.; Evangelista, F. A.; Fermann, J. T.; Mintz, B. J.; Burns, L. A.; Wilke, J. J.; Abrams, M. L.; Russ, N. J.; Leininger, M. L.; Janssen, C. L.; Seidl, E. T.; Allen, W. D.; Schaefer, H. F.; King, R. A.; Valeev, E. F.; Sherrill, C. D.; Crawford, T. D. *WIREs Comput. Mol. Sci.* **2012**, *2*, 556.

(48) Parker, T. M.; Burns, L. A.; Parrish, R. M.; Ryno, A. G.; Sherrill, C. D. *J. Chem. Phys.* **2014**, *140*, 094106.

(49) Werner, H.-J.; Knowles, P. J.; Knizia, G.; Manby, F. R.; Schütz, M.; Celani, P.; Korona, T.; Lindh, R.; Mitrushenkov, A.; Rauhut, G.; Shamasundar, K. R.; Adler, T. B.; Amos, R. D.; Bernhardsson, A.; Berning, A.; Cooper, D. L.; Deegan, M. J. O.; Dobbyn, A. J.; Eckert, F.; Goll, E.; Hampel, C.; Hesselmann, A.; Hetzer, G.; Hrenar, T.; Jansen, G.; Köppl, C.; Liu, Y.; Lloyd, A. W.; Mata, R. A.; May, A. J.; McNicholas, S. J.; Meyer, W.; Mura, M. E.; Nicklass, A.; O'Neill, D. P.; Palmieri, P.; Peng, D.; Pflüger, K.; Pitzer, R.; Reiher, M.; Shiozaki, T.; Stoll, H.; Stone, A. J.; Tarroni, R.; Thorsteinsson, T.; Wang, M. MOLPRO, version 2012.1, a package of ab initio programs. Published Online: 2012.

(50) Stone, A. J. *The Theory of Intermolecular Forces*; Clarendon Press: Oxford, 1996.

(51) Katrusiak, A.; Podsiadło, M.; Budzianowski, A. *Cryst. Growth Des.* **2010**, *10*, 3461.

(52) Brock, C. P.; Dunitz, J. D. *Acta Crystallogr., Sect. B: Struct. Sci.* **1982**, *38*, 2218.

(53) Brock, C. P.; Dunitz, J. D. *Acta Crystallogr., Sect. B: Struct. Sci.* **1990**, *46*, 795.

(54) Holmes, D.; Kumaraswamy, S.; Matzger, A. J.; Vollhardt, K. P. C. *Chem. Eur. J.* **1999**, *5*, 3399.

(55) Mattheus, C. C.; Dros, A. B.; Baas, J.; Meetsma, A.; Boer, J. L. d.; Palstra, T. T. M. *Acta Crystallogr., Sect. C: Cryst. Struct. Commun.* **2001**, *57*, 939.

(56) Watanabe, M.; Chang, Y. J.; Liu, S.-W.; Chao, T.-H.; Goto, K.; Islam, M. M.; Yuan, C.-H.; Tao, Y.-T.; Shinmyozu, T.; Chow, T. J. *Nature Chem.* **2012**, *4*, 574.

(57) Frisch, M. J.; Trucks, G. W.; Schlegel, H. B.; Scuseria, G. E.; Robb, M. A.; Cheeseman, J. R.; Scalmani, G.; Barone, V.; Mennucci, B.; Petersson, G. A.; Nakatsuji, H.; Caricato, M.; Li, X.; Hratchian, H. P.; Izmaylov, A. F.; Bloino, J.; Zheng, G.; Sonnenberg, J. L.; Hada, M.; Ehara, M.; Toyota, K.; Fukuda, R.; Hasegawa, J.; Ishida, M.; Nakajima, T.; Honda, Y.; Kitao, O.; Nakai, H.; Vreven, T.; Montgomery Jr., J. A.; Peralta, J. E.; Ogliaro, F.; Bearpark, M. J.; Heyd, J.; Brothers, E. N.; Kudin, K. N.; Staroverov, V. N.; Kobayashi, R.; Normand, J.; Raghavachari, K.; Rendell, A. P.; Burant, J. C.; Iyengar, S. S.; Tomasi, J.; Cossi, M.; Rega, N.; Millam, N. J.; Klene, M.; Knox, J. E.; Cross, J. B.; Bakken, V.; Adamo, C.; Jaramillo, J.; Gomperts, R.; Stratmann, R. E.; Yazyev, O.; Austin, A. J.; Cammi, R.; Pomelli, C.; Ochterski, J. W.; Martin, R. L.; Morokuma, K.; Zakrzewski, V. G.; Voth, G. A.; Salvador, P.; Dannenberg, J. J.; Dapprich, S.; Daniels, A. D.; Farkas, Ö.; Foresman, J. B.; Ortiz, J. V.; Cioslowski, J.; Fox, D. J.; Gaussian, Inc.: Wallingford, CT, USA, 2009.

(58) Sherrill, C. D.; Takatani, T.; Hohenstein, E. G. *J. Phys. Chem. A* **2009**, *113*, 10146.

(59) The rate at which the interaction energy decreases will be dependent on the separation distance. At separation distances up to 4 angstroms, there will be exponential decrease as charge penetration will be a large contribution. At larger separations, there will be 1/R^n dependence due to dispersion and various electrostatic multipole interactions.

(60) The distance dependence of the electrostatics terms will be dependent on the rank of the interacting multipoles. The distance dependence takes the form 1/R^(1+L+M) where L and M are the rank of the interacting multipoles, i.e., charge is rank 0, dipole is rank 1, etc.

(61) Kennedy, M. R.; McDonald, A. R.; DePrince, A. E.; Marshall, M. S.; Podeszwa, R.; Sherrill, C. D. *J. Chem. Phys.* **2014**, *140*, 121104.

(62) Anatole von Lilienfeld, O.; Tkatchenko, A. *J. Chem. Phys.* **2010**, *132*, 234109.

(63) Wen, S.; Beran, G. J. O. *J. Chem. Theory Comput.* **2011**, *7*, 3733.

CHAPTER 8

CONCLUSIONS AND OUTLOOK

8.1 Synopsis

Over the past few years, organic electronic devices have undergone significant improvements, with the efficiencies of organic photovoltaics climbing rapidly and organic light-emitting displays becoming commonplace in the consumer market. Fundamental materials studies such as those presented here will allow for the continued advancement of these devices through a more complete understanding of the processes that govern their operation. While the performance of new organic electronic devices is impressive, the transport of charge is still often a limiting step in the device operation. Therefore, a more complete understanding of the processes that impact the rate of charge transport, such as the polarization of the environment due to an excess charge, is necessary in order to engineer ever more efficient devices.

We began by introducing a model for polarization energy based upon a polarizable force field that utilizes atom-centered multipoles instead of atom-centered charges in order to accurately recreate the molecular quadrupole moment in non-dipolar molecules. The polarization within this model is treated using atom-centered induced dipoles with isotropic atomic polarizabilities that are able to recreate the anisotropic molecular polarizability and give an accurate description of the molecular environment, with the electrostatic parameters derived from electronic-structure calculations. First, we applied this model to the linear oligoacenes (*i.e.*, naphthalene, anthracene, tetracene, and pentacene) as a validation step to compare to experimental results and previous theoretical calculations. We show improvement in terms of polarization energy magnitude and polarization energy asymmetry to previous models while quantitatively describing the polarization energy as a function of the linear acene length compared to experimental results.

We then tested the predictive ability of our model by calculating the polarization energy of perfluorinated naphthalene and pentacene; neither of that had been studied experimentally with regards to the polarization energy. The polarization energy asymmetry is reversed for these systems due to the change in sign of the molecular quadrupole components, a result that may be justified without the need for experiment.

With this model, we have introduced a readily accessible method by which the polarization energy of organic molecular crystals may be assessed. This model has already been implemented by other groups in both published work[1] and on-going work.

Prompted by the work of Griffith *et al.* we applied our model to pentacene and TIPS-pentacene to give insight as to why there is a large observed difference in the polarization energy of these two materials, even though they are electronically similar. Using symmetry-adapted perturbation theory, we showed that the non-bonded interactions in the two systems are significantly different and that because of the packing differences (herringbone *vs.* brickwork) the quadrupole interactions change. This change in electrostatic interactions results in the quadrupole interactions being destabilizing in TIPS-pentacene; thus, the stabilization of the charge carrier is reduced, which in turn results in a smaller polarization energy. The impact of the molecular packing on the polarization energies and thus the solid-state ionization energies of pentacene and TIPS-pentacene highlights that care must be taken when extrapolating ionization potentials from solution-phase measurements such as cyclic voltammetry.

Continuing along this same line of thought, we then examined the effects of reduced packing density and backbone orientation on the polarization energy using tetracene and rubrene as model systems. We observed that the effect of reducing the packing density within the layer in which the charge resides is an order of magnitude larger than that of reducing the packing density between layers. This is advantageous for materials engineering as the *intra*layer density may be controlled to cause large changes in the polarization energy (keeping in mind that this can also reduce the intermolecular electronic couplings) while the *inter*layer packing density can be used to fine tune the polarization to a desired amount.

We then moved away from bulk materials to examine the energetic landscape at organic interfaces. For an organic-vacuum interface, we showed that the polarization energy at the interface is lower than that of the bulk material, which is primarily due to the reduced stabilization of induced dipoles as there are fewer polarizable sites. The polarization energy of even one layer away from the surface is found to be more representative of the bulk than of the surface; this aspect should be considered by experimental groups who wish to study the surface properties of a material, since care must then be taken to ensure that only the very surface is probed.

For an ideal organic-vacuum interface, each molecule at the surface feels the same environment; as such, the polarization energy of each site is identical, for a crystal with equivalent molecules. However, this situation no longer prevails at organic-organic interfaces where each molecular site feels a distinct environment. By combining our model for polarization energy with molecular dynamics, we have simulated a more realistic pentacene/C_{60} bilayer interface; we found that the polarization energy for a charge on either side of the interface may vary by a significant amount and that the polarization energy of each particular site can change by a large amount over time, which confirms that the energetic landscape at these interfaces is indeed very complex.

Finally, we used symmetry-adapted perturbation theory to construct detailed multidimensional potential energy surfaces for benzene and the linear oligoacenes up to hexacene. We found that under transformation each of the dimer systems presents similar surfaces when rotated from a co-facial to T-shaped dimer configuration; however, each system is unique when long-axis translation and dimer separation are considered. Additionally, we constructed 2-dimensional contour plots that show that, as the linear acene increases in length, the lowest energy separation distance decreases and there becomes a secondary low-energy configuration at even smaller separation. We also evaluated the charge-penetration contribution to the interaction energy and observed that this contribution increases linearly with acene length and is nearly as large as the total interaction energy for the dimers.

Overall, this Thesis focused on the development and application of a model for polarization energy in organic electronic materials that is both accurate and easily accessible. Within this framework, we provided insight into how the non-bonded interactions contribute to the polarization energy and how changing these interactions then changes the polarization energy. We have demonstrated that the packing configuration strongly influences the polarization energy through both packing density and molecular orientation and that the energetic landscape at organic-organic interfaces is very complex. Many factors must indeed be considered when predicting how materials will perform.

8.2 Future Considerations

Even though we have demonstrated the general applicability of our model by calculating the polarization energy of a number of systems, the model is still incomplete since thus far it only includes the electronic polarization energy. To increase the accuracy and completeness of the model, geometric relaxations of the charged molecule, expected to contribute a few tenths of an eV, lattice relaxations, on the order of 0.01 eV, and partial delocalization of the charge in highly ordered systems such as rubrene, all need to be considered. To date, a single model that incorporates all of these components has proven to be too computationally demanding; however, by combining different models that each account for one portion of the total polarization energy, a more complete picture can be gained.

While a single model that incorporates all facets of polarization energy is not likely to be developed in the short-term, there are still a number of interesting problems for which our current model can be of interest. The first such problem would be the consideration of 2-component systems where the polarization energy can be very different for each of the molecules and allowing for more accurate modeling of charge transport using Equation 1.2. Here, though, care must be taken when comparing the polarization energies at the two sites as the nuclear component due to relaxation of the charged species may be important if the electronic polarization energy difference is small.

Since the active layers in organic electronic devices are often amorphous, molecular dynamics can be used to study the effect of reduced crystallinity of the system on the polarization energy. Beginning with a crystalline system and then increasing the temperature in the simulations while taking snapshots as the temperature is increased the effect of the reduction in crystallinity can be evaluated. Such a method could also be applied to the study of bulk heterojunctions where the donor and acceptor layers have mixed.

To expand on the work of Chapter 6, additional interface configurations are also currently being considered. Gregg[2] has shown that entropy plays an important role in charge separation. By increasing the dimensionality of a system the change in entropy can be maximized, and the barrier to charge separation reduced. While C_{60} displays three-dimensional charge transport, pentacene presents two-dimensional charge transport. Thus, by increasing the dimensionality of pentacene the barrier to charge separation may be reduced. To this end, interdigitated pentacene-C_{60} interfaces are being simulated that allow some amount of *face-on* pentacene/C_{60} interaction; this retains the primarily *edge-on* orientation of pentacene.

McGehee and co-workers have recently shown that there is an equilibrium between the free charge carriers and the charge-transfer states,[3] indicating that the barrier to charge separation from charge pairs is small. From the results obtained in Chapter 6, this is not the case in the pentacene-C_{60} system, with a barrier to charge separation of several tenths of an eV, although it has been suggested that the McGehee model may only apply to high-performance OPV systems. As such, the application of our model to high-performance materials such as the T1 and T2 materials of Bazan and co-workers[4] to simulate mixed small-molecule [polymer]/PCBM interfaces is necessary.

By applying our model to determine the polarization energy in a wider range of systems, a predictive framework could be developed such that the effect of a given change in crystallinity or molecular orientation would have an expected outcome, thus allowing for better design of molecular systems with desirable properties prior to synthesis. The challenge going forward, therefore, lies in not only providing accurate description of a wide range of systems and configurations, but also in development and implementation of more accurate models that incorporate the effects currently neglected in polarization energy models.

8.3 References

(1) Xu, T.; Yin, S. *Sci. China Chem.* **2014**, *57*, 1375.
(2) Gregg, B. A. *J. Phys. Chem. Lett.* **2011**, *2*, 3013.
(3) Burke, T. M.; Sweetnam, S.; Vandewal, K.; McGehee, M. D. *Adv. Energy Mater.* **2015**, 1500123.
(4) Coughlin, J. E.; Zhugayevych, A.; Bakus, R. C.; van der Poll, T. S.; Welch, G. C.; Teat, S. J.; Bazan, G. C.; Tretiak, S. *J. Phys. Chem. C* **2014**, *118*, 15610.